The Dissertation Committee for Qinjian Jin Certifies that this is the approved version of the following dissertation:

Intraseasonal Modulation of Indian Summer Monsoon by Middle East Dust: An Observational and Numerical Modeling Study

Committee:

Zong-Liang Yang, Supervisor

Robert E. Dickinson

Rong Fu

Charles S. Jackson

Chien Wang

Intraseasonal Modulation of Indian Summer Monsoon by Middle East Dust: An Observational and Numerical Modeling Study

by

Qinjian Jin, B.S.

Dissertation

Presented to the Faculty of the Graduate School of

The University of Texas at Austin

in Partial Fulfillment

of the Requirements

for the Degree of

Doctor of Philosophy

The University of Texas at Austin

August 2015

Dedication

To my beloved parents,

who are always behind me and teach me to become strong physically and spiritually;

To my sisters,

with whom I couldn't have a happier childhood.

To my girlfriend,

who makes my life full of love!

Acknowledgements

I am grateful to my supervisor, Dr. Zong-Liang Yang, whose expertise, guidance, and encouragement make it possible for me to work on a topic of great interest to me. The knowledge and the way of critical thinking I learned from him will benefit my entire academic career. It is great pleasure to work with him.

I would like to express my gratitude to my committee members: Dr. Robert E. Dickinson, Dr. Rong Ru, Dr. Charles S. Jackson, and Dr. Chien Wang for their constructive suggestions and advice on my research. I also want to thank my host at the National Center for Atmospheric Research, Dr. Alex B. Guenther, who is always patient and inspiring, encouraging me to do better. Additionally, I thank Dr. Jianping Huang and Dr. Zhonglei Mei in Lanzhou University, who encouraged me and provide me the opportunity to explore the sciences.

I am highly appreciative and grateful to my group members Dr. Jiangfeng Wei, Dr. Hua Su, Dr. Zhongfeng Xu, Dr. Cedric David, Lisa Helper, Dr. Xiaodan Guan, Dr. Mingjie Shi, Dr. Ahmad Tavakoly, Yongfei Zhang, Gang Zhang, Alex Resovsky, Sagar Parajuli, Peirong Lin, Xitian Cai, and Dr. Long Zhao for spending countless hours listening to my talks in the group meetings, providing feedbacks and discussing interesting questions. I also want to thank my friends, Yin Lei, Kai Zhang, Binyan Yan and Dr. Hua Yuan for sharing their expertise with me.

I would like to express my gratitude to my teachers, Dr. Kerry H. Cook, Dr. Edward Vizy, Dr. William Cochran, who taught me the knowledge and skills that will help me in my career. Special thanks to Patricia Bobeck for her great teaching in scientific writing.

My research was funded by King Abdullah University of Science and Technology, China Scholarship Council, Jackson School of Geosciences, and the National Center for Atmospheric Research.

Intraseasonal Modulation of Indian Summer Monsoon by Middle East Dust: An Observational and Numerical Modeling Study

Qinjian Jin, Ph.D.

The University of Texas at Austin, 2015

Supervisor: Zong-Liang Yang

As one of the world's strongest monsoon systems, the Indian summer monsoon affects one–third of the global population. The temporal and spatial variability of the ISM rainfall has great socio-economic impacts, particularly on agriculture and food supply in South Asia. Additionally, South Asia is an area with heavy atmospheric loading of aerosols from both wind-blown mineral dust and manmade pollutants. These aerosols can significantly influence the ISM rainfall through their radiative and microphysical effects. In our study, we focus on three questions. 1) How does the ISM rainfall respond to the Middle East dust in observations on intraseasonal timescales? 2) Can the regional climate model reproduce the observed relationship between Middle East dust and the ISM rainfall, and what are the model uncertainties and how do they influence our results? 3) How does the ISM system respond to different types of aerosols in different source regions on the intraseasonal timescales? I use multiple satellite retrievals, reanalysis datasets, and ensemble modeling experiments to study the dust–monsoon connection. Multivariate empirical orthogonal function is performed on aerosol optical depth and rainfall from satellite observations, and winds and geopotential height from reanalysis to identify the coupled spatial patterns among these variables. Cross-correlation analyses between satellite-retrieved AOD in the Middle East and the ISM rainfall are calculated to

characterize the timescales of dust–monsoon connections. Furthermore, ensemble numerical experiments are conducted to examine the causal relationship and physical mechanisms between Middle East dust aerosols and the ISM monsoon. The ensemble experiments are created by perturbing physical and chemical model schemes to examine the uncertainties in parameterizing the shortwave radiation, dust diffusion in the boundary layer, and aerosol chemical mixing rules. The primary scientific findings are summarized here. (1) Middle East dust aerosols are positively correlated with the ISM rainfall in Pakistan, central and northern India, and Coastal South West India. (2) The timescale of the dust–monsoon connection is about 11 to 13 days. (3) Middle East dust aerosols can enhance the southwesterly monsoon flow over the Arabian Sea due to their direct radiative heating effect in the lower troposphere, which can increase the south–north ocean–land thermal contrast. The enhanced monsoon flow can transport more water vapor from the Arabian Sea to the Indian subcontinent, thereby resulting in more monsoon rainfall. (4) Middle East dust aerosols play a dominant role in modulating the ISM rainfall compared to dust aerosols from other regions; local anthropogenic aerosols in India, although with much lower concentrations than dust, can play a similar role to Middle East dust aerosols. Our findings demonstrate that a better representation of Middle East dust aerosols and their interactions with meteorological fields is important for understanding and modeling the variability of the ISM rainfall.

Table of Contents

List of Tables

List of Figures

Chapter 1: Introduction

1.1. Aerosol and Indian Summer Monsoon

1.1.1. Aerosols

Aerosols are solid particles or liquid droplets suspended in the Earth's atmosphere, with radii ranging from 0.001 μm to 100 μm. Aerosols can be classified into primary or secondary aerosols. Primary aerosols contain particles injected directly into the atmosphere, while secondary aerosols involve gas–particle conversion. Wind-Blown mineral dust and sea salt are examples of primary aerosols, and sulfates converted from biogenic or volcanic gases are example of secondary aerosols. Air pollution can be both primary and secondary aerosols.

Aerosols can come from various sources, such as natural and anthropogenic emissions. As natural aerosols, mineral dust and sea salt account for more than 90% of the total aerosol loading around the globe, with dust of ~40% and sea salt of ~50% (IPCC, 2001). Other aerosols, such as industrial dust, fossil fuel, and aircraft from anthropogenic emissions and biogenic emission and biomass burning from natural emissions, account for less than 10%. These aerosols can be differentiated through measurements of their physical and chemical properties, which are also parameterized in numerical models. Some of the important physical properties include aerosol optical depth (AOD), particle size distributions, refractive index, the asymmetry parameter, the single-scattering albedo, hygroscopicity, and so on. Some of these physical properties are linked to or determined by their chemical properties, e.g. aerosol chemical compositions. The common compositions of aerosols are sulfate, nitrate, ammonium, black carbon, mineral dust ($CaCO_3$), sea salt (NaCl), organic carbon, and water.

The concentration of aerosols can be measured by AOD. Figure 1.1 shows the geographic distributions of seasonal AOD at 550 nm from satellite observations over a period of 2000–2014. This AOD is comprised of all aerosol types from both natural and anthropogenic sources. Unlike greenhouse gases, which are well mixed in the atmosphere and tend to be evenly distributed around the globe, dust aerosols tend to concentrate near their source regions. It is obvious that heavy aerosol loadings are observed in the tropical and subtropical regions and the northern hemisphere has higher AOD values than the southern hemisphere. Furthermore, AOD shows greater values and a larger spatial extent during the boreal summer season than in other seasons.

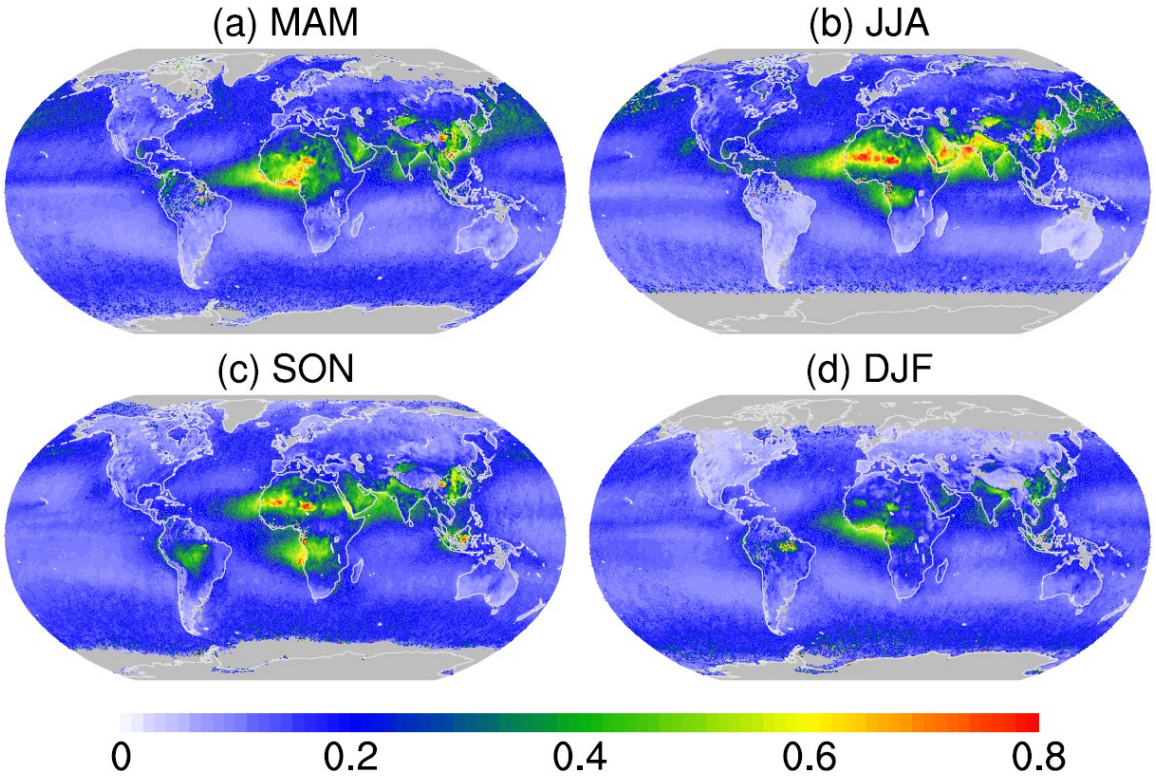

Figure 1.1. Geographic distribution of seasonal AOD at 550 nm over March 2000–February 2014. The data are from MISR level three monthly AOD. The gray color represents missing values.

1.1.2. Indian Summer Monsoon

A monsoon is defined as seasonal changes in atmospheric circulation and precipitation associated with the asymmetric heating of land and ocean. The Indian summer monsoon (ISM) is one of the world's largest monsoon systems due to the large Eurasian landmass to the north of the Indian Ocean. During the late boreal spring, the landmass in Eurasia receives increasing solar radiation and becomes warmer than the Indian Ocean because of the lower heat capacity of landmass than the ocean. This heterogeneous surface warming between land and ocean results in a thermal low-pressure system centered over northwest India, Pakistan, Afghanistan, Iran, and the Arabian Peninsula, and a high-pressure system located in the south Indian Ocean. This south–north ocean–land pressure gradient can then drive strong winds from the Indian Ocean northward to the Indian subcontinent, forming one of the largest monsoons during the boreal summer (Webster and Fasullo, 2014).

The ISM rainfall is extremely important for the large population in South Asia (Figure 1.2a). Heavy rainfall occurs in Coastal South West India, central and north India, and Bay of Bengal. The ISM rainfall exhibits quite strong seasonal variations. Most of the ISM rainfall events occur in the boreal summer (~50%) with limited rainfall in the boreal winter (7%). Furthermore, rainfall is used to define the ISM onset and demise (Fasullo and Webster, 2003). The ISM arrives in south India in late May or early June and gradually moves northward and westward to Pakistan in early July. It begins to retreat from Pakistan in early September and withdraws from south India in late September.

The variability of the ISM rainfall on intraseasonal and inter-annual timescales is affected by a number of factors (e.g. Turner and Annamalai, 2012), such as sea surface temperature (SST) in the Indian Ocean (Levine and Turner, 2012), El Niño–Southern Oscillation (ENSO) (Mishra et al., 2012), and snow cover in previous winter (Saha et al.,

2013). A better understanding of the contributors of the ISM variability is of great importance for the ISM prediction and for reducing the casualties and property loss caused by floods and droughts during the ISM season.

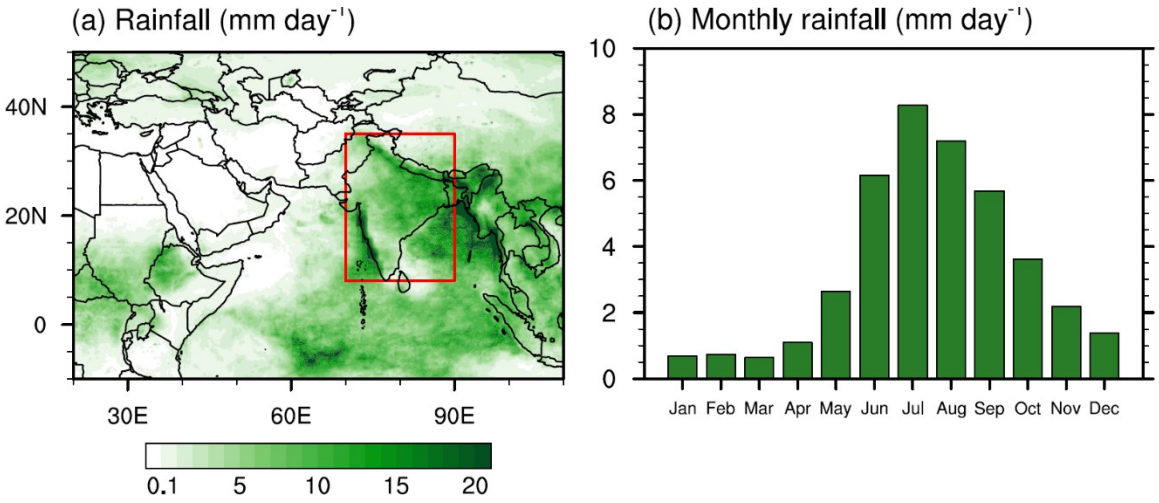

Figure 1.2. (a) Spatial patterns of JJA rainfall (mm day^{-1}). (b) Monthly rainfall (mm day^{-1}) area-averaged in India marked by the red box (8°–35°E, 70°–90°N) in Figure 1.2a. The data are from TRMM observations and averaged for 1998–2014.

1.2. Review of Monsoon Responses to Aerosols

Aerosols can play significant roles in the Earth's climate system, biogeochemical cycles, and human health. They can influence the Earth's radiative budget by scattering and absorbing solar and terrestrial radiation (direct effect) (Satheesh and Moorthy, 2005). They can also work as cloud condensation nuclei (CCN) and ice nuclei (IN), evaporate clouds and change clouds microphysical properties (indirect effect) (Lohmann and Feichter, 2005). When mixed with clouds, aerosols can evaporate clouds (semi-direct effect) (Hansen et al., 1997). Furthermore, deposition of aerosols on land, snow, and ice can change the surface albedo, resulting in melting of snow and ice (cryosphere radiative effect) (Qian et al., 2011; Flanner, 2013). When deposition occurs on ocean, aerosols can

provide nutrients, e.g. nitrogen, iron and phosphorus, acting as fertilizers to ocean microbiology (biogeochemical effect) (Mahowald, 2011).

The ISM region has been identified as a heavy aerosol loading area. The high AOD values in India are partly attributed to the local air pollutions and desert dust emission from the Thar Desert. Besides the local aerosol sources, the ISM regions is surrounded by the world's second and third largest deserts, i.e. the Arabian Desert to its west and the Taklimakan Desert and the Gobi Desert to its northeast. The dust aerosols in the remote deserts can be transported to the Indian subcontinent.

Previous studies have well documented the impacts of local anthropogenic aerosols in India and remote dust aerosols in East Asia on the ISM system. The increasing anthropogenic emissions in India contribute to a drier ISM on the decadal timescales since 1950s through reducing the south–north ocean–land thermal contrast due to aerosol's surface cooling effect in India, known as the "solar dimming effect" (Ramanathan et al., 2005; Meehl et al., 2008; Bollasina et al., 2011, 2013; Bollasina et al., 2014). On the contrary, the local anthropogenic aerosols in India especially black carbon and the remote dust emissions in the Taklimakan Desert can stack up around the Tibetan Plateau and warm the mid-upper troposphere over the Tibetan Plateau by absorbing solar radiation on the inter-annual timescales. Associated with this heating is a low-pressure system, which causes the air to converge in the mid-upper troposphere over north India and a strengthened northward monsoon flow in the lower troposphere over central and south India. This heating effect of aerosols on the ISM rainfall is known as the "elevated heating pump" (EHP) (Lau et al., 2006). The EHP effect has been subject to debate mainly due to the lack of observational support (Lau and Kim, 2006; Kuhlmann and Quaas, 2010; Nigam and Bollasina, 2010; Lau and Kim, 2011; Nigam and Bollasina, 2011). Furthermore, the heating in the planetary boundary layer initiated by absorbing aerosols (i.e. black carbon)

in India can increase the moist static energy (MSE) of subcloud layers, which in turn results in more rainfall during the ISM season (Wang et al., 2009b). It should be noticed that the solar dimming and the EHP effect influence the ISM rainfall by modulating the large-scale atmospheric circulation; therefore, they tend to have a stronger impact on the stratiform rainfall than convective rainfall. However, the aerosol-induced perturbation of MSE tends to increase the convective rainfall.

1.3. Understudied Impact of the Middle East Dust Aerosols

The abovementioned studies examined the responses of the ISM system to the remote desert dust emissions in East Asia as well as the local dust and anthropogenic emissions in India. However, there are quite few studies focusing on the Middle East dust aerosols and their impacts on the ISM system.

The Middle East and the Arabian Sea have quite heavy aerosol loading during the ISM season, as shown in Figure 1.1. There are several aerosol hot spots in this region, such as the Arabian Peninsula, the Arabian Sea, and the Iranian Plateau. The high AOD values over the Arabian Sea are attributed to the long-distance transport of dust aerosols from the Arabian Peninsula by the strong northwesterly "Shamal" winds. These aerosols can influence the local climate. The intensified cyclones over the AS have been partly attributed to aerosol-induced SST change (Evan et al., 2011). The positive AOD anomalies over the AS are found to be associated with drought in India (Rahul et al., 2008). Furthermore, studies found that the thermal forcing over the IP and AP could exert a dominant impact on the ISM rainfall in central India and the ISM evolution (Wu et al., 2012; Iqbal et al., 2013). Therefore, it is crucial to examine the potential impacts of the Middle East dust on the ISM system.

Vinoj et al. (2014) demonstrated a positive correlation between the ISM rainfall in south India and dust aerosols in the western part of North Africa and over the Arabian Sea over timescales of about a week. Using GCM (i.e. CAM5) simulations, they attributed this dust–monsoon correlation to dust-induced heating in the lower troposphere over North Africa and West Asia, which can enhance water vapor transport from the Arabian Sea to the Indian subcontinent, thereby resulting in more monsoon rainfall in India. They mainly focused on the ISM rainfall changes in south India, but the ISM rainfall plays a more important role in north India and Pakistan because of the much greater population in this region than in south India. The monsoon rainfall has shown significant trends in north central and north India during the second half of the past century (Bollasina et al., 2011). However, the spatial patterns of the rainfall increases simulated by Vinoj et al. (2014) are not quite consistent with observations, which can be partly attributed to a coarse horizontal resolution (2.5°×1.9°) in CAM5. The poor representation of the Tibetan Plateau by such a coarse resolution can cause deficiencies in simulating the radiative–dynamical interactions of the ISM flow (Bollasina et al., 2011). Using CAM5.1, Wehner et al. (2014) showed that the high-resolution (0.23°×0.31°) simulations can better capture the ISM extreme rainfall events than those from coarser resolutions (0.9°×1.3° and 2.6°×1.9°). Therefore, high-resolution simulations are needed to study the dust–monsoon relationship.

1.4. OBJECTIVES

This study examines the relationship between the Middle East dust and the ISM system using both observations and high-resolution numerical modeling. The physical mechanism underlying the dust–monsoon relationship is studied in detail. A further step is taken to quantify the different impacts of dust versus anthropogenic emissions in different source regions on the ISM rainfall.

Three research questions are proposed:

1) How does the ISM rainfall respond to the Middle East dust in observations on intraseasonal timescales?
2) Can the regional climate model reproduce the observed relationship between Middle East dust and the ISM rainfall, and what are the model uncertainties and how do they influence our results?
3) How does the ISM system respond to different types of aerosols in different source regions on the intraseasonal timescales?

In Chapter 2, multiple satellite and reanalysis datasets are used to investigate the relationship between Middle East dust and the ISM system. Correlation and composite analyses of monthly anomalies of AOD and rainfall both from satellites are performed to decipher the relationship between them. The method of multivariate empirical orthogonal function (MV-EOF) analysis is used to find out the coupled spatial patterns of AOD, heating in the lower-mid troposphere, the ISM circulation and rainfall. Results from observations are included in Chapter 2.

In Chapter 3, the observed relationship between dust and monsoon rainfall in Chapter 2 is further examined using a numerical modeling method. Thirty-two ensemble simulations are created through the perturbed physical and chemical ensemble (PPCE) method to consider the model uncertainties in parameterizations of shortwave radiation scheme, aerosol turbulent mixing in the boundary layer, and aerosol chemical mixing rules. The dust impact is represented by the difference between ensemble means of simulations with and without dust emission. The modeling results are shown in Chapter 3.

In Chapter 4, the responses of the ISM system to different aerosol types in different source regions are compared. Our results in this chapter are compared with previous studies by quantifying the ISM responses to the local dust and anthropogenic emissions in India

and remote dust emission in the Middle East and East Asia. The EHP effect is also examined. These results are demonstrated in Chapter 4.

Finally, the conclusions and future work are summarized in Chapter 5.

Chapter 2: Observational Positive Response of the Indian Summer Monsoon to Middle East Dust

2.1. ABSTRACT

Using observational and reanalysis data, we investigated the impact of dust aerosols over the Middle East and the Arabian Sea (AS) on the Indian summer monsoon (ISM) rainfall. Satellite and aerosol reanalysis data show extremely heavy aerosol loading, mainly mineral dust, over the Middle East and AS during the ISM season. Multivariate empirical orthogonal function analyses suggest an aerosol–monsoon connection. This connection may be attributed to dust-induced atmospheric heating centered over the Iranian Plateau (IP), which enhances the meridional thermal contrast and strengthens the ISM circulation and rainfall. The enhanced circulation further transports more dust to the AS and IP, heating the atmosphere (positive feedback). The aerosols over the AS and the Arabian Peninsula have a significant correlation with rainfall over Central and Eastern India about two weeks later. This finding highlights the nonlocal radiative effect of dust on the ISM circulation and rainfall and may improve ISM rainfall forecasts.

2.2. INTRODUCTION

The inter-annual and seasonal variability of the Indian summer monsoon (ISM) rainfall is extremely important for the large population in this region. A number of factors contribute to this variability, such as sea surface temperature (SST) (Levine and Turner, 2012), El Niño-Southern Oscillation (ENSO) (Mishra et al., 2012), and snow cover (Saha et al., 2013). In recent years, the impact of aerosols, including their direct and indirect effects on the ISM system, has received increasing attention.

Anthropogenic black carbon and other man–made aerosols, which show an increasing trend in Asia in recent decades, may reduce ISM rainfall by exerting a surface cooling effect over the Indian subcontinent and surrounding regions. This aerosol-induced

cooling effect through scattering and absorbing solar radiation results in a reduced north–south land–sea thermal contrast and a weaker meridional monsoon circulation (the solar dimming effect) (Ramanathan et al., 2005; Meehl et al., 2008; Bollasina et al., 2011) attributed the observed ISM drying trend over central-northern India in the past 60 years mainly to human-influenced aerosols. The importance of non-Asian anthropogenic and biomass burning emissions in suppressing ISM rainfall was also reported (Cowan and Cai, 2011; Ganguly et al., 2012). The above studies addressed the impacts of aerosols on suppressing ISM rainfall on the decadal timescales. However, more and more studies found that aerosols could strengthen ISM on the inter-annual or seasonal timescales. Wang et al. (2009b) showed that the heating initiated by absorbing aerosols within the planetary boundary layer can increase sub-cloud layer moist static energy and ISM rainfall. Lau et al. (2006) postulated that the thermal heating over the Tibetan Plateau, which is exacerbated by heat-absorbing black carbon emissions on the southern slopes of the Tibetan Plateau, acts like an elevated heat pump (EHP) that can advance and intensify ISM rainfall. It should be pointed out that the EHP mechanism has been subject to debate (Nigam and Bollasina, 2010; Lau and Kim, 2011; Nigam and Bollasina, 2011), mainly because it has little observational support (Kuhlmann and Quaas, 2010). Furthermore, the impact of aerosols on strengthening ISM was also reported on the intraseasonal timescales. Bollasina et al. (2013) found that anthropogenic aerosols were likely responsible for the observed earlier onset of the ISM.

The majority of the aforementioned studies focus primarily on the impacts of anthropogenic or biomass-burning emissions over land on the ISM system; much less attention has been paid to natural aerosols, especially mineral dust. Wang et al. (2009a) studied the contribution of dust aerosols to the total absorbing aerosol optical depth (AOD) and found that dust aerosols were equal to anthropogenic aerosols in terms of absorbing

solar radiation over the Indian subcontinent and nearby regions. Kuhlmann and Quaas (2010) examined the vertical profile of various kinds of global aerosols using the Cloud–Aerosol Lidar and Infrared Pathfinder Satellite Observation (CALIPSO) dataset and concluded that heavy dust loadings were observed over the AS with up to 80% of the measurements detecting either dust or polluted dust.

The AS and the Middle East have heavy dust loadings during the ISM season (Figure 2.1). Several dust-active regions are present in our domain: the southern AP, the AS, Iran, Afghanistan, and Pakistan. The dust aerosols over the AS are transported from land. Over the last decade, the AS and AP have shown the greatest increasing aerosol concentration trend during the boreal summer (Hsu et al., 2012). Despite the remarkable potential importance of aerosols over the Middle East and the AS in influencing the ISM system, less attention has been focused on it than on anthropogenic aerosols over India and the Tibetan Plateau, especially on timescales shorter than one month. Rahul et al. (2008), using four years of AOD datasets, reported positive and negative AOD anomalies over the AS during the recent Indian normal and drought years, respectively. Evan et al. (2011) attributed the intensified AS tropical cyclones to aerosols over the AS. Very lately, Vinoj et al. (2014) showed a positive correlation between West Asian dust and ISM rainfall over timescales of about a week and attributed this correlation to dust-induced heating of the atmosphere over North Africa and West Asian. On the other hand, the thermal forcing of the IP also plays a significant role in the ISM evolution. Wu et al. (2012) found that the thermal forcing of the IP dominates the northern part of the ISM system. Iqbal et al. (2013) demonstrated that the south Asian heat low extending to the IP exerts a dominant impact on ISM rainfall over Central India. Therefore, examining the direct radiative effect of dust

aerosols over the IP and AS on the ISM system can lead to a better understanding of the dust–monsoon interaction.

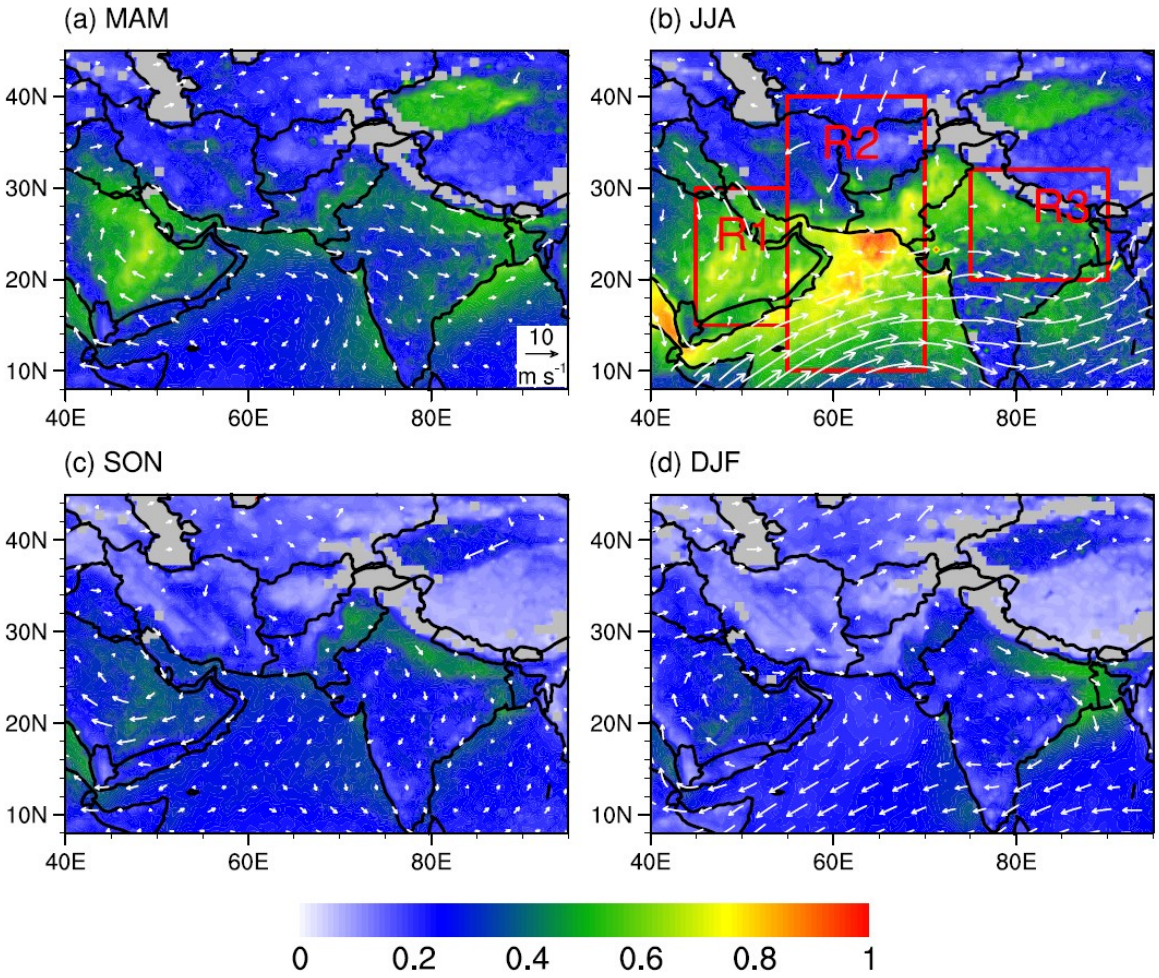

Figure 2.1. Spatial distribution of climatological mean (2000–2013) of seasonal AOD at 550 nm and 850 hPa winds in the ISM region. Results are shown for (a) spring (MAM), (b) summer (JJA), (c) fall (SON), and (d) winter (DJF). Aerosols are from MISR level–three monthly satellite data and winds are from MERRA monthly reanalysis data. The grey colors represent missing values. The red boxes in (b) are regions for further analysis.

In this paper, we provide observational evidence for a different mechanism from Vinoj et al. (2014) to address the response of ISM rainfall to dust aerosols over the AS and

the Middle East on weekly timescales, using data from long–term (2000–2013) satellite AOD observations and atmospheric reanalyses. This new mechanism sheds further light on the interactions among dust, radiative forcing, and ISM and providing more quantitative estimates of the timescales of those interactions.

2.3. Data and Methods

Monthly gridded level–three AOD datasets retrieved by the Multi–angle Imaging SpectroRadiometer (MISR) ($0.5^o \times 0.5^o$) and the Moderate Resolution Imaging Spectroradiometer (MODIS) ($1^o \times 1^o$) both onboard the Terra satellite and daily AOD from MODIS onboard the Aqua satellite ($1^o \times 1^o$) are used to study the aerosol–monsoon interaction. Monitoring Atmospheric Composition and Climate (MACC) ($0.5^o \times 0.5^o$) reanalysis data of partial AOD of various aerosol types, developed at the European Centre for Medium-Range Weather Forecasts (ECMWF) (0.5×0.5^o), are also used (Benedetti et al., 2009). For rainfall data, we used Tropical Rainfall Measuring Mission (TRMM) monthly 3B43 and daily 3B42 (both version 7) data ($0.25^o \times 0.25^o$) and the National Oceanic and Atmospheric Administration (NOAA) Precipitation Reconstruction over Land (PREC/L) ($1^o \times 1^o$) (Chen et al., 2002). The TRMM product merged the surface rain gauge data and satellite estimates and NOAA's PREC/L merged only the gauge observations over land. Zonal and meridional wind components obtained from Modern Era Retrospective analysis for Research and Applications (MERRA) ($1/2^o \times 2/3^o$) (Rienecker et al., 2011) reanalysis datasets are compared for consistency with ECMWF Interim Reanalysis (ERA-Interim) ($0.5^o \times 0.5^o$) (Dee et al., 2011). The HadlSST1 dataset was used to calculate Niño 3.4 SST index. All the data used are for the period of 2000–2013, except for Aqua-MODIS AOD and MACC reanalysis datasets, which are for the period of 2003–2013. All datasets used in this study are available in the Auxiliary Material (Text S3).

Multivariate empirical orthogonal function (MV-EOF) analysis, also referred to as combined principal component analysis (PCA) with two or more field variables combined in the same PCA, is a useful tool for isolating coupled patterns of variability among multiple fields (Bretherton et al., 1992; Mishra et al., 2012). In this study, AOD, thickness between two pressure levels, zonal and meridional wind components, and rainfall are combined to perform MV-EOF analysis, in an attempt to unveil the physical mechanism responsible for the aerosol–rainfall connection. Each variable was standardized by its mean standard deviation so that the variance of the different variables were comparable in the MV-EOF analysis. Meanwhile each variable maintains its original spatial distribution of variance.

2.4. RESULTS

2.4.1. Aerosol Climatology and Composition

Figure 2.1 shows the spatial distribution of climatological mean (2000–2013) of seasonal MISR AOD at 550 nm and MERRA 850 hPa winds. In our study domain, boreal spring (March–April–May (MAM)) and summer (June–July–August (JJA)) are high-aerosol seasons; fall (September–October–November (SON)) and winter (December–January–February (DJF)) show much less aerosol. In MAM, high aerosol concentrations are observed over the AP, the Indian subcontinent, and the Taklimakan Desert. In JJA, higher than MAM aerosol concentrations are observed over the AP, the AS, the IP, Pakistan, the Indian subcontinent, and the Taklimakan Desert. In fall and winter, relatively low aerosol concentrations are found in the northern Indian subcontinent along the Himalayas. The AOD over the AS and IP has much greater seasonality than over Central and Eastern India (CEI).

One interesting phenomena is that the AOD over water bodies, such as the Red Sea

and the AS, is higher than over the adjacent land regions, such as the AP and the Indian subcontinent. A possible cause is aerosol humidification. Both theoretical investigations and field experiments show that water vapor can strengthen the aerosol's light scattering ability, thus resulting in higher AOD (Jeong et al., 2007; Boucher and Quaas, 2013). The relatively weak wind over the northern AS (Figure 2.1b) can also promote aerosol accumulation in these areas, resulting in high AOD values. Furthermore, minimal washout of aerosols by rainfall over the AS may also contribute to high AOD values.

Using MACC aerosol reanalysis data, the contributions of various aerosol types to the total AOD are shown in Figure 2.2. The aerosol model in MACC (Morcrette et al., 2009) includes five aerosol types: mineral dust, sulfate, sea salt, organic matter, and black carbon. Mineral dust aerosols dominate the study domain, especially over the Red Sea, the AP, the AS, Pakistan, northwest India, and the Taklimakan Desert. Mineral dust contributes 53% of the total AOD over the AS and IP. Using CALIPSO, Kuhlmann and Quaas (2010) found that 80% of measurements are either dust or polluted dust aerosols over the northwest AS (60–65°E, 20–25°N). Both MACC and CALIPSO datasets show that mineral dust produces the greatest amount of AOD over the AS and IP. The other four aerosol types contribute much less to the total AOD over the AS and IP: 28% for sulfate, 12% for sea salt, 5% organic matter, and 2% black carbon.

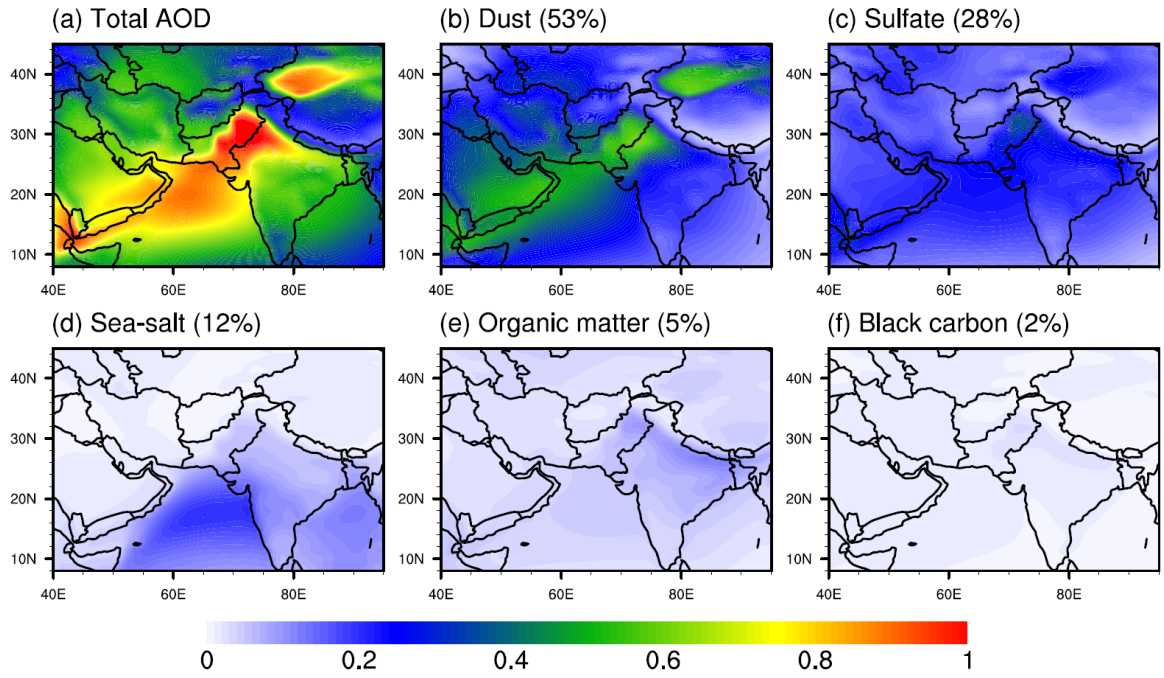

Figure 2.2. Spatial distribution of climatological mean (2003–2013) of JJA AOD at 550 nm for various aerosol types in the ISM region. Results are shown for (a) Total AOD, (b) mineral dust, (c) sulfate, (d) sea salt, (e) organic matter, and (f) black carbon. The numbers in brackets represent the percentage of contribution of each aerosol type to the total AOD over the AS and IP (R2 in Figure. 2.1b). Aerosols are from ECMWF MACC 6 hourly reanalysis.

2.4.2. Aerosol–ISM Connection

In order to demonstrate the spatiotemporal connections between aerosols, atmospheric circulation, and ISM rainfall, MV-EOF was performed on AOD, thickness between 500 and 700 hPa pressure levels, winds, and rainfall in JJA from 2000 to 2013. According to the hypsometric equation, the thickness between two pressure levels is proportional to the average air temperature between them.

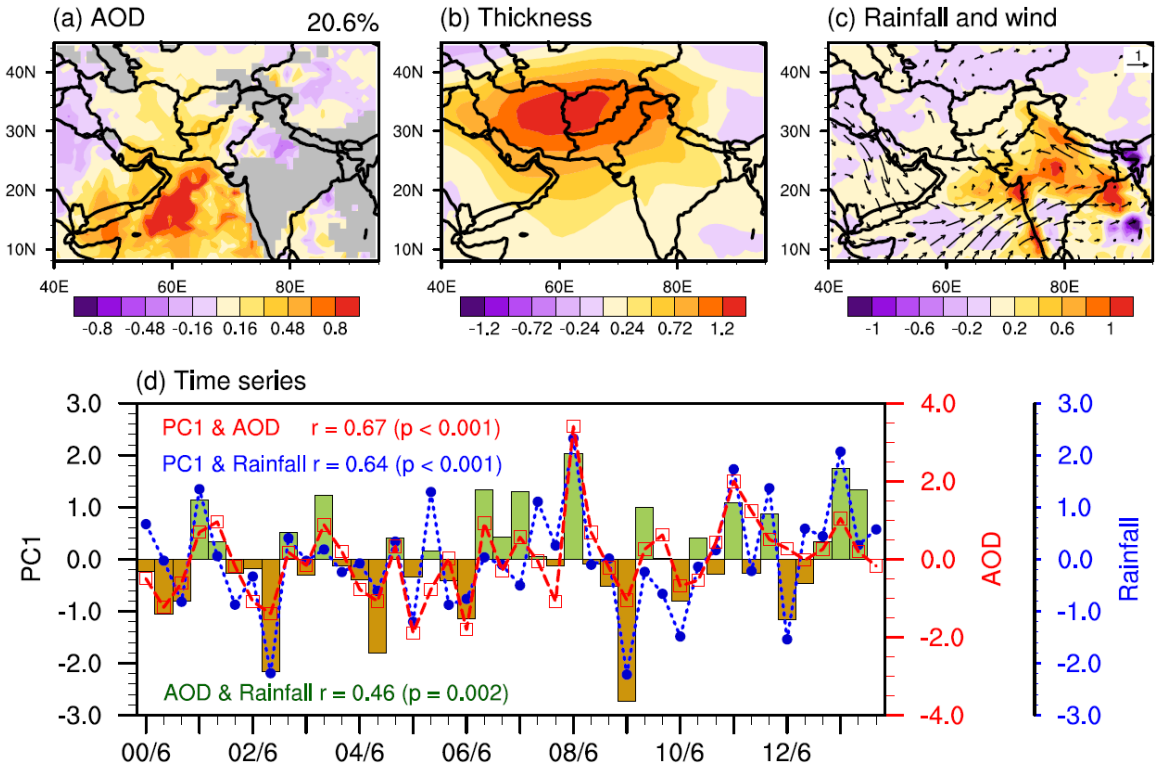

Figure 2.3. Leading MV-EOF spatial patterns for JJA 2000–2013 monthly (a) AOD, (b) thickness between 700 and 500 hPa pressure levels, and (c) TRMM rainfall and MEERA 850 hPa winds, and (d) their associated time series (bars). See section 2 for details. The monthly anomalies of AOD over the AS and IP (R2 in Figure 2.1b: 10−40°N, 55−70°E) and rainfall over CEI (R3 in Figure 2.1b: 20−32°N, 75−90°E) are also shown. All data are standardized. The grey color in (a) represents missing values.

The leading mode of MV-EOF analysis shows the strongest positive AOD anomalies over the AS and the southern AP with 0.7 to 0.8 standard deviation from the mean (Figure 2.3a). Less strong (0.3 to 0.4 standard deviation) positive anomalies appear over the IP in most areas of Iran and Pakistan, western and southern Afghanistan, and the regions north to Iran and Afghanistan. Figure 2.3b shows a center of strong heating in the lower troposphere between 700 and 500 hPa around the IP with more than one standard deviation from the mean. This heating center extends further southward to the AS.

Corresponding to the heating gradient are enhanced southwesterly and northwesterly winds over the AP and AS, respectively, with about one standard deviation from the mean (Figure 2.3c). The enhanced southwesterly wind can transport increased water vapor from the AS to the Indian subcontinent, contributing to a stronger monsoon and more increased rainfall (Figure 2.3c). On the other hand, the enhanced northwesterly wind can generate more dust aerosols over the IP and transport these dust aerosols to the AS and IP (to be shown later), forming a positive feedback. Figure 2.3d shows the time series associated with the leading MV-EOF mode, AOD monthly anomaly over the AS and IP, and the rainfall monthly anomaly over CEI. All three-time series show weak positive trends. The trend for AOD is most significant and has been found in other studies (Hsu et al., 2012). The time series of the leading MV-EOF is significantly correlated with both AOD ($r = 0.67$) and rainfall ($r = 0.64$). Similar results are also found in ERA-Interim and NOAA PREC/L datasets (not shown). This connection between rainfall and aerosol can be confirmed by a simple correlation analysis of the area-averaged rainfall in CEI and AOD over the AS and IP ($r = 0.46$); the spatial distributions of the Spearman rank correlation coefficient are included in Text S2. The coupled patterns among AOD, thickness, winds, and rainfall in the leading mode of MV-EOF suggests a connection between dust aerosols over the AS and IP and atmospheric heating in the lower troposphere, which may be responsible for the enhanced ISM circulation and rainfall.

ISM rainfall has been shown to be correlated with ENSO (Mishra et al., 2012). No significant correlation exists between time series of the leading mode of MV-EOF and ENSO; however, a significant correlation coefficient of 0.51 is found between the time series of the second mode and ENSO (not shown). Therefore, the leading mode (Figures 2.3) is likely to be driven by the aerosol anomaly, and the second mode is associated with ENSO.

Note that the location of maximum heating and maximum AOD are slightly different. This is due to the high surface albedo over the IP, which can enhance aerosol-induced atmospheric heating by reflecting more solar radiation to dust layers above than the sea surface (Kuhlmann and Quaas, 2010). Another potential reason for the location difference is the high atmospheric heating efficiency over land due to low water vapor content.

We further studied this heating effect by performing composite analyses. First, 14 months with the highest and 14 with lowest AOD values over the IP (25−40°N, 50−70°E) based on MISR monthly AOD were selected from the 42 JJA months of 2000−2013. The time-averaged zonal mean (55−70°E) differences of monthly temperature anomalies between these 2 sets of 14 months were calculated for different pressure levels and shown in Figure 2.4. We used temperature data from both MERRA and ERA-Interim reanalysis. Although none of them includes variable aerosols in their reanalysis model, the upper air temperature variations should be captured by assimilating data from weather balloons. Both MERRA and ERA-Interim show strong and significant heating over the IP and relatively weaker heating in the lower troposphere over the AS. The heating in the upper troposphere is not significant because of the large variance of temperature there. The meridional thermal gradient increases more in the upper troposphere than in the lower troposphere, which is consistent with the general findings of Dai et al. (2013) on Asian monsoons.

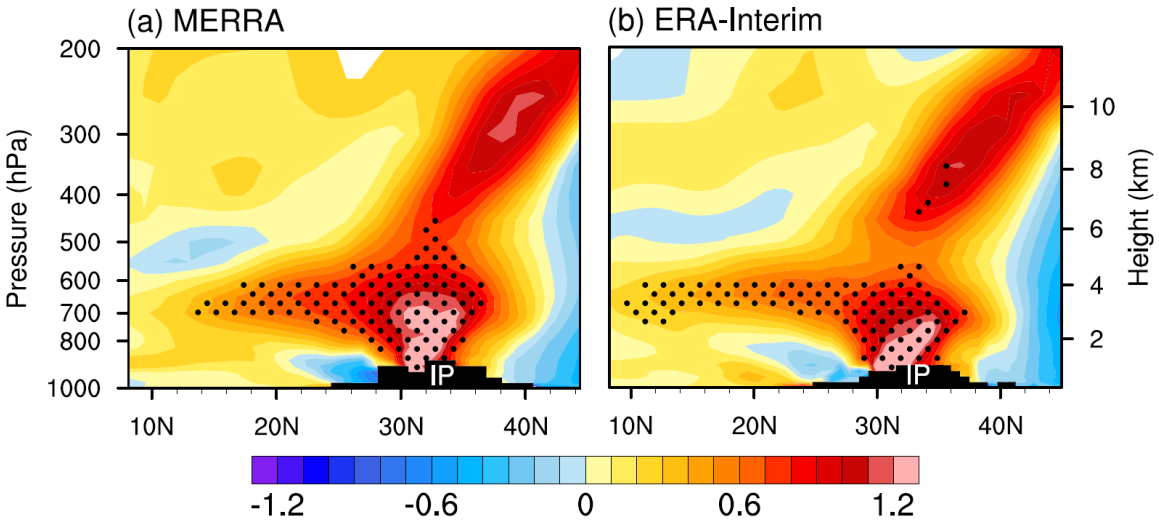

Figure 2.4. Zonal mean (55−70°E) of air temperature differences (for each pressure level) between 14 months with the highest AOD (in the order of AOD from low to high: 2011/08, 2013/06, 2013/07, 2009/08, 2012/07, 2006/07, 2009/07, 2010/07, 2008/06, 2008/07, 2011/07, 2011/06, 2001/07, and 2003/07) and 14 months with the lowest AOD (in the order of AOD from low to high: 2007/08, 2005/06, 2005/08, 2006/06, 2000/08, 2002/08, 2000/06, 2001/08, 2002/06, 2007/06, 2004/06, 2006/08, 2012/06, and 2012/08) of total 42 JJA months in 2000−2013. Results are shown for (a) MERRA and (b) ERA-Interim. The black dots highlight the differences that are confident at 95% level, which are determined by a bootstrap test of sampling the data during the 42 JJA months for 10,000 times. Unit: K.

2.4.3. Physical Mechanism of the Aerosol–Rainfall Connection

Based on the above analyses, we propose a physical mechanism that may be responsible for the aerosol–rainfall connection. Aerosol-induced atmospheric heating over the IP and AS may intensify the meridional thermal contrast and lead to stronger southwesterly winds over the AS; these winds can transport more water vapor from the AS to the Indian subcontinent and increase ISM rainfall in CEI. The enhanced thermal contrast may also lead to stronger northwesterly winds over the AP, producing and transporting more dust aerosol to the IP and AS. Thus, a positive feedback loop may exist, which strengthens the effect. To verify the aerosol's transport pathways and its effect on rainfall,

cross correlations were performed between winds over the AP, AOD over the AS and IP, and rainfall over CEI (Figure 2.5). Because it takes time for dust to travel from the AP to the AS and IP and to influence rainfall via the above-mentioned mechanism, lagged correlations are calculated. The red curve in Figure 2.5 shows that the Spearman rank correlation coefficients between wind over the AP and AOD over the AS and IP reach a peak when wind leads AOD by three days. For AOD and rainfall, the lead-time for the strongest correlation is 13 days; for wind and rainfall, the lead-time is 17 days. The lead-time between wind and AOD roughly equals to the sum of the other two, indicating that the processes are almost sequentially connected. Note that the region for AOD includes both AS and IP (R2 in Figure 2.1b); if using AOD over IP, the results are similar except the peak correlation between wind and AOD is lower but still significant, as shown in Figure 2.6. These lagged relationships between winds, AOD, and rainfall further confirm the mechanism discussed above, because if their variations are caused by other common factors (e.g., SST) they are not very likely to have such lagged relationships.

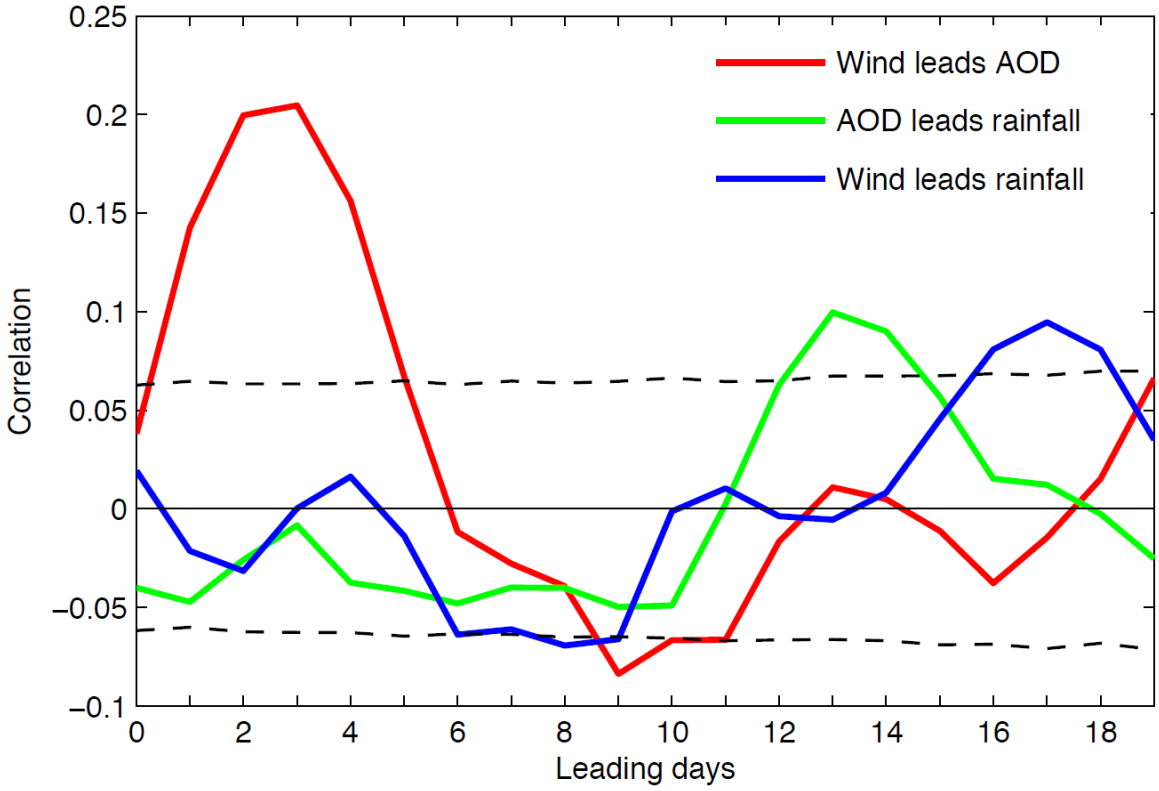

Figure 2.5. Cross Spearman rank correlation coefficients between 2 m winds amplitude over the AP (R1 in Figure 2.1b: 15−30°N, 45−55°E), AOD over the AS and IP (R2 in Figure 2.1b: 10−40°N, 55−70°E), and rainfall over CEI (R3 in Figure 2.1b: 20−32°N, 75−90°E). All correlations are calculated based upon daily anomalies obtained by substracting the 19-day running mean from the daily data. Two dash lines represent the 95% confidence intervals, which are calculated by a bootstrap test of permuting the original time series for 10,000 times. The intervals change with time lag because of the decreasing of sample sizes. Different pairs of time series have similar confidence intervals and those from one pair are shown here.

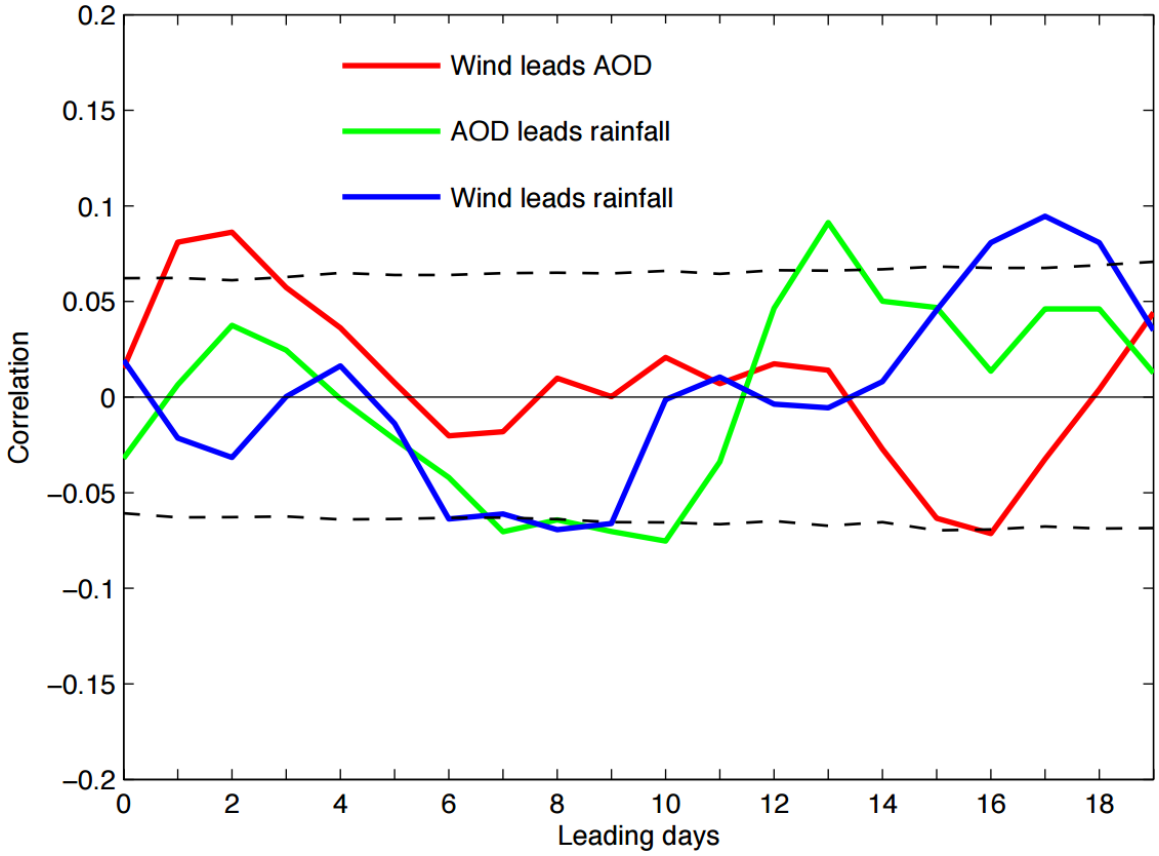

Figure 2.6. Same as Figure 2.5, but with AOD area-averaged over the IP (25−40°N, 55−70°E).

2.5. Discussion and Conclusions

High AOD values (about 0.49) were observed over the AS and IP in JJA in independent satellite retrievals. The high AOD values over the AS coincides with a wetting trend over this region (Damberg and AghaKouchak, 2013), implying a possible positive relationship between AOD and rainfall, but a simple Spearman rank correlation analysis (see Figure 2.7) shows no significant correlation between AOD and rainfall. The MV-EOF analysis (Figures 2.3c and 2.3d) points to the dominant role of moisture flux on rainfall in this region. The AOD over the AS and IP starts to increase in MAM, reaches a peak in JJA,

begins to decrease in SON, and sustains at a very low level in DJF. The overlap of the AOD peak period with the ISM season provides the possibility that dust aerosols over the Middle East and the AS may influence ISM rainfall.

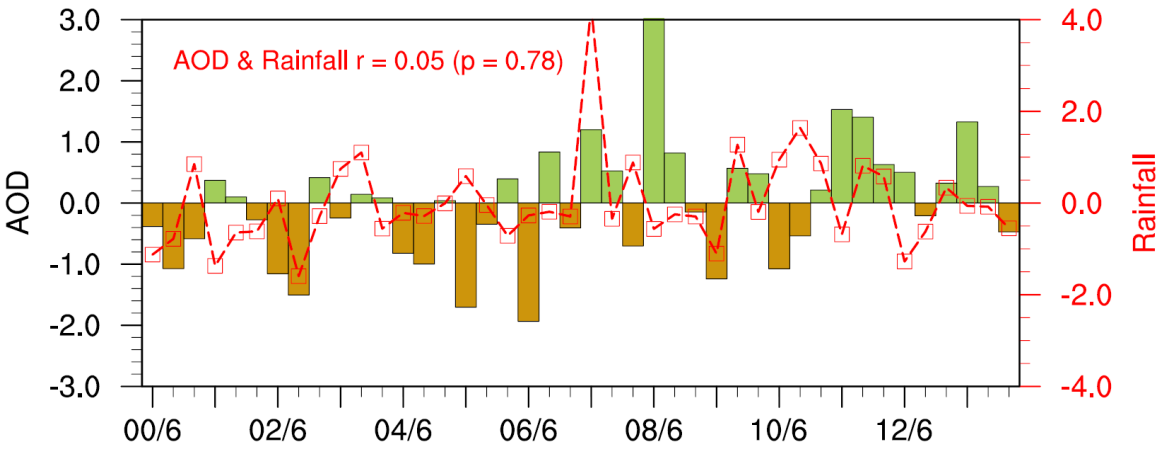

Figure 2.7. Time series of monthly anomalies of MISR AOD and TRMM rainfall (mm day^{-1}) both area-averaged over the AS (60–65°E, 20–25°N).

The connection between aerosols over the AS and IP and rainfall over CEI was studied using MV-EOF. Responding to positive AOD variability over the AS, the IP, and adjacent areas, strong atmospheric heating centered over the IP was observed in the lower troposphere resulting in enhanced southwesterly and northwesterly wind anomalies over the AS and AP, respectively. The enhanced southwesterly winds over the AS can transport more water vapor to the Indian subcontinent, causing a positive rainfall anomaly over CEI. Meanwhile, since the dust emission highly depends on wind speed in the AP (Fecan et al., 1999), the enhanced northwesterly winds generate and transport more dust from the AP to the AS and IP, forming a positive feedback loop. This dust-monsoon interaction mechanism is similar to the "EHP" effect, but is located over the IP.

The cross correlation analyses not only confirm the dust–monsoon connections, but also characterize the timescales of these connections. The timescale of surface wind over

the AP affecting AOD over the AS and IP is about 3 days; for AOD–rainfall (over CEI), the timescale is about 13 days; for wind–rainfall, it is about 17 days. These lagged relationships may contribute to a more accurate ISM rainfall forecast.

One issue of this study is that multiple factors can influence the ISM system. Although MV-EOF can capture the spatiotemporal connection of various components, it is difficult using observational data alone to isolate and quantify the contribution of each individual component to the ISM system. Vinoj et al. (2014) studied the impacts of various aerosol types on ISM rainfall using a global climate model. They attributed the observed positive correlation between AOD over the AS, West Asia, and the AP and ISM rainfall to dust-induced atmospheric heating and associated large-scale convergence over North Africa and the AP, which result in an increased moisture transport to India within a week. Our observation-based study shows an EHP effect located over the IP and its surrounding areas, which results in a heat low that may be responsible for the intensified ISM circulation and rainfall. Satellite datasets show very limited aerosols in Egypt, Sudan, and Libya in North Africa, but higher AOD over the IP, the AP, and the AS. Therefore, it is more likely that the EHP located over the IP due to dust aerosols is responsible for this dust–monsoon correlation. Our future work will involve the use of high-resolution regional climate models coupled with chemistry to test the proposed physical mechanism that explains how the dust aerosols in the Middle East and IP influence the ISM system. Because dust loading has increased considerably during the last decade over the AP, the AS, and the IP [*Hsu et al.*, 2012], our findings may provide guidance for studying aerosol–rainfall interactions on longer time scales.

Chapter 3: Consistent Response of Indian summer Monsoon to Middle East Dust in Observations and Simulations

3.1 ABSTRACT

The response of the Indian summer monsoon (ISM) circulation and precipitation to Middle East dust aerosols on intraseasonal timescales is studied using observations and the Weather Research and Forecasting model with chemistry (WRF-Chem). Satellite data shows that the ISM rainfall in coastal southwest India, central and northern India, and Pakistan are closely associated with Middle East dust aerosols. The physical mechanism behind this dust-ISM rainfall connection is examined through ensemble simulations with and without dust emission. Each ensemble includes 16 members with various physical and chemical schemes to consider the model uncertainties in parameterizing shortwave radiation, the planetary boundary layer, and aerosol chemical mixing rules. Experiments show that dust aerosols increase rainfall by about 0.44 mm day^{-1} (~10%) in coastal southwest India, central and northern India, and northern Pakistan, a pattern consistent with the observed relationship. The ensemble mean rainfall response over India shows much stronger spatial correlation with the observed rainfall response than any of the ensemble members. The largest modeling uncertainties are from the boundary layer schemes, followed by shortwave radiation schemes. In WRF-Chem, the AOD over the Middle East shows the strongest correlation with the ISM rainfall response when AOD leads rainfall response by about 11 days. Further analyses show that the increased ISM rainfall is related to the enhanced southwesterly flow and moisture transport from the Arabian Sea to the Indian subcontinent, which are associated with the development of an anomalous low pressure system over the Arabian Sea, the southern Arabian Peninsula, and the Iranian Plateau due to dust-induced heating in the lower troposphere (800–500 hPa). This study demonstrates a thermodynamic mechanism that links remote desert dust emission in the

Middle East to the ISM circulation and precipitation variability on intraseasonal timescales, which may have implications for ISM rainfall forecasts.

3.2 INTRODUCTION

Aerosols, from both natural sources (e.g. mineral dust, sea-salt, and volcanic eruptions) and anthropogenic emissions (e.g. black carbon and sulfate) can influence climate by scattering and absorbing solar and terrestrial radiation (the direct effect) and by serving as cloud condensation nuclei and altering cloud microphysical properties (the indirect effect). The Indian summer monsoon (ISM) region and its surrounding areas have been identified to have high aerosol concentrations (Kuhlmann and Quaas, 2010) and this large aerosol loading has been increasing dramatically during the past decade due to population growth and more frequent dust activity (Hsu et al., 2012). The potential impacts of aerosols on ISM is an important issue because half of the world's population rely heavily on the ISM rainfall for water supply and agricultural production.

Both observational and modeling studies suggest that local anthropogenic aerosols, especially black carbon, over northern India have major impacts on ISM through the "solar dimming effect" and the "elevated heat pump effect" on different timescales (Ramanathan et al., 2005; Lau and Kim, 2006; Wang et al., 2009b; Kuhlmann and Quaas, 2010; Nigam and Bollasina, 2010; Bollasina et al., 2011; Lau and Kim, 2011; Nigam and Bollasina, 2011; Bollasina et al., 2013; Bollasina et al., 2014). In addition to local anthropogenic aerosols, remote mineral dust aerosols, which dominate the aerosol concentrations in the Middle East and the Arabian Sea (AS), can play an important role in altering the ISM rainfall. Wang et al. (2009a) found that dust aerosols can absorb solar radiation in a way similar to black carbon in the ISM and nearby regions. Using CALIPSO satellite retrievals, Kuhlmann and Quaas (2010) examined the aerosol constituents and concluded that the AS

has heavy dust loading with up to 80% of measurements identified as either dust or polluted dust during the Asian summer monsoon season. Jin et al. (2014) (2014; hereafter J2014) found that dust aerosols contribute 53% of the total AOD over the AS and the Iranian Plateau (IP) during the ISM season based on aerosol reanalysis.

The above studies have documented spatiotemporal features of mineral dust in the Middle East and the ISM surrounding regions, but have not focused on the impacts of remote Middle East dust on the ISM system. Until recently, general circulation model (GCM) experiments and observational analyses have demonstrated significant impacts of remote Middle East dust aerosols on the ISM rainfall. Vinoj et al. (2014) (2014; hereafter V2014) found a positive relationship between the ISM rainfall in southern India and dust aerosols over the AS, West Asia and the Arabian Peninsula (AP) using a GCM. They proposed that dust-induced convergence over eastern North Africa and the AP by heating the atmosphere increases moisture transfer over India, which in turn modulate monsoon rainfall over south India within a week. Based on satellite retrieved AOD and rainfall and meteorological reanalysis, J2014 proposed an AOD-ISM rainfall hypothesis based on a dust-induced "elevated heat pump effect" (EHP) centered over the IP and extending southward to the AS. By connecting the dust and ISM, this hypothesis explains the observed positive correlation between Middle East dust and ISM rainfall. Although V2014 and J2014 proposed a similar physical mechanism for the AOD-ISM rainfall correlation, the spatial patterns of increased ISM rainfall from their studies are quite different. In V2014, the rainfall response was found only in southern and central India and mainly located in south India, with only a minor increase or even decrease in rainfall in central India. However, in J2014, increased rainfall was observed in Pakistan and all of India except for southeast India; the largest increase in rainfall was located in the Indo-Gangetic Plain (IGP) region. In addition, V2014 stated no cross-correlation between AOD and ISM

rainfall within a week in observations, but J2014 found a significant cross-correlation with its maximum occurring when AOD leads ISM rainfall by 13 days. Most recently, Solmon et al. (2015) (2015; hereafter S2015) studied the interaction between Middle East dust and ISM rainfall on interannual to decadal timescales using a regional climate model (RCM) and found that the dust increased rainfall in southern India, while it decreased rainfall in central and northern India (CNI) and Pakistan during the period of 2000 to 2009. All three studies have focused on the dynamic impact of dust radiative forcing on the ISM rainfall, but their results differ or have opposite signs in terms of spatial distributions of the rainfall response in central and north India and Pakistan.

Our study uses observations and model experiments to understand the discrepancies among the above studies. We have three research questions. First, in what areas is rainfall sensitive to Middle East dust aerosols? The AOD-ISM rainfall relationship based on observations can provide a baseline for model evaluations. Secondly, how are the observed AOD-ISM interactions represented in the Weather Research and Forecasting model (Skamarock et al., 2005) with chemistry (WRF-Chem) (Grell et al., 2005)) and how do the modeling uncertainties affect our conclusions? In V2014, 19 ensemble simulations were conducted during a short period (10 days). In S2015, three ensemble simulations were created by perturbing the boundary conditions. In our study, 16 pairs of ensemble simulations are conducted using a perturbed physics and chemistry ensemble (PPCE) method during the boreal summer 2008, a period with strong dust emission. We believe that by using PPCE members we can better capture the uncertainties in the monsoon response to dust because the AOD-ISM rainfall hypothesis is based on both chemical properties (e.g. aerosol chemical mixing rules) of dust and their impact on atmospheric physical processes (e.g. radiation and circulations) (McFiggans et al., 2006). The dust-induced impact is then examined by the ensemble mean differences. Finally, is the 13-day

maximum cross-correlation found in observations in J2014 captured by WRF-Chem? This question is critical because if the AOD-ISM rainfall hypothesis is true, AOD must lead the ISM rainfall in the model.

3.3 Model and Experiment

3.3.1 Model

The Weather Research and Forecast model (WRF) is a state of the art mesoscale numerical weather prediction model, developed at the National Center for Atmospheric Research (NCAR). It incorporates multiple options for various physical schemes, such as microphysics, cumulus, radiation, land surface, planetary boundary layer, and so on. Incorporation of multiple options makes WRF used in a wide range of meteorological applications across spatial scales from tens of meters to thousands of kilometers.

WRF with online chemistry (WRF-Chem) The Weather Research and Forecasting model (Prospero et al., 2002) with online chemistry (WRF-Chem) (Grell et al., 2005) simultaneously simulates fate/evolution of trace gases and aerosols and their interactions with meteorological fields. The WRF-Chem model incorporated the second-generation Regional Acid Deposition Model (RADM2) gas phase chemical mechanism (Stockwell et al., 1997) and the Modal Aerosol Dynamics Model for Europe (MADE) primary aerosol scheme (Schell et al., 2001) coupling the Secondary Organic Aerosol Model (SORGAM) aerosol scheme for simulating secondary organic aerosol (SOA) formation from biogenic and anthropogenic emissions (Ackermann et al., 1998). RADM2 uses a simplified lumped molecular approach with surrogate species, which classifies species based on similarity in oxidation reactivity and emission magnitudes (Middleton et al., 1990), to represent atmospheric chemical compositions. RADM2 treats 63 gas phase species, including 21 inorganic and 42 organic species. 21 photolysis and 124 thermal reactions are included in

RADM2 to simulate the main gas phase chemical reactions. The Carbon Bond Mechanism version Z (CBM-Z) phase gas chemical mechanism (Zaveri and Peters, 1999) and Model for Simulating Aerosol Interactions and Chemistry (MOSAIC) aerosol scheme (Zaveri et al., 2008) were also incorporated into WRF-Chem. CBM-Z uses a lumped structure approach, in which species are categorized according to the similarity in the reactions of carbon bonds. CBM-Z treats 52 gas phase species, including 16 inorganic and 36 organic species, and simulating 16 photolysis and 116 thermal reactions. The advantage of CBM-Z against RADM2 is that CBM-Z always conserve carbon mass, but it compromises on better representation of gas phase species and their interactions. Although RADM2 and CBM-Z are based on various assumptions associated with each lumping method, they show similar performance in simulating key species in the atmosphere (Zaveri and Peters, 1999).

3.3.1.1. Aerosol Species and Size Representation

The major aerosols species treated in both MADE-SORGAM and MOSIAC include sulfate, nitrite, ammonium, soil-derived dust, organic carbon (OC), black carbon (BC), sea salt, and water. In addition, MOSAIC also treats calcium carbonate and methane sulfonic acid. Modal and sectional approaches are used to represent aerosol size distribution in MADE-SORGAM and MOSAIC, respectively. Modal approach has three overlapping modes: Aitken (0.01−0.1 μm), accumulation (0.1−1.0 μm), and coarse modes (1.0−10.0 μm), assuming a lognormal distribution within each mode (Liu et al., 2012; Albani et al., 2014; Mahowald et al., 2014). Sea salt, soil-derived dust, and anthropogenic emissions are treated in coarse mode, and other aerosol species are treated in both Aitken and accumulation modes. Sectional approach has eight size bins (0.039−0.078 μm, 0.078−0.156 μm, 0.156−0.312 μm, 0.312−0.625 μm, 0.625−1.25 μm, 1.25−2.5 μm, 2.5−5.0 μm, and 5.0−10.0 μm dry diameter). Aerosols are assumed internally mixed within

each mode or bin so that all particles have the same chemical composition, and externally mixed between modes or bins.

3.3.1.2. Aerosol Formation

The particles are formed by direct particle emission and secondary formation of nucleation. Direct emission include emission from biomass burning, anthropogenic emission, soil-derived dust, sea salt, and so on. Nucleation dynamic is incorporated to take into account the formation of secondary aerosols in sulfuric acid-water conditions (Kulmala et al., 1998). There is no explicate mode for nucleation simulated in current MADE, so all freshly formed particles are assigned to Aitken mode, assuming a median diameter of 10 *nm* and a standard deviation of 1.6 *nm*.

3.3.1.3. Aerosol Growth

The growth of aerosol particle size by vapor condensation is calculated based the rate of change of third moment of aerosol size lognormal distribution by neglecting the Kelvin effect (Binkowski and Shankar, 1995). The production rate of vapor condensation is calculated by RADM2 chemistry scheme. Since aerosol particle size is defined as dry particle radium, the condensation does not cause particle shift between modes or bins. Coagulation caused by Brownian motion is considered in MADE. The collision of particles within one mode can form a new particle in that mode; the collision of particles from two different modes can form a new particle in the mode with larger diameter (Whitby and McMurry, 1997).

3.3.1.4. Dry Deposition

Dry deposition of trace gases is calculated using dry deposition velocity, which is parameterized by aerodynamic, sub layer, and surface resistance (Wesely, 1989). Dry deposition of aerosols is calculated using gravitational sedimentation velocity (Wesely,

1989), resistance due to interception (Ruijgrok et al., 1995; Zhang et al., 2001), impaction (Peters and Eiden, 1992), and Brownian motion (Binkowski and Shankar, 1995).

3.3.1.5. Wet Scavenging

Wet deposition of both trace gases and aerosols in-cloud and below-cloud are treated in the model. Cloud-borne aerosols through activation and Brownian diffusion and cloud water-dissolved trace gases are assumed to be immediately removed from the atmosphere by collection of rainfall, ice, snow, and graupel. The removal rate of cloud-borne aerosols and trace gases is approximately identical to the removal rate of cloud water by precipitation, which is calculated by microphysics scheme in the model (e.g. Lin microphysics scheme). Below-cloud scavenging of aerosols by precipitation through impaction and interception and trace gases by rainfall are also treated following (Easter et al., 2004).

3.3.1.6. Aerosol Optical Properties

Each aerosol species is assigned a complex refractive index, with its real part indicating phase velocity of scattering and its imaginary part indicating absorption when solar radiation propagates through the atmosphere. In WRF-Chem, mineral dust aerosols are assigned the wavelength-independent refractive index ($1.550+i0.003$) within the shortwave (SW) range. However, the absorbing ability of dust aerosols decreases as wavelength increases (Wagner et al., 2012; Utry et al., 2015). Therefore, in this study wavelength-dependent refractive indices are employed from the Rapid Radiative Transfer Model GCM application (RRTMG) SW radiation scheme (Iacono et al., 2008) in the Community Atmosphere Model. The imaginary parts of the refractive indices are 0.024, 0.0135, 0.0063, and 0.004 for wavelengths at 300, 400, 600, and 999 nm, respectively. The real part of dust refractive index is the same as in the default WRF-Chem. Aerosol optical

properties such as optical depth, single scattering albedo, asymmetry factor, extinction, and backscatter coefficient are calculated in three dimensions at the abovementioned 4 SW wavelengths using Mie theory. For longwave radiation, aerosol optical depth and extinction coefficient are calculated at 16 wavelengths (3.4−55.6 μm).

3.3.2. Emissions

3.3.2.1. Dust Emission

The Goddard Chemistry Aerosol Radiation and Transport (*GOCART*) dust emission scheme (Ginoux et al., 2001) coupled with the MADE-SORGAM aerosol scheme is used to simulate dust emission. In GOCART, dust emission is calculated based on wind speed and an erodibility map (Prospero et al., 2002; Zender et al., 2003b) as

$$G = CSs_p u_{10m}^2 (u_{10m} - u_t) \quad (3.1)$$

G: dust emission flux (μg m^{-2} s^{-1})

C: dimensionaless empirical proportionality constant

S: soil erodibility of potential dust source regions (Figure 3.1b)

s_p: a fraction of mass of each size bin of total dust emission

u_{10m}: wind speed at 10 m above the surface

u_t: wind speed threshold under which dust emission does not occur

GOCART represents dust emission in 5 bins, with averaged radii of 0.73, 1.40, 2.40, 4.50, and 8.00 μm. The computed dust emission are divided into the accumulation and coarse modal modes for MADE-SORGAM to match the representation of particle size distribution in the aerosol scheme.

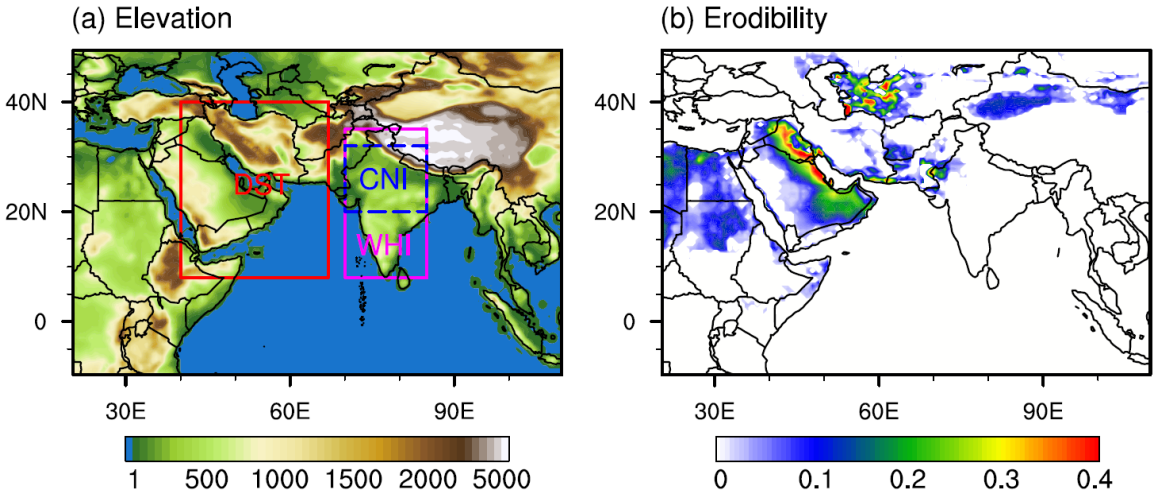

Figure 3.1. (a) Elevation map in WRF-Chem domain (unit: m). "DST", "WHI", and "CNI" represent the remote dust region (8°–40° N, 40°–67° E), the entire India (8°–35° N, 70°–85° E), and the central and northern India (20°–32° N, 70°–85° E), respectively. (b) Soil erodibility (unitless) map used in WRF-Chem dust emission scheme.

3.3.2.2. Other Emissions

The anthropogenic emissions for WRF-Chem come from the mixture of the Reanalysis of the Tropospheric chemical composition emissions inventory (http://retro.enes.org/index.shtml), Emission Database for Global Atmospheric Research (http://www.mnp.nl/edgar/introduction), and GOCART. These anthropogenic emissions include 20 gases and 3 aerosol species, including BC, OC, and sulfate. Background emissions are from GOCART dataset, including nitrate, H_2O_2, hydroxyl radical, and DMS. Biogenic emissions are calculated online using the Model of Emissions of Gases and Aerosols from Nature (Guenther et al., 2012). Biomass burning emissions are obtained from the Global Fire Emissions Database version 2 with 8-day temporal resolution (http://www.globalfiredata.org/index.html).

3.3.3. Experiment Design

In this study, WRF-Chem 3.5 is configured over the Middle East and the ISM region (9.68° S–49.60° N, 20.41°–109.87° E, see Figure 3.1a) with 160×120 grid points centered over the AS (23° E, 65° N), at a 54-km horizontal resolution and 30 vertical layers up to 50 hPa. This domain covers major dust source regions represented by erodibility in the model, as shown in Figure 3.1b. A few key areas are selected to examine the relationship between Middle East dust and the ISM rainfall. The DST box is chosen to include the heavy dust loading areas, i.e. the AS, the AP, the IP, Afghanistan, and Turkmenistan. The WHI box and CNI boxes are chosen to represent the rainfall over the whole India and central and northern Indian, respectively.

All simulations cover a 104-day period from 20 May 2008 to 31 August 2008 without nudging. The first 12 days for each integration are discarded as "spin up" to reduce the impact of initial conditions, and the analysis focuses on the monsoon season from 1 June 2008 to 31 August 2008. Meteorological fields from the European Centre for Medium-Range Weather Forecasts (ECMWF) Interim Reanalysis (ERA-I) global reanalysis data are prescribed as lateral and lower boundary conditions (e.g. SST) and initial conditions.

WRF-Chem provides multiple options for physical and chemical parameterizations. For physical parameterizations, we used the Noah land surface model (Chen et al., 2001; Dai et al., 2013), the RRTMG SW and longwave (LW) radiation scheme, Yonsei University (YSU) planetary boundary layer (PBL) scheme (Hong et al., 2006), and Lin's second-moment microphysical scheme (Lin et al., 1983). An updated version of the Grell-Devenyi (Grell and Devenyi, 2002) cumulus parameterization scheme is used, which includes feedback from the parameterized convection to the atmospheric RRTMG radiation scheme and Fast-J photolysis scheme. For the chemical

parameterizations, we used RADM2 gas-phase chemistry, MOSAIC-SORGAM aerosol chemistry with aqueous reactions, and Fast-J photolysis scheme. Table 3.1 summarizes the model schemes used in this study.

Table 3.1. Configuration options of WRF-Chem used in this study.

Atmospheric Process		Model Option
Physics	Longwave radiation	RRTMG
	Shortwave radiation	RRTMG-Goddard
	Surface layer	Monin-Obukhov
	Land surface	Noah
	Boundary layer	YSU/BouLac
	Cumulus clouds	Grell-Freitas
	Cloud microphysics	Lin et al.
Chemistry	Gas-phase chemistry	RADM2
	Aerosol chemistry	MOSAIC-SORGAM with aqueous reactions
	Photolysis	Fast-J
Emission	Dust emission	GOCART
	Sea-salt emission	MADE/SORGAM
	Anthropogenic emission	Reanalysis of the Tropospheric and Emission Database for Global Atmospheric Research
	Biogenic emission	The Model of Emissions of Gases and Aerosols from Nature version 2
	Fire emission	MODIS

To understand how the model uncertainties and errors affect our results, additional alternative physical and chemical parameterization schemes are used to create ensemble simulations. V2014 and S2015 created ensemble members by perturbing initial and boundary conditions, respectively. In this study, two groups of simulations were designed based on the presence and absence of dust emission. The reference group considers all aerosol forcing (including mineral dust, sea salt, biomass burning, biogenic emission, and anthropogenic emission; ALLF) and the perturbed group is identical to the first group but without dust emission (NDST). Within each group, 16 ensemble members were created using the PPCE method, because we are more interested in how differences in the aerosol

chemical mixing rules, aerosol diffusion in the atmospheric boundary layer, and radiation schemes may affect the simulations of the ISM rainfall and variability.

Four different aerosol chemical mixing rules are used to calculate the aerosol optical properties: volume approximation, Maxwell-Garnett approximation, exact volume, and exact Maxwell-Garnett schemes (Fast et al., 2006; Barnard et al., 2010). The volume approximation assumption calculates refractive indices based on the volume average of each aerosol species. The Maxwell-Garnett method assumes a random distribution of black carbon in spherical particles. Both of the volume and Maxwell-Garnett schemes call the full Mie calculation only at the first time step (Ghan et al., 2001). However, the exact volume and exact Maxwell-Garnett schemes call the full Mie calculation at each time step.

Two SW radiation schemes—RRTMG and Goddard, and two PBL schemes—YSU and Bougeault-Lacarrère (BouLac) are employed. The sub-grid cloud parameterization in RRTMG can simulate interactions between aerosol radiative forcing and sub-grid clouds. YSU and BouLac represent two types of PBL schemes—turbulent kinetic energy and first-order closure schemes (Shin and Hong, 2011). Totally, there are 32 ensemble members, which are comprised of 2 PBL×2 SW×4 composition×2 dust options as detailed in Table 3.2. Note that the LW radiation induced uncertainties are not considered in this study, because only the RRTMG LW radiation scheme is coupled with the aerosol scheme.

Table 3.2. Various schemes employed to create the ensemble members.

Scheme	Option		Description
Shortwave radiation	sw4	Goddard	1. 11 spectral bands (7 UV, 1 PAR, 3 infrared), 2. A two-stream adding algorithm 3. No interacts with sub-grid clouds
	sw2	RRTMG	1. 14 spectral bands (3 UV, 2 PAR, 9 infrared), 2. A two-stream algorithm for multiple scattering 3. Represents sub-grid cloud variability by McICA with maximum-random cloud overlap.
Planetary boundary layer	pb1	YSU	1. First-order closure 2. *K* profile and non-local mixing 3. Explicit treatment of entrainment
	pb8	BouLac	1. One-and-a-half order closure 2. Prognostic turbulent kinetic energy equation
Aerosol Chemical mixing rules	op1	Volume	1. Internal-mixing of aerosol composition 2. Full Mie calculations are called only at the first time step
	op2	Maxwell	1. Randomly distributes black carbon within a particle 2. Full Mie calculations are called only at the first time step
	op3	Exact volume	Same as volume, but use full Mie calculation at each time step
	op4	Exact Maxwell	Same as Maxwell, but use full Mie calculation at each time step

UV, PAR, and McICA stand for ultraviolet, photosynthetically active radiation, and the Monte Carlo Independent Column Approximation, respectively.

3.4. DATASETS

3.4.1. AOD

The Moderate-resolution Imaging Spectroradiometer (MODIS) instrument aboard the National Aeronautics and Space Administration (NASA) Terra and Aqua platforms is uniquely designed to observe and monitor atmospheric trace gases, clouds, and tropospheric aerosols. MODIS provides two kinds of AOD data, “dark target” and “deep-blue” daily and monthly AOD at the wavelength of 550 nm with resolution of $1^{o} \times 1^{o}$ from

March 1, 2000 to the present (http://ladsweb.nascom.nasa.gov/data/search.html). The "dark target" algorithm provides best results over the oceans and on land with low surface albedo; the "deep-blue" algorithm retrieves AOD over regions with bright surfaces, such as desert (Hsu et al., 2004). In our study, both kinds of AOD are combined to expand the spatial coverage by simply assigning the "deep-blue" AOD to the grid if the "dark target" AOD is missed. In this way, the global AOD is available over both oceans and land. Because of a broad swath—2330 km, MODIS images the entire earth every 1–2 days.

The Multi-angle Imaging Spectroradiometer (MISR) instrument provides detailed aerosol properties at the global scale. MISR onboard Terra, NASA's first Earth Observing System spacecraft, is designed to improve our understanding of the regional and global impacts of different types of atmospheric particles and clouds on climate (Diner et al., 1998). With nine cameras, MISR views Earth in nine different directions, and each piece of Earth's surface below is successively imaged by all nine cameras, in each of four wavelengths (blue, green, red, and near infrared). This specific feature of MISR can help estimate aerosol particle size and composition with unprecedented accuracy. Based on the particle size information, the aerosol's effects on climate caused by natural sources and human activities can be isolated. The swath for MISR is only 360 km, which gives MISR a longer global span time of 9 days.

The ECMWF Monitoring Atmospheric Composition and Climate (MACC) ($0.5° \times 0.5°$) reanalysis data provide partial AOD of various aerosol types (Benedetti et al., 2009). MACC assimilates MODIS dark target production collection 5, which does not include AOD retrievals over the bright surface using the "deep-blue" algorithm.

3.4.2. Precipitation

Four precipitation datasets are used. The Tropical Rainfall Measuring Mission (TRMM) (0.25° × 0.25°) monthly 3B43 (version 7) and daily 3B42 (version 7) precipitation datasets are employed (Huffman et al., 2007). These two products combine multiple independent satellite precipitation estimates and Global Precipitation Climatology Centre rain gauge analysis. The Global Precipitation Climatology Project (GPCP) (1° × 1°) monthly and daily (version 2) rainfall datasets are produced by combining multiple satellite retrieved precipitation and surface precipitation gauge analyses (Huffman et al., 2001). The Climate Prediction Center Merged Analysis of Precipitation (CMAP) (2.5° × 2.5°) monthly and pentad rainfall datasets are produced based on five kinds of satellite retrievals (Xie and Arkin, 1997). The National Oceanic and Atmospheric Administration PRECipitation REConstruction over land (PREC/L) (0.5° × 0.5°) monthly rainfall datasets are constructed by precipitation gauge observations (Chen et al., 2002).

3.4.3. Reanalysis

ERA-I (0.5° × 0.5°) (Rienecker et al., 2011) is adopted to provide WRF-Chem with lateral and lower boundary conditions, as well as initial conditions. The Modern Era-Retrospective Analysis for Research and Applications (MERRA) (1/2° × 2/3°) (Dee et al., 2011) is also used for comparison with ERA-I and model evaluation in terms of geopotential height (GPH) and circulations.

3.5. Evaluation of ISM and AOD Simulated by WRF-Chem

Figures 3.2a–3.2c illustrate the spatial patterns of the observed and modeled rainfall averaged for June–July–August (JJA) 2008. During the ISM season, TRMM and GPCP observed heavy rainfall in coastal southwest India (CSWI) and CNI. The WRF-Chem ensemble mean rainfall in 16 ALLF members (Figure 3.2c) shows a spatial pattern quite

consistent with that of TRMM and GPCP. Note that the model overestimates rainfall in CSWI and underestimates rainfall in CNI. Similar rainfall difference between model simulations and observations were also found in both RCM (e.g. Solmon et al., 2015) and GCM (e.g. Levine and Turner, 2012) studies. The underestimated rainfall in CNI can be partly attributed to the lack of representation of agricultural irrigation in the model. Intensive irrigation activities occurring during JJA over the IGP can increase local evapotranspiration, and thus increase rainfall (Douglas et al., 2009). Figures 3.2d–2f show the GPH and circulation at 850 hPa from reanalysis and WRF-Chem. The ISM system is featured by strong cross-equator southerly winds in the tropical Indian Ocean and southwesterly winds in the lower troposphere in the AS and the Bay of Bengal. Another ISM feature is the deeper low-pressure centered over north India and the IP. In general, the model can capture the ISM features quite well.

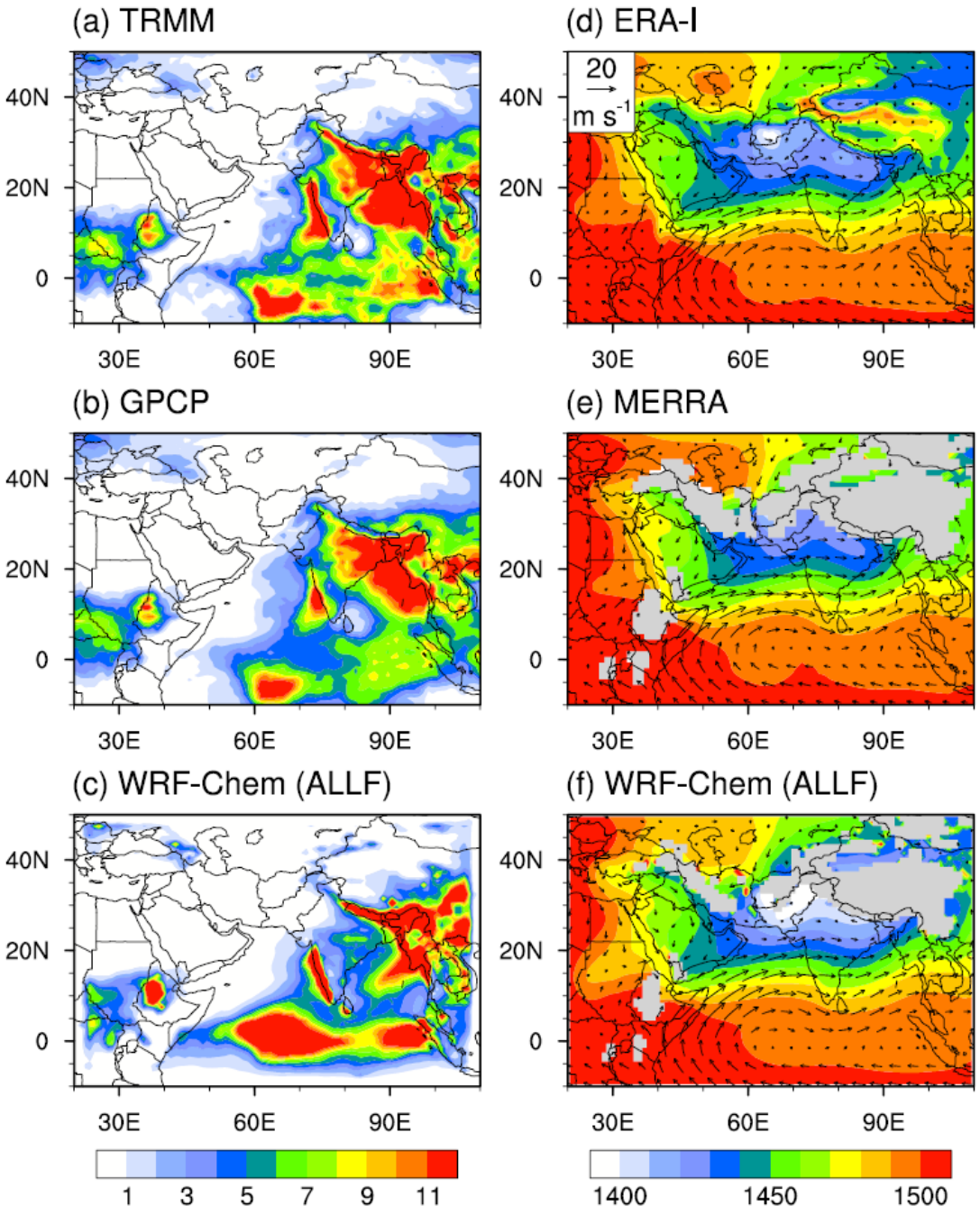

Figure 3.2. (Left) Precipitation (mm day^{-1}) from (a) TRMM, (b) GPCP, (c) WRF-Chem (ALLF). (Right) 850 hPa GPH (shading; unit: m) and wind (arrows; units: m s-1) from (d) ERA-I, (e) MERRA, (f) WRF-Chem (ALLF). All variables are average for JJA 2008. In Figures (e) and (f), topography is masked out in grey.

A reliable representation of the spatial distribution of dust concentration in the model is essential for examining dust impacts on the ISM rainfall. The modeled AOD at 300, 400, 600, and 999 nm are converted to 550 nm using the Ångström exponent and evaluated using satellite retrieved AOD, which is usually at 550 nm. By tuning the empirical proportionality in Equation (1) against satellite AOD, the spatial pattern of modelled AOD is quite consistent with multiple satellite retrievals and aerosol reanalysis results. Figure 3.3 demonstrates that WRF-Chem captures the observed high dust loading in the AP, the Thar Desert, and the IP. However, the model underestimates AOD over the northern AS and overestimates AOD in the southern AP in comparison to the other four datasets. Note that MISR, MODIS Aqua, and MACC show much higher AOD over the AS than the southern AP, whereas modeled AOD shows the opposite. This discrepancy between the modeled and satellite data could be attributed to two potential contributors. First, the assumption regarding dust mass distribution on dust particle size in the MADE-SORGAM aerosol scheme is not suitable for Middle East dust aerosols. In MADE-SORGAM, only 7% of the mass of total dust emission is assigned to the accumulation mode, whereas the other 93% percent goes into the coarse mode; consequently, most dust emission is deposited quickly in the dust source regions in the AP and only very little is transported long-distance to the AS. However, in the Mineral Dust Entrainment and Deposition model (Zender et al., 2003a), 17% of the mass of dust emission is assigned to the accumulation mode. Note also that the underestimation of fine particles reduces dust-induced atmospheric heating because fine particles absorb 3 to 5 times the solar radiation absorbed by coarse particles (Mahowald et al., 2014). Secondly, the model does not adequately represent the impact of relative humidity on AOD calculation. Increased relative humidity can lead to higher AOD because more water vapor can be taken up by dust particles, an effect known as aerosol humidification (Myhre et al., 2007).

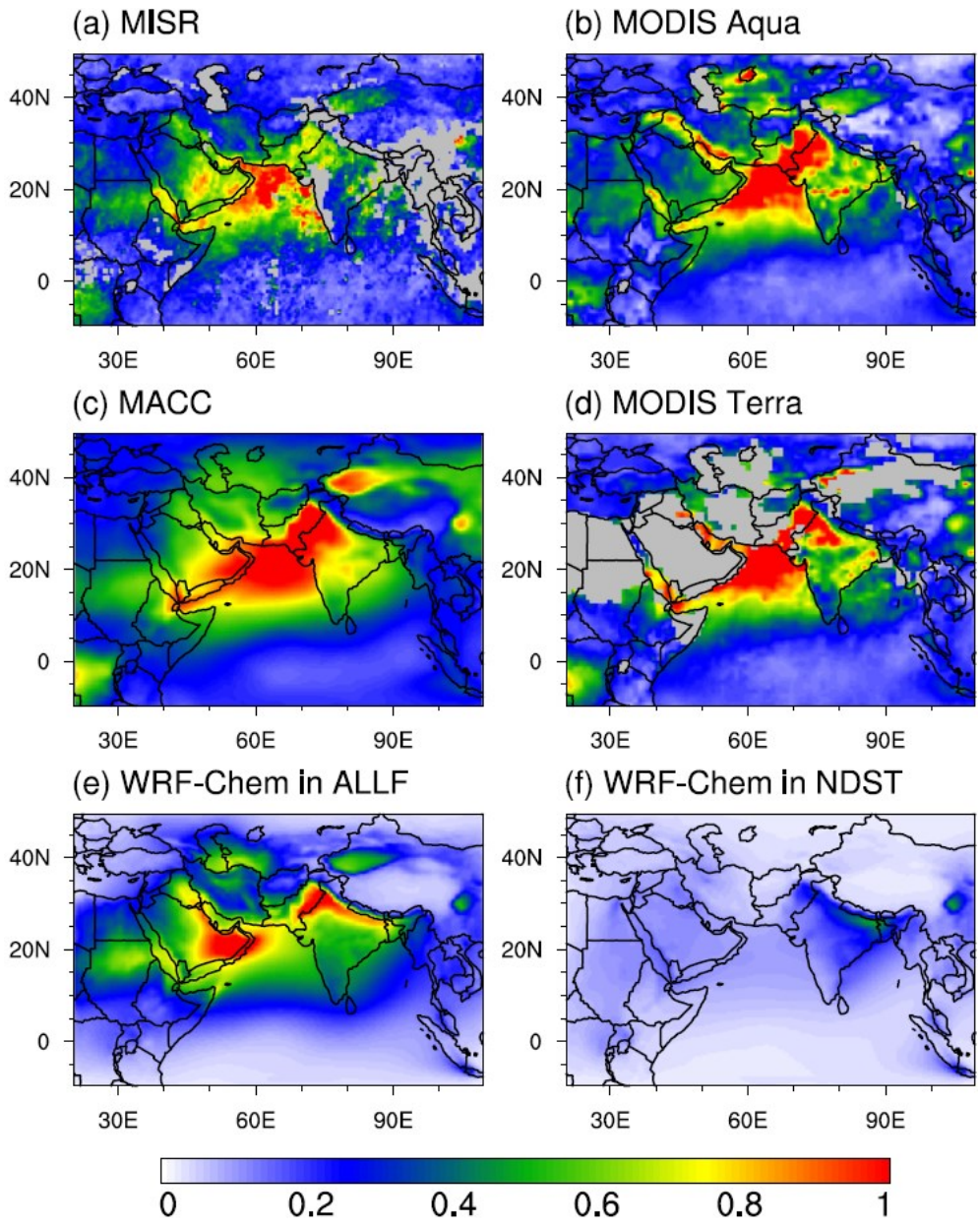

Figure 3.3. Spatial patterns of AOD (unitless) from (a) MISR (558 nm), (b) MODIS Aqua (550 nm), (c) MACC (550 nm), (d) MODIS Terra (550 nm), (e) WRF-Chem (ALLF; 550 nm), and (f) WRF-Chem (NDST; 550 nm) averaged for JJA 2008. Missing values are masked in grey in Figures (a), (b) and (d).

3.6. Observed Relationship between Dust and ISM Rainfall

The observed relationship between AOD and ISM rainfall is studied using regression analysis. Figure 3.4 shows the spatial patterns of AOD regressed on the area-averaged ISM rainfall in WHI using their JJA monthly anomalies during 2000 and 2013. Figure 3.4a shows the regressed AOD using MISR and NOAA observations. Positive anomalies of ISM rainfall in WHI are associated with heavy aerosol loading over the northern AS, the southern AP, and the IP. This spatial pattern of regressed AOD persists or becomes stronger in other AOD and rainfall datasets, as shown in Figures 3.4b–3.4d. Over northeastern India, dust is negatively correlated with rainfall because local dust is removed through wet deposition. This spatial pattern is consistent with the modeled atmospheric heating pattern induced by dust in Figure 3.12a, which will be discussed later.

To compare this observed dust-ISM rainfall relationship with model simulations, Figure 3.5 shows the precipitation regressed on the area-averaged AOD in the DST region. In general, the various datasets show a consistent spatial pattern. The positive response of rainfall to AOD is primarily located in the IGP, the central India, and CSWI, while a weak negative response is seen in southeast India. This observed north-positive and southeast-negative correlation patterns differ from the results of V2014 (Figure 4b in V2014) and is almost opposite to those of S2015 (Figure 5b in S2015), but it is very similar to our observation-based analysis in J2014 (Figure 2c in J2014). See Table 3.3 for a summary.

The regression analyses of AOD–ISM rainfall relationship based on observations provide a baseline for evaluating the model results.

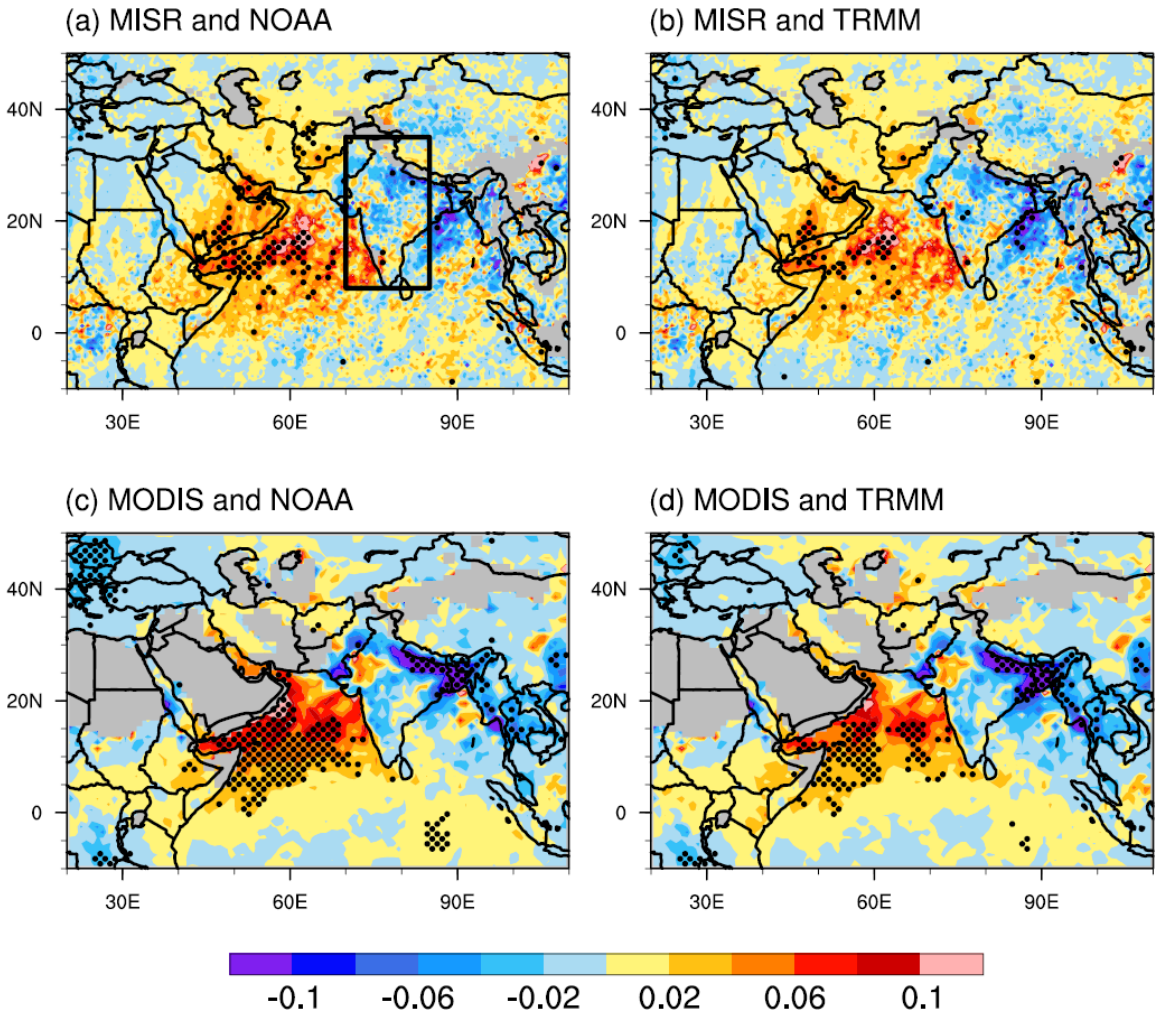

Figure 3.4. Spatial patterns of AOD regressed on area-averaged ISM rainfall in WHI (box in (a)) using JJA monthly anomalies from 2000 to 2013. Two different AOD datasets (MISR and MODIS Terra) and two different rainfall datasets (NOAA and TRMM) are used, so there are four different results. The black dots represent grid points that are 95% confident based on the *t*-test. Missing values are masked out in grey.

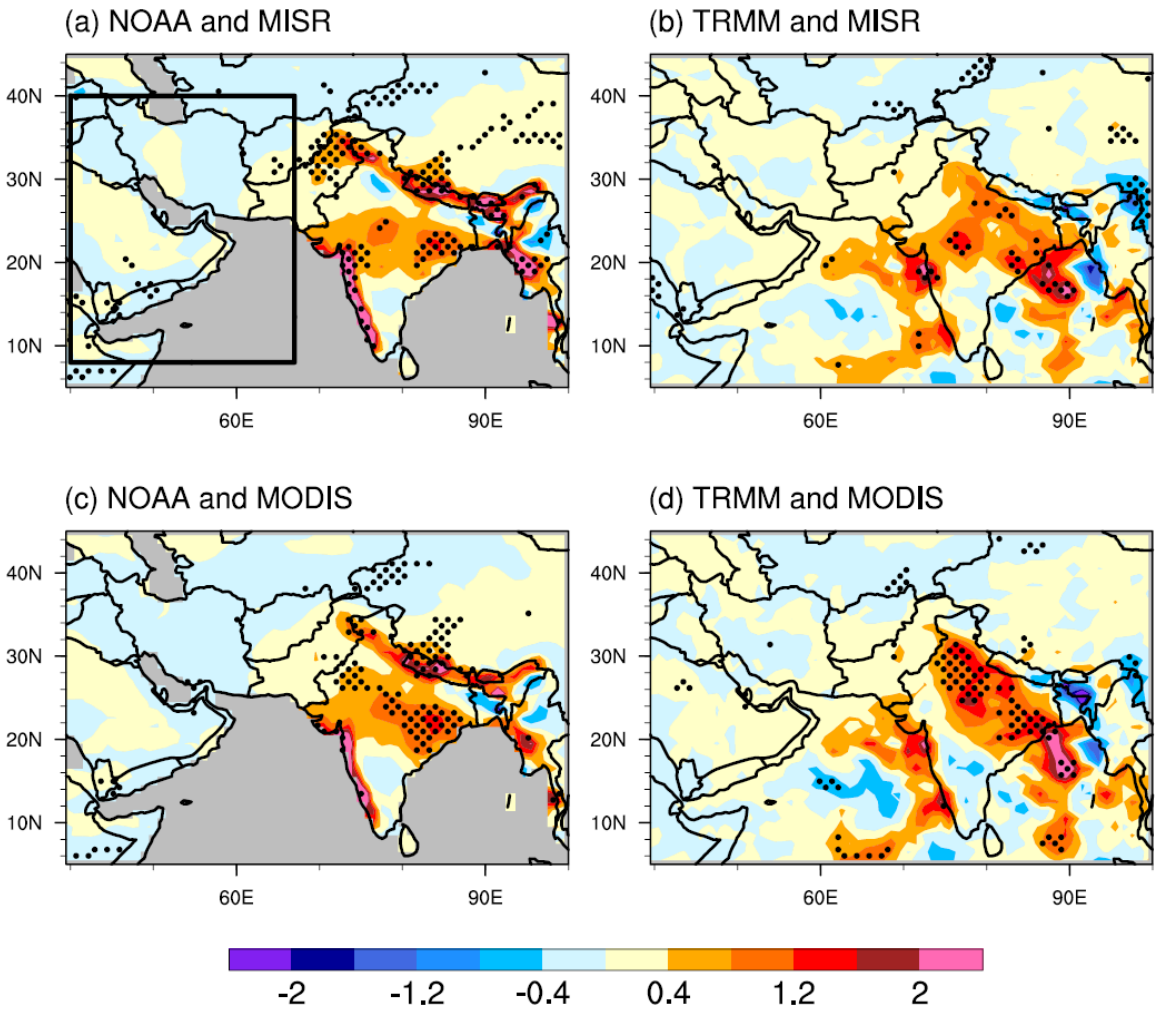

Figure 3.5. Same as Figure 3.4, but for the spatial patterns of precipitation (mm day^{-1}) regressed on area-averaged AOD in the AS, the south AP, and the IP (box in (a).

Table 3.3. Rainfall response in various regions of India to Middle East dust in this study and other references.

Reference		Pakistan	CNI	CSWI	Southeast India
This study	Satellite	+	+	+	–
	Model	+	+	+	–
V2014		Not shown	No change	+	+
J2014		+	+	+	–
S2015		–	–	+	+

"+" and "–" mean increased and decreased rainfall, respectively.

3.7. MODELED ISM RAINFALL RESPONSE TO DUST

The ISM rainfall response to Middle East dust is represented by the ensemble mean differences in rainfall from 16 ALLF and 16 NDST simulations. Figure 3.6a shows the spatial patterns of the total rainfall response averaged during JJA. In general, the total rainfall increases over most of India with an average magnitude of 0.44 mm day^{-1} (~10%) in WHI. The largest rainfall increases occur in CNI, northern Pakistan, and CWSI. Note that the spatial pattern of rainfall increase closely follows the topography along CSWI and the Tibetan Plateau, indicating that increased rainfall can be mainly related to large-scale circulation changes. Conversely, decreased rainfall is simulated in southeastern and northeastern India. The spatial pattern of the modeled rainfall response is generally consistent with the observed AOD-ISM rainfall relationship in Figure 3.5 and Figure 2.3c in Chapter 2 (see Table 3.3). Figure 3.6b illustrates the convective rainfall responses. The convective rainfall responses display consistently spatial increases across India, but the stratiform rainfall responses follow the topography in Figure 3.6c, which is similar to the total rainfall responses.

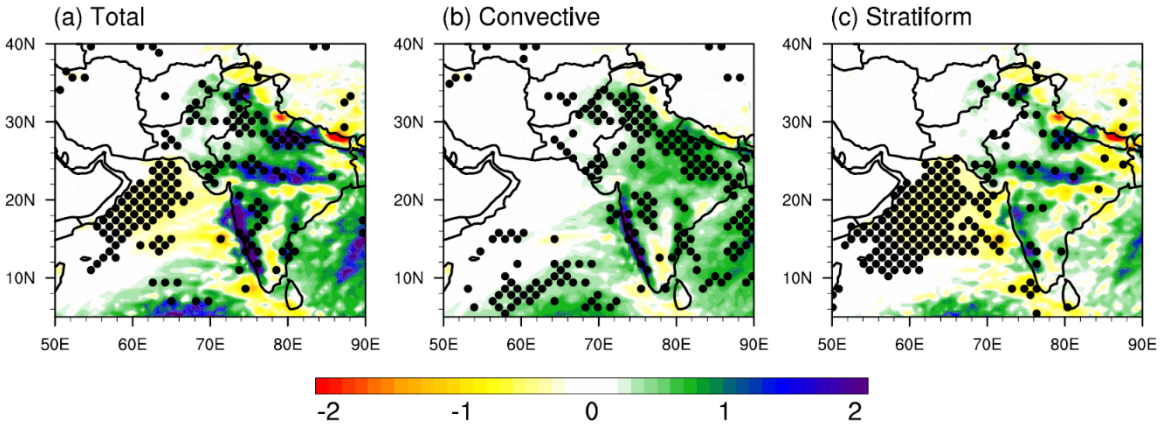

Figure 3.6. Spatial pattern of WRF-Chem ensemble mean differences in rainfall (mm day^{-1}) between AFFL and NDST experiments during JJA 2008. Areas that are confident at the 90% level based on a one-sided Student's *t*-test are dotted.

Figure 3.7 shows the spatial correlations between the regressed rainfall pattern in Figure 3.5c and rainfall responses in each of the 16 ensemble pairs (ALLF−NDST) as well as their ensemble mean. It can be seen that 15 out of 16 members show positive spatial correlations between the modeled rainfall response and regressed rainfall in observations, with a magnitude of 0.1 to 0.5, which indicates that most of the members can capture the observed spatial patterns of dust-induced rainfall changes. Interestingly, the rainfall response from the ensemble mean shows a spatial correlation of about 0.6, much larger than any of the ensemble members. This indicates that the ensemble mean may cancel out and reduce model errors raised from various parameterization schemes.

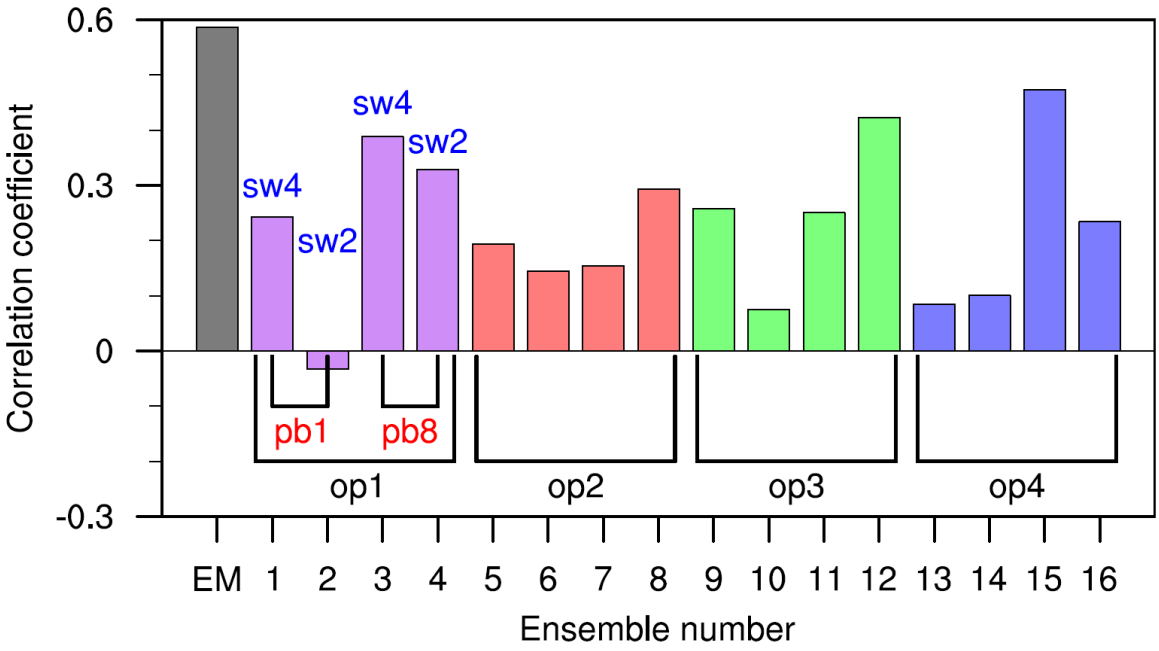

Figure 3.7. Spatial correlation coefficients between the regressed rainfall change pattern (Figure 3.5c) and the modeled rainfall response (Figure 3.6) from the ensemble members (marked by numbers from 1 to 16) and their ensemble mean (marked by "EM"). "EM" stands for the ensemble mean. The region for calculating the spatial correlation is WHI. Using other figures in Figure 3.5 for the evaluations gets similar results. See Table 3.2 for the denotations.

Figure 3.7 also illustrates that ensemble members 2, 6, 10, and 14 show very small correlation coefficients. These schemes share the same SW radiation and PBL schemes—Goddard and YSU. The low correlation coefficients are attributed mainly to the BouLac PBL scheme, because ensemble members 4, 8, 12, and 16 show high correlation coefficients and share the same SW radiation schemes but have a different PBL scheme—BouLac from members 2, 6, 10, and 14. Furthermore, the ensemble members using RRTMG SW radiation schemes generally show higher correlation coefficients than those using the Goddard SW radiation scheme, while those using the different aerosol chemical mixing rules show very little differences in correlation coefficients.

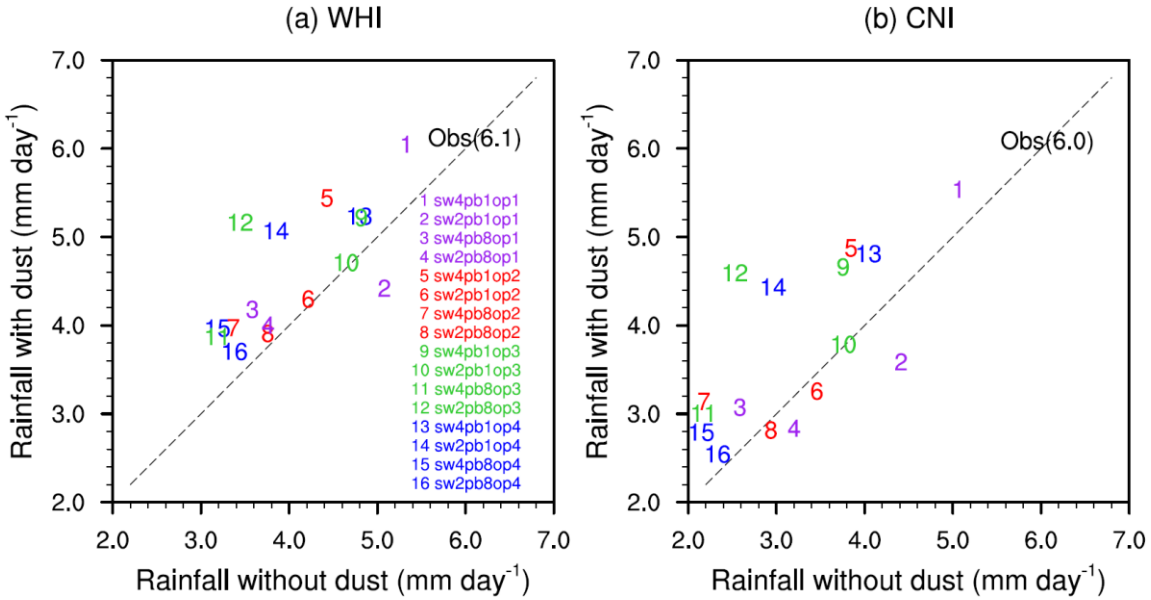

Figure 3.8. Scatter plot of area-averaged rainfall (mm day^{-1}) in WHI and CNI in 16 pairs of ALLF and NDST ensemble simulations and observations. "Obs" means averaged observational rainfall from TRMM, GPCP, and CMAP, with area-averaged mean values of 6.1 and 6.0 in parentheses in WHI and CNI, respectively. The ensemble numbers are the same as in Figure 3.7. See Table 3.2 for the denotations.

Figure 3.8 shows the scatter plot of the area-averaged rainfall in WHI and CNI in each ALLF ensemble member (y-axis) against NDST members (x-axis). In WHI, all members are located above or on the 1:1 line except the number 2, indicating that dust-induced rainfall increases are quite robust. Along with the number 2, which shows decreased rainfall, the numbers 4, 6, 8, 10, and 16 show very weak rainfall increase. These simulations share the same Goddard SW scheme. The situation is similar in CNI, but with more members showing decreased rainfall than in WHI. Therefore, we conclude that the largest effects on our simulation results are from the PBL scheme, followed by the SW radiation scheme, and the aerosol chemical mixing rule has a very weak effect.

Figure 3.9 shows the time series of WRF-Chem simulated daily rainfall in each ensemble member and the ensemble mean of rainfall response and AOD in ALLF simulations. In general, the model can capture the temporal variation of rainfall in July and August, with two peaks in early July and the first half of August in both the model runs and observations. The model has a notable low bias in June, which is larger in CNI than in WHI. This low bias could be attributed to irrigation, which occurs in spring and summer with maximum irrigation in May and June in IGP (Douglas et al., 2009). Ensemble means underestimate mean rainfall by one-third in NDST members during JJA 2008 in both WHI and CNI as shown in Figure 3.9. However, some ensemble members (thin blue and yellow lines in Figures 3.9a and 3.9b) do overestimate rainfall during specific days in WHI and CNI. The daily ensemble mean of rainfall response is shown in Figures 3.9c and 3.9d. In both WHI and CNI, increased rainfall is illustrated in most days during the entire period. However, the rainfall response does not change significantly in CNI until late June or early July, which is due to a late monsoon onset in CNI at the end of June (Moron and Robertson, 2014). The daily ensemble mean of the modeled area-averaged AOD in DST is also shown in Figures 3.9c and 3.9d for comparison with the rainfall response.

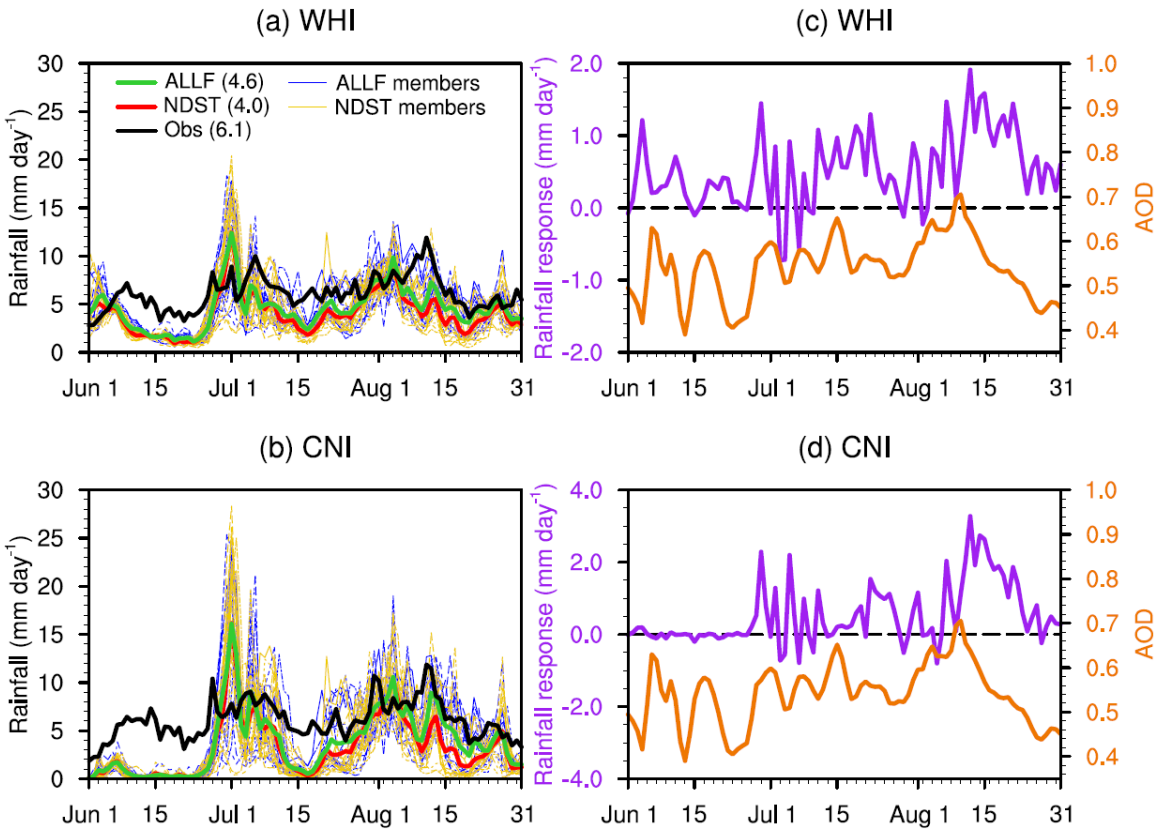

Figure 3.9. (Left) Time series of rainfall (mm day^{-1}) in 32 ensemble members and ensemble means of ALLF and NDST experiments and (Right) ensemble mean rainfall responses (mm day^{-1}) in WHI and CNI and AOD in DST (from ALLF). The numbers in parentheses are time-averaged rainfall.

Figure 3.10 shows the cross-correlation between the daily ensemble mean of rainfall response in WHI and CNI and AOD in DST. Both correlation coefficients become significant when AOD leads rainfall by 10 to 11 days, comparable to the observed 13-day lag shown in J2014. This provides further evidence for the causal relationship between Middle East dust and ISM rainfall.

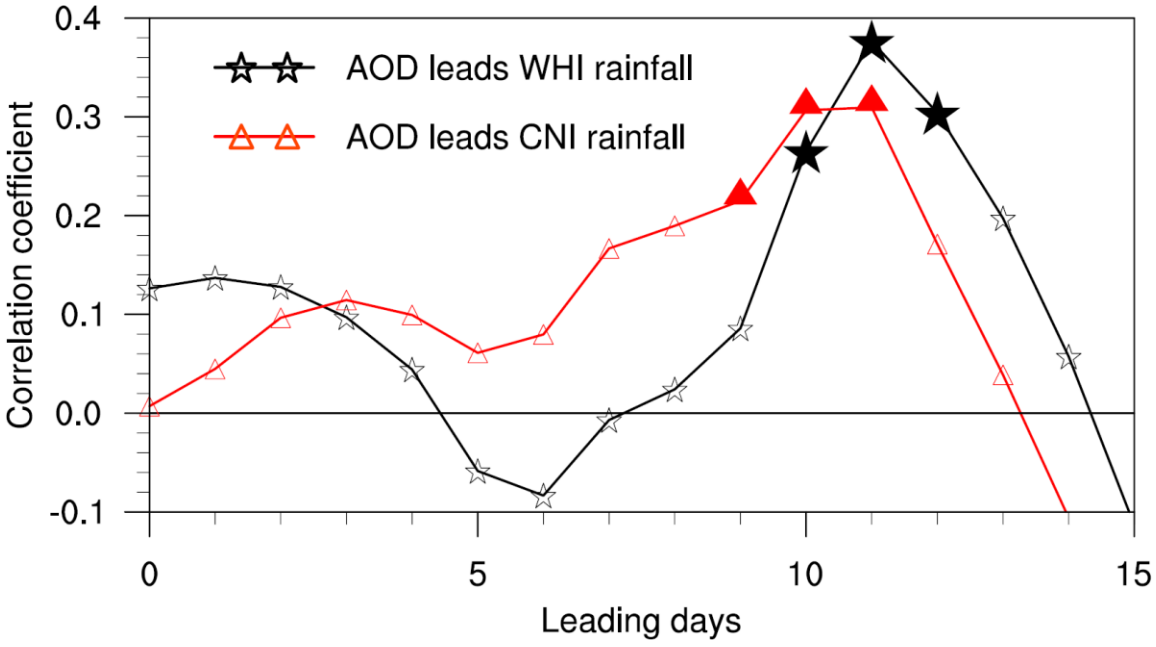

Figure 3.10. Cross-correlation coefficients between WRF-Chem simulated rainfall in WHI and CNI and AOD in remote DST region. All correlations are calculated based upon daily anomalies obtained by subtracting the 21-day running mean from the daily data. The filled markers represent that the correlation coefficients are 95% confident based on the *t*-test. The unfilled markers are not significant.

3.8. Physical Mechanism of AOD–ISM Relationship

3.8.1. Radiative Forcing of Dust

The direct radiative forcing of dust at all-sky conditions is calculated at the top of the atmosphere (TOA), in the atmosphere, and at the surface. Because the spatial patterns of clear-sky radiative forcing are similar to all-sky conditions, we focus only on all-sky conditions. Figure 3.11 shows the ensemble mean of dust radiative forcing (ALLF minus NDST) for SW, LW, and net (SW+LW) radiation. For SW, dust aerosols at the TOA reflect and scatter more SW radiation back to space than dust-free cases, so the SW radiative forcing is negative as shown in Figure 3.11a (downward is defined as positive). The

negative SW radiative forcing is very strong over water bodies, such as the Red Sea, the AS, the Persian Gulf, and the Caspian Sea, with a magnitude around 30 W m^{-2}. However, Figure 3.11a shows a quite weak or even positive SW radiative forcing over regions with bright surfaces, such as in eastern North Africa, the AP, the IP, and the Taklimakan Desert. The contrasting spatial patterns of SW radiative forcing over water and land are due to the high surface albedo contrast between them. Due to the high albedo of dust layers, when dust plumes reach the ocean, they reflect and scatter more SW radiation back to space than water bodies. Note that the small and sparsely distributed positive SW radiative forcing at the TOA is due to changes in clouds, which can be caused by dust-induced changes in atmosphere dynamics and cloud microphysics. In the atmosphere, dust aerosols can absorb SW radiation and heat the atmosphere. Figure 3.11b shows positive SW radiative forcing over the entire domain. This positive radiative forcing can attain a magnitude of 20 to 25 W m^{-2} in Iraq, the southern AP, the northern AS, and Pakistan. The land–ocean contrast in radiative forcing observed at the TOA is not seen within the atmosphere, because the spatial distribution of dust-induced atmospheric heating is mainly determined by dust concentration rather than surface properties. However, some studies have proposed that dust aerosols can absorb SW radiation more effectively over bright surfaces than over dark surfaces due to multiple reflections of SW radiation between overlying dust layers and bright land surfaces (Lau et al., 2006; Kuhlmann and Quaas, 2010). At the surface, dust aerosols block SW radiation from reaching the surface through scattering and absorption, which results in a surface cooling effect as shown in Figure 3.11c. The maximum magnitude of the negative SW radiative forcing is about 30 W m^{-2} in the Red Sea, the southern AP, the northern AS, the Persian Gulf, and Pakistan.

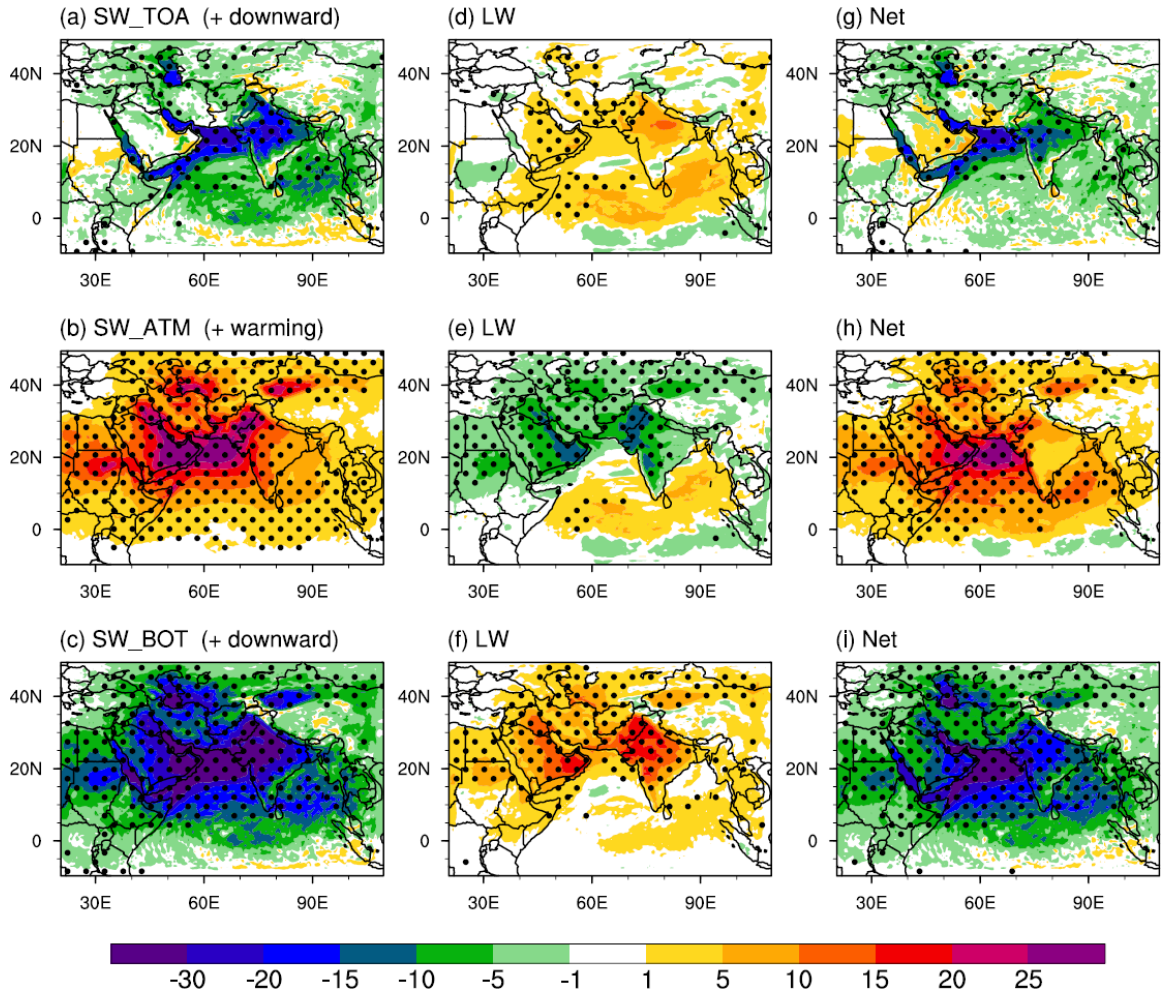

Figure 3.11. Spatial patterns of dust direct radiative forcing (W m^{-2}) at the top of the atmosphere (TOA), in the atmosphere (ATM), and at the surface (BOT) averaged during JJA 2008. Calculated from the ensemble mean differences between ALLF and NDST experiments of WRF-Chem. Downward radiation is defined as positive at the TOA and the surface; therefore, positive (negative) value means absorb/warming (irradiate/cooling) effects in the atmosphere. Net radiative forcing is the sum of SW and LW radiative forcing. The dotted areas mean that radiative forcing is 95% confident based on one-sided Student's *t*-test.

For LW, at the TOA Figure 3.11d shows that dust causes positive radiative forcing between 1 to 5 W m^{-2}. The dust layer can absorb surface-emitted LW radiation, and then

reemit it back to the surface. Because the dust layer is cooler than the surface due to its higher altitude, it emits less LW radiation to space than the surface on dust-free days, resulting in positive radiative forcing at the TOA. In the atmosphere, due to the blocking effect of dust, less LW radiation is absorbed by the atmosphere above the dust layer, which results in an atmospheric cooling effect. Figure 3.11e illustrates that the LW cooling effect of dust can reach magnitudes of 10 W m^{-2} in dust source regions and decreases to 5 W m^{-2} in most other regions except for the northern Indian Ocean and the Bay of Bengal, where positive forcing is observed. At the surface, the blocking effect of dust results in a positive forcing, i.e. warming effect, of about 10 W m^{-2} over the AP and Indian subcontinent as shown in Figure 3.11f. Note that the LW radiative forcing in the atmosphere and at the surface is stronger over land than over ocean. There are several reasons for this. First, the LW radiation interacts more efficiently with large particles than small particles. Large particles are mainly located in dust source regions and very few can be transported over long-distance to the ocean. Secondly, there is less water vapor between the surface and dust layer over land than over ocean. This strengthens the interactions between surface-emitted LW radiation and overlying dust aerosols. Third, the hotter land surface can emit more LW radiation than the cooler ocean surface.

It is obvious that the LW and SW radiative effects of dust have opposite signs, and the SW forcing has a much greater magnitude than LW forcing (Figures 3.11a─3.11f). Therefore, the dust net radiative forcing is dominated by the SW forcing (Figures 3.11g─3.11i). The area-averaged radiative forcing of dust over the whole domain is summarized in Table 3.4. By simple comparison of values in Table 3.4, we can conclude that a quarter to one-third of the SW radiative forcing is counterbalanced by LW radiative effects, which is consistent with previous studies (Huang et al., 2009).

Table 3.4. Area-averaged direct radiative forcing of dust simulated by WRF-Chem over the entire model domain for JJA 2008. The acronyms have the same meaning as in Figure 3.11. Units: W m^{-2}.

	SW	LW	Net
TOA	–3.32	1.07	–2.25
ATM	6.44	–1.64	4.80
BOT	9.76	2.71	–7.05

3.8.2. Dust Impact on Circulation

Dust aerosols can change large-scale circulations through their surface cooling effects and atmospheric warming effects. The resultant circulation change depends on the net effect of the two.

Figure 3.12a illustrates the spatial pattern of the ensemble mean thickness differences in ALLF and NDST simulations between 800 hPa and 500 hPa averaged for JJA 2008. According to the hypsometric equation, the thickness between two isobaric surfaces is proportional to the mean temperature of the layer. Figure 3.12a illustrates the increased thickness over the AS and southeast AP with a magnitude of 25 to 30 m, equal to 2.5 to 3 K. The spatial pattern of the thickness differences generally follows the AOD spatial pattern (Figure 3.3e). Figure 3.12b shows the vertical profiles of area-averaged atmospheric heating sources at all-sky conditions in DST. LW radiative forcing and sensible heating contribute to the atmospheric cooling from the surface to about 600 hPa. The SW radiative forcing is the only source of atmospheric warming effect, which is strongest near 950 hPa and diminishes to zero near 400 hPa. The latent heat shows little changes. Net atmospheric heating, which is the sum of LW, SW, sensible heat, and latent heat, demonstrates the atmospheric heating effect of dust from the near surface to 400 hPa except for an anomalous cooling effect at 900 hPa, which is caused by cloud effects.

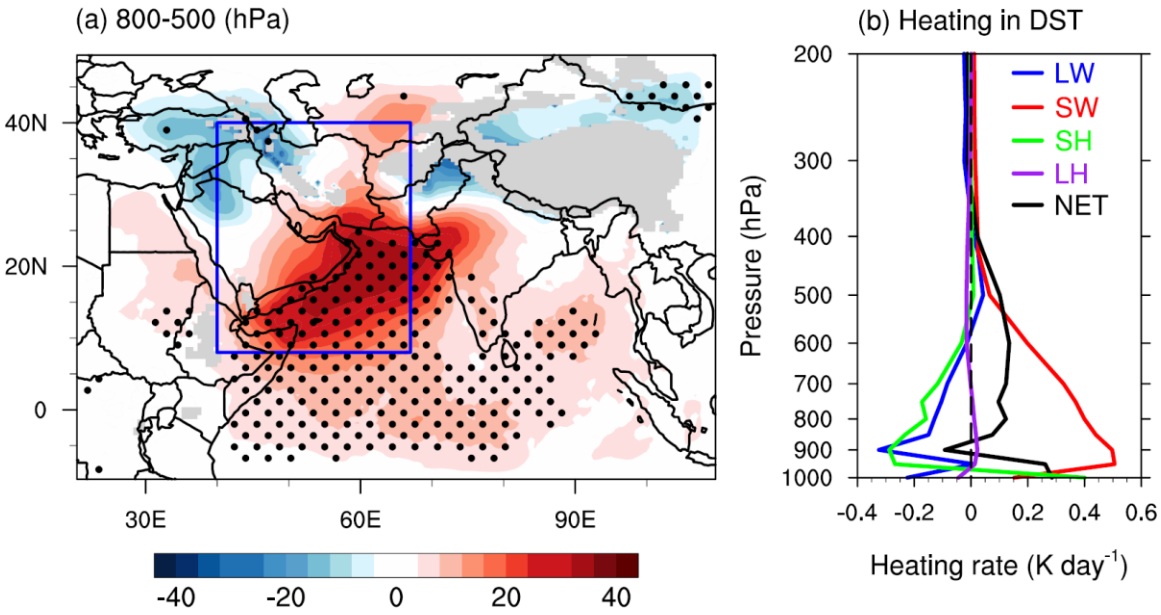

Figure 3.12. (a) Spatial pattern of WRF-Chem ensemble mean differences in thickness between 800 and 500 hPa pressure layers between the ALLF and NDST experiments (unit: m). (b) Vertical profiles of the WRF-Chem ensemble mean differences in atmospheric heating rate area-averaged in DST (box in (a)) between the ALLF and NDST experiments (units: K day^{-1}). The dotted areas in (a) mean that radiative forcing is 95% confident based on one-sided Student's *t*-test. All heating rates are for all-sky conditions. "SH", "LH", and "NET" stand for sensible heating, latent heating, and net heating rate. Net heating is the sum of SW, LW, SH, and LH.

Due to dust-induced atmospheric heating in the lower troposphere, a low-pressure system at 850 hPa can be observed (shown as contours in Figure 3.13a) over the AS, Shamal wind regions, the IP, and the Caspian Sea and nearby regions. Associated with the low-pressure system is a convergence region centered over the north AS and western India at 850 hPa, illustrated by arrows in Figure 3.13a. In this convergence area, the strengthened southwesterly winds transport more water vapor from the AS northeastward to the Indian subcontinent. When moist airflows meet the mountains in CSWI, CNI, Tibetan Plateau, and north Pakistan, they are lifted, converged and cooled, which forms the orographic

rainfall (Figure 3.6). Additionally, the strengthened northwesterly winds over the AP can result in more dust emission over the AP and transport them from the AP to the AS, thus forming a positive feedback. Figure 3.13b shows that dust can also modulate the atmospheric circulation in the upper troposphere, e.g. 500 hPa. There are two dust-induced convergence regions at 500 hPa: the IP and Iraq, CNI and North China. The role of dust-induced upper troposphere heating and circulation changes in modulating ISM is not clear and needs to be addressed in future studies. Dai et al. (2013) showed that the south-north thermal contrast in the mid-upper troposphere is more important for the Asian monsoon than that in the lower troposphere.

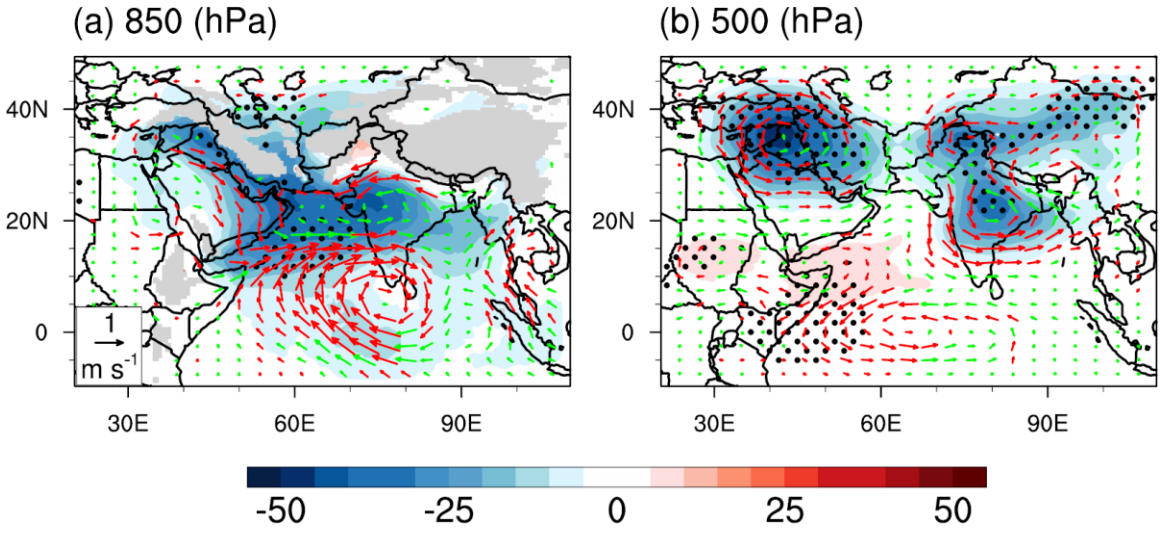

Figure 3.13. WRF-Chem ensemble mean differences in GPH (shading; unit: m) and winds (arrows; units: m s^{-1}) at (a) 850 hPa and (b) 500 hPa between ALLF and NDST experiments. The dotted areas are 95% confident based on one-sided Student's *t*-test. The red arrows show wind differences that are 95% confident based on one-sided Student's *t*-test, and green arrows are other wind differences (not confident).

3.8.3. Dust Impact on Moisture Budget

By disturbing large-scale circulations, dust can also modulate the moisture budget of ISM. Contours in Figure 3.14 show the spatial distribution of the ensemble mean of precipitable water differences in the entire atmospheric column in ALLF and NDST experiments during JJA 2008. Increased PW is simulated over the entire Indian subcontinent with maximum increases of 2 mm in CSWI and IGP. The increased PW is attributed to the strengthened moisture transport by southwesterly winds over the AS and southeasterly winds over the IGP, as indicated by arrows in Figure 3.14. A minor PW increase occurs in east India around 20° N, which causes decreased rainfall in this area as shown in Figure 3.6. Note that the increased PW is less than that of the increased rainfall in CSWI and central India. This is because rainfall process usually involves moisture convergence, which brings in moisture from surrounding regions (Trenberth, 1999).

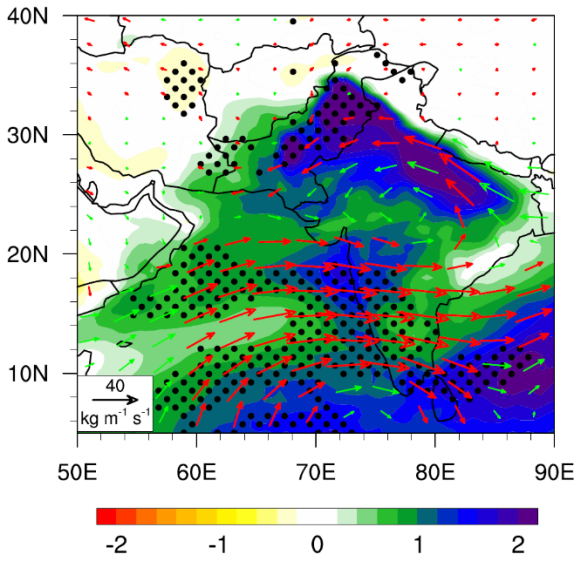

Figure 3.14. Same as Figure 3.6, but for precipitable water (shading; unit: mm) and water vapor flux (arrows; units: kg m^{-1} s^{-1}) both integrated within the entire atmospheric column. Black dots represent precipitable water differences that are 95% confident based on a one-sided Student's *t*-test. The red arrows represent wind differences that are 95% confident, and the green arrows represent other wind differences (not confident).

3.9. DISCUSSION AND CONCLUSIONS

Frequent dust storms develop in the boreal summer due to the strong "Shamal" winds in the AP and IP. After a long-distance transport, these dust storms can reach the AS and interact with ISM. Using observational datasets, we found a positive correlation between the ISM rainfall and the remote Middle East dust aerosols. To disclose the physical mechanism responsible for this correlation, a regional meteorological model with online chemistry, WRF-Chem, is used to examine the radiative effects of Middle East dust on ISM. The primary conclusions are drawn below.

WRF-Chem is capable of simulating the major ISM features and heavy dust loading in the Middle East and the AS during the boreal summer. The model can capture the ISM circulations quite well, e.g. the cross-equator circulation and the southwesterly winds over the AS. It also reproduces precipitation patterns quite similar to observations, with heavy precipitation located in CSWI and IGP. The low bias of precipitation in central India is partly attributed to the lack of representation of agriculture irrigation. In addition, by tuning the empirical proportionality constant in the GOCART dust emission scheme against satellite observations, the model can capture the main spatiotemporal features of dust aerosols in the Middle East and its surrounding regions.

Satellite retrievals show that AOD in DST is positively correlated with the ISM rainfall in CSWI, CNI, and Pakistan. This correlation is examined here by using WRF-Chem. Two groups of experiments with the presence and absence of dust emission are designed to isolate dust impacts on ISM rainfall. Ensemble model results based on PPCE show that mineral dust increases the ISM rainfall by 0.44 mm day^{-1} (about 10%) in WHI. The spatial pattern of the modeled rainfall increase is highly consistent with the observational results shown in J2014 and this study. However, V2014 and S2015 show different patterns. Using a GCM, V2014 demonstrated significantly decreased rainfall or

very weakly increased rainfall in central India. The differences in rainfall response between their studies and ours may be attributed to different atmospheric heating patterns caused by dust (Figure 3.12 in this study versus Fig. S4a in V2014), which may result from different representations of dust emission, dust diffusion in the PBL, or model resolution. An accurate representation of elevated orography of the Tibetan Plateau is critical in simulating ISM due to the large elevation gradient (Bollasina et al., 2011). Using an RCM, S2015 showed results that were opposite to those of J2014 and this study in terms of rainfall response. In S2015, the decreased rainfall in CNI is attributed to high GPH anomalies over CNI, Pakistan, the central and north AS. Our further analyses show that the modeled rainfall response from the ensemble mean shows a much stronger spatial correlation with the observed rainfall response than any of the ensemble members, indicating that ensemble mean can cancel out and reduce model errors from various parameterizations. By comparing the performance of individual ensemble member in Figures 3.7 and 8, we conclude that the largest effects on our simulation results are from the PBL schemes, followed by the SW radiation schemes, and the aerosol chemical mixing rules have a relatively weak effect.

Cross-correlation analysis of modeled daily AOD in DST and the ISM rainfall in WHI and CNI shows a maximum cross-correlation when AOD leads rainfall by 11 days (Figure 3.10). This finding is very similar to the 13 days found in observational datasets by J2014. Note that the model experiments here have separated the rainfall response due to dust for the correlation analysis, while observations include various forcing and responses. Considering that a typical dust event usually lasts 3 to 5 days, and the time for water vapor to be transported from the equator to CNI is about a week assuming a wind speed of 10 m s^{-1}, the total time is about 10 to 12 days. Therefore, the timescale of 11 days is reasonable.

This cross-correlation provides further evidence to support the causal relationship between Middle East dust and ISM rainfall.

Dust-induced ISM rainfall increase can be explained by the dynamic impacts of dust radiative forcing on water vapor transport from the AS to the ISM region. By absorbing solar radiation in the atmosphere (Figure 3.11h), dust heats the lower troposphere (800–500 hPa) by about 2 to 2.5 K over the AS, the south AP, and the IP (Figure 3.12). The dust-induced atmospheric heating causes a low-pressure system at 850 hPa over the AS and surrounding regions, which is associated with a convergence anomaly over the AS and north India (Figure 3.13). The southwestern branch of the convergence anomaly transports more water vapor from the AS to the Indian subcontinent, resulting in more precipitable water in the atmospheric column (Figure 3.14). This strengthened southwesterly wind due to dust-induced heating is responsible for the dust-ISM rainfall correlation observed in both satellite data and model simulations. Furthermore, the northwestern branch of the convergence anomaly over the AP can create more dust emission and transport these dust particles from the AP to the AS, building a positive feedback.

Two issues warrant further discussion. First, SST is prescribed during the three-month simulation period. The SST in the AS has been shown to play an important role in modulating the ISM rainfall (e.g. Levine and Turner, 2012). The surface cooling effect of dust can decrease the SST, which may influence the ISM rainfall response to Middle East dust. Secondly, although the aerosol indirect effect is turned on in this study, experiments with a relatively coarse horizontal resolution of 54 km cannot resolve convective clouds (typically 1–5 km wide), which in turn fails to consider the indirect aerosol effects on the ISM rainfall. In future studies, we suggest to use a high resolution RCM with grid spacing at 1–5 km coupled with an ocean model to quantify the impacts of dust-induced SST

change and aerosol indirect effect on the ISM rainfall. Overall, this study highlights the dynamic impact of remote mineral dust in the Middle East on ISM rainfall. This dust-ISM rainfall relationship should be examined in the models participating in the fifth and future phases of the Coupled Model Intercomparison Project on interannual to decadal timescales.

Chapter 4: Contribution of Local and Remote Dust and Anthropogenic Aerosols to Indian Summer Monsoon Rainfall

4.1. ABSTRACT

The intraseasonal responses of the Indian summer monsoon (ISM) rainfall to local anthropogenic aerosols in India and dust aerosols in both local (i.e. the Thar Desert) and remote (i.e. the Middle East and west China) regions are studied using the Weather Research and Forecasting model with chemistry (WRF-Chem). Ensemble experiments are designed by perturbing the model physical and chemical schemes to examine the model uncertainties. Model results show that the dust-induced ISM rainfall increase can be mainly attributed to the remote dust aerosols in the Middle East, while the contributions from local dust aerosols in India and Pakistan and remote dust aerosols in West China are rather limited. Both the convective and stratiform rainfalls increase due to the presence of dust and anthropogenic aerosols. Convective rainfall shows a more spatially consistent increase than stratiform rainfall, whose increase follows the topography. Moreover, the rainfall increase induced by the local anthropogenic aerosols is comparable to that by the Middle East dust aerosols. Rainfall increases due to the Middle East dust aerosols are mainly located in North India, Central India, and Costal South West India, while the anthropogenic aerosol-induced rainfall increases are located in North India and Central India. The different spatial distributions of rainfall changes can be attributed to different responses of water vapor flux to dust and anthropogenic aerosols. The Middle East dust aerosols tend to enhance the southwesterly monsoon flow over the Arabian Sea, which can transport more water vapor to both South India and North India, while the anthropogenic aerosols tend to enhance the southeasterly monsoon flow over North India, which results in more water vapor in this region. Our findings highlight the different intraseasonal responses of the ISM rainfall to dust aerosols in different regions and anthropogenic aerosols, which may have

implications for the ISM predictions and attribution of the ISM rainfall variability on longer timescales.

4.2. INTRODUCTION

Unlike greenhouse gases, which are well-mixed in the atmosphere and tend to be evenly distributed around the globe, aerosols concentrate near their source regions and tend to have great temporal variabilities due to their short residence time in the atmosphere (i.e. days to months). Therefore, the climate effects of aerosols are quite evident in the regional scale and on the short time scales.

Asia has the world's heaviest aerosol loading due to desert dust and anthropogenic emissions. Dust storms are quite active in the Middle East (.e.g. the Arabian Desert), South Asia (e.g. the Thar Desert), and East Asia (e.g. the Takalimakan Desert and Gobi Desert) during the boreal spring and summer. Anthropogenic emissions in South Asia and East Asia contribute significantly to the total aerosol loading and have increased dramatically since 1950s resulting from rapid increase in population and energy consumption. Increasing evidence from observational and modeling studies show that both natural dust and anthropogenic aerosols in Asia can affect one of the world's largest monsoon system the—Indian summer monsoon (ISM)) on various time scales.

There are three physical pathways underlying the aerosol–ISM connection. The first pathway is related to the "solar dimming" effect (Ramanathan et al., 2005; Meehl et al., 2008; Bollasina et al., 2011, 2013; Bollasina et al., 2014). The aerosol-induced surface cooling effect in the Indian subcontinent can reduce the south–north ocean–land thermal contrast, which results in the weakened ISM on decadal timescales. This effect can be caused by both scattering aerosols (e.g. sulfate and sea salt) and absorbing aerosols (e.g. mineral dust and black carbon). The second pathway is related to the "elevated heat pump"

(EHP) effect (Lau et al., 2006). The dust aerosols from the Taklimakan Desert and black carbon from India can stack up around the Tibetan Plateau and heat the atmosphere in the mid-upper troposphere, which can result in an anomalous low-pressure system over the Tibetan Plateau and strengthen the ISM on inter-annual timescales. It is worth pointing out that the EHP effect is a subject of debate mainly due to lack of observational support (Lau and Kim, 2006; Kuhlmann and Quaas, 2010; Nigam and Bollasina, 2010; Lau and Kim, 2011; Nigam and Bollasina, 2011). The third pathway is also related to the EHP effect, but over the Iranian Plateau instead of the Tibetan Plateau. The dust aerosols over the Iranian Plateau and the Arabian Sea transported from the Arabian Desert can contribute to an enhanced southwesterly monsoon flow over the Arabian Sea due to the dust-induced heating in the lower-mid troposphere, which increases the ISM rainfall on weekly to intraseasonal timescales (Jin et al., 2014; Vinoj et al., 2014).

The above studies have not differentiated the impacts from local versus remote aerosols in Asia on the ISM system. Given the large spatial extent of the ISM and multiple aerosol source regions in the ISM and the surrounding regions, it is important to quantify how aerosols from different sources and different regions modulate the ISM system through the physical pathways.

Our study uses ensemble modeling experiments to examine the radiative, dynamic, and hydrological responses of the ISM system to direct and indirect effects of dust versus anthropogenic aerosols in different regions in Asia on the intraseasonal timescales. One of our objectives is to quantify the relative contributions of dust aerosols from India and remote regions in the Middle East and East Asia to changes in the ISM rainfall. We also study the role of the local anthropogenic emissions in the ISM rainfall response. Finally,

we examine the EHP effect in our model simulations, aiming to shed further light on this debate from a modeling perspective.

4.3. Model and Dataset

4.3.1. Model

We use the Weather Research and Forecasting model coupled with the online chemistry (WRF-Chem) developed collaboratively among the community (Grell et al., 2005; Fast et al., 2006; Barnard et al., 2010). WRF-Chem simultaneously simulates the emission, turbulent mixing, transport, transformation, dry and wet depositions of trace gas and aerosols and their interactions with meteorological fields. The Modal Aerosol Dynamics Model for Europe (MADE) primary aerosols scheme coupling the Secondary Organic Aerosol Model (SORGAM) scheme is used, which considers eight primary aerosol types (i.e. sulfate, nitrate, ammonium, black carbon, mineral dust, sea salt, organic carbon, and water) and several secondary organic aerosols formed by transformation from biogenic and anthropogenic emissions. The Goddard Chemistry Aerosol Radiation and Transport (GOCART) dust emission is employed to generate dust emission in the model. The dust emission calculated by GOCART is determined mainly by surface winds and soil erodibility, as shown in Figure 4.1a.

The model domain covers the Middle East and the ISM region centered over the Arabian Sea with 160×120 points in the zonal and meridional directions, respectively, with a horizontal resolution of 54 km and 30 vertical layers up to 50 hPa. This domain includes four major deserts, i.e. the Arabian Desert, the Thar Desert, the Takalimakan Desert, and the Gobi Desert, along with some other deserts in the Iranian Plateau, Afghanistan, and Turkistan. All simulations span a 104-day period from 20 May 2008 to 31 August 2008. The analyses focus on simulation results for only JJA 2008 with the first 12 days as "spin

up". The model boundary and initial conditions are extracted from the European Centre for Medium-Range Weather Forecasts (ECMWF) Interim Reanalysis (ERA-I) global reanalysis dataset. For detailed model configuration, please see Chapter 3.

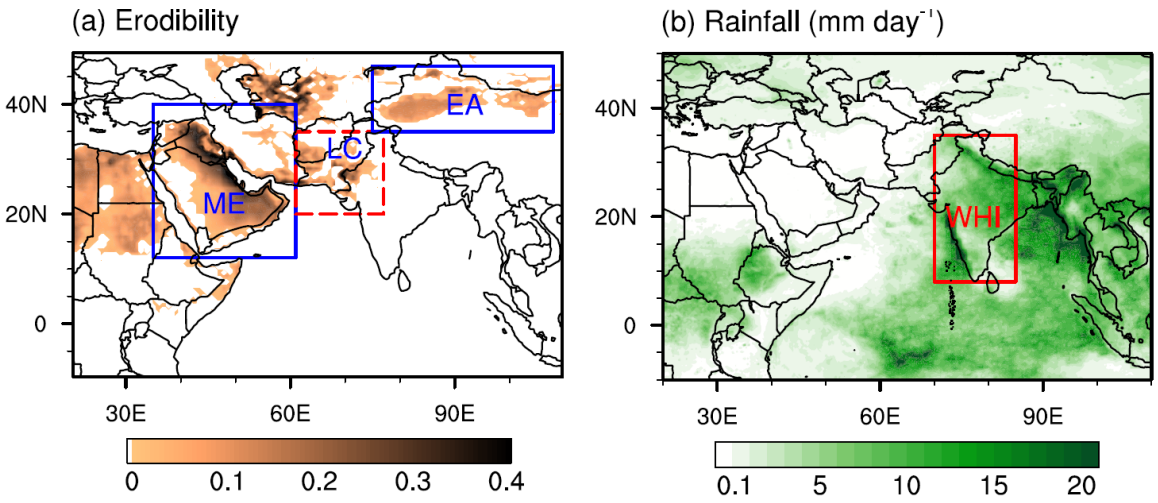

Figure 4.1. (a) Soil erodibility (unitless) map used in WRF-Chem GOCART dust emission scheme. "LC", "ME", and "EA" represent the local dust source regions (20°–35° N, 61°–77° E), the remote dust source regions in the Middle East (12°–40° N, 35°–61° E), East Asia (35°–47° N, 75°–108° E), respectively. (b) Averaged rainfall (mm day^{-1}) for JJA 2008.

4.3.2. Aerosol Indirect Effects

Aerosols can form cloud condensation nuclei (CCN) after being activated and then influence the concentration and size of cloud droplets, cloud albedo, liquid water content in cloud, cloud fraction, and cloud lifetime. WRF-Chem 3.5 parameterizes the aerosol indirect effects as

$$\frac{\partial N_k}{\partial t} = -(V \cdot \nabla N)_k + D_k - C_k - E_k + S_k \quad (4.1)$$

where N_k is grid cell mean cloud droplet number mixing ratio in layer k, D_k is vertical diffusion, C_k is droplet loss due to collision or coalescence or collection, E_k is droplet loss due to cloud evaporation, and S_k is droplet source due to nucleation.

Aerosol activation, a process in which aerosol particles form cloud droplets, is the only source of cloud droplet number in Equation (4.1). Not all aerosol particles can form cloud droplets. Aerosol particles that are not activated to form cloud droplet will remain suspend in the interstitial air and referred as interstitial aerosols. Aerosol activation is based on a maximum supersaturation. When cloud dissipates, cloud droplets evaporate and cloud-borne aerosols are resuspended, i.e. aerosols transform from cloud-born to interstitial states.

The effective cloud particle size is calculated based on cloud droplet number and cloud water mixing ratio in the Goddard and RRTMG SW radiation schemes (first indirect effect). The aerosol-induced changes in cloud droplets mass and number are treated in the two-moment Lin et al. and Morrison microphysics scheme (second direct effect). It is should be pointed out that these processes are only applied in the grid cell so that they may not have much impact on sub-grid processes, such as convection. The total rainfall calculated by WRF-Chem consists of the stratiform and convective rainfall. As mentioned above, only stratiform rainfall (i.e. grid cell rainfall) is affected by aerosol indirect effects.

4.3.3. Experimental Design

We have conducted one reference and six disturbed experiments, with sea surface temperature described from ERA-I. The reference experiment (REF) considers all aerosol forcing (i.e. mineral dust, anthropogenic emission, sea salt, biogenic emission, and biomass burning). The disturbed experiments are otherwise identical to REF, except for exclusion of dust emission in the whole domain (NWH), the Middle East (NME), local regions (NLC), East Asia (NEA), and exclusion of anthropogenic emission in the whole domain (NAN), to determine the roles of different types of regional aerosols and to examine the

nonlinear relationship between aerosol forcing and the ISM response. The detailed description of the seven experiments are listed in Table 4.1.

Table 4.1. Summary of experiment design.

Experiments	Description
REF	All aerosol simulations
NWH	No dust emission in the entire domain
NME	No dust emission in the Middle East
NLC	No dust emission in the local areas
NWC	No dust emission in East Asia
NAN	No anthropogenic emission in the entire domain

To understand the influence of the model uncertainties on our results, 16 additional ensemble simulations are carried out in each of the 7 experiments. The 16 ensemble simulations are created using the various physical and chemical parameterizations of 1) aerosol chemical mixing rules (4), 2) aerosol turbulent mixing in the boundary layer (2), and 3) shortwave radiation schemes (2). For the detailed explanation of the ensemble simulations, see Chapter 3.

4.3.4. Datasets

The aerosol optical depth (AOD) datasets are from the Moderate-resolution Imaging Spectroradiometer (MODIS) onboard the National Aeronautics and Space Administration (NASA) Aqua satellite and the Multi-angle Imaging Spectroradiometer (MISR) onboard NASA Terra satellite. Both MODIS and MISR level three monthly datasets are used for model evaluation. In addition, the Monitoring Atmospheric Composition and Climate (MACC) aerosol reanalysis dataset is compared for consistency with satellite datasets.

4.4. RESULTS

4.4.1. AOD in Simulations

Figure 4.2 shows AOD at 550 nm for observations, reanalysis, and module simulations for JJA in 2008. Observational AOD from satellites and MACC reanalysis illustrate high AOD values over the Arabian Sea, the Arabian Peninsula, Pakistan, north India, with a magnitude of about one, as shown in Figures 4.2a–4.2d. The simulated AOD in REF demonstrates similar spatial patterns to the observational AOD, but with underestimates over the Arabian Sea and overestimates over the Arabian Peninsula. The potential contributors to AOD bias are discussed in Chapter 3. Figure 4.2f displays AOD from anthropogenic emissions, with the highest AOD values in north India high values in the Arabian Peninsula, and low values over the ocean regions and the Tibetan Plateau. The AOD spatial patterns in experiments NME, NLC, and NWC are as expected with low values in areas where dust emissions are removed, as shown in Figures 4.2g–4.2i, respectively. Note that AOD values in Pakistan and north India for NME are lower than those in REF due to eastward transport of dust from the Arabian Peninsula. Figure 4.2j illustrates AOD in NAN, with high AOD values in dust source and downwind regions.

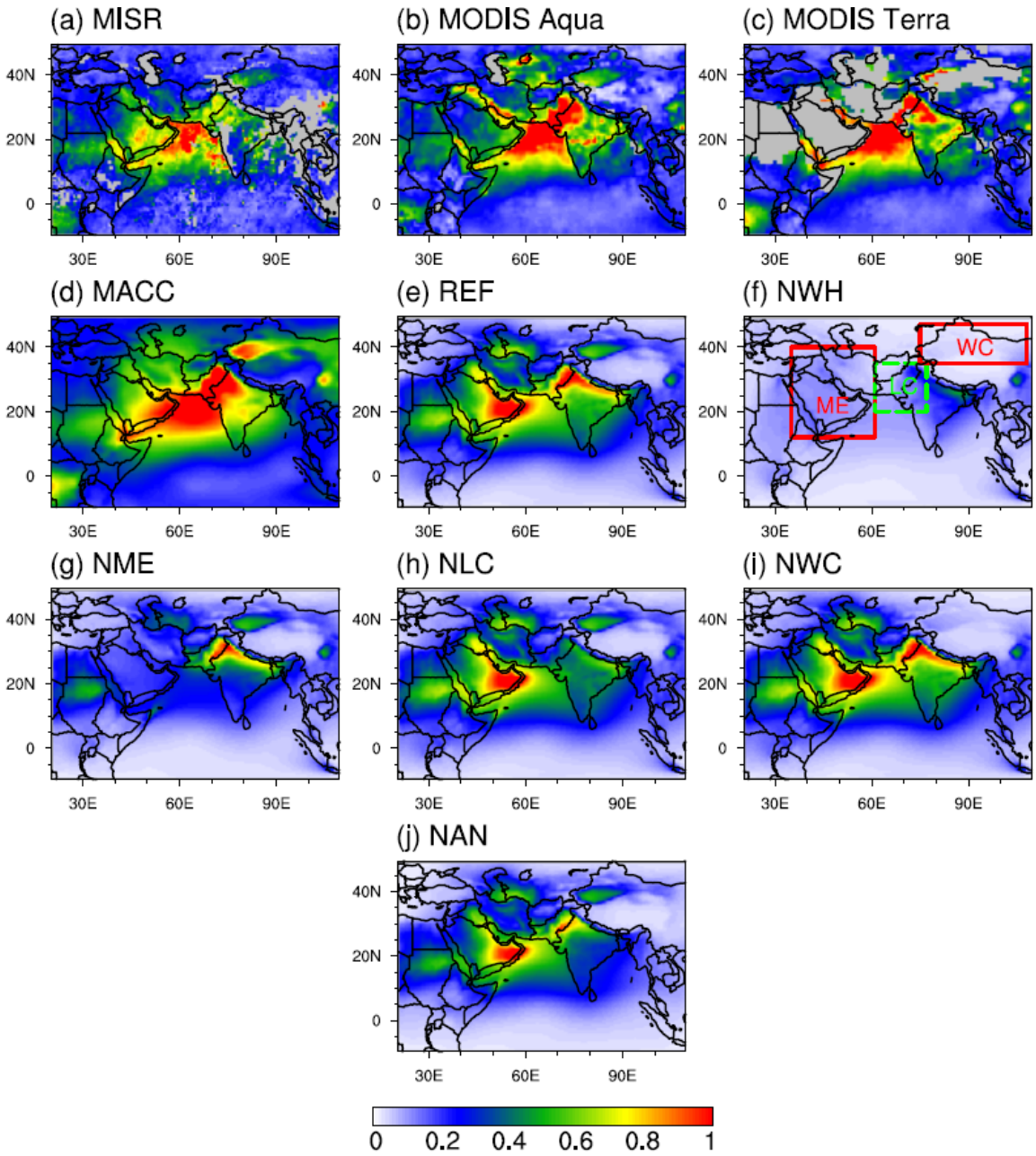

Figure 4.2. Spatial pattern of AOD from (a) MISR, (b) MODIS Aqua, (c) MODIS Terra, (d) MACC, (e) REF, (f) NWH, (g NME, (h) NLC, (i) NEA, (j) NAN, and (k) NHP averaged for JJA 2008. MISR AOD is measured at 558 nm, and all other AOD is shown at 550 nm. WRF-Chem AOD is the ensemble mean of 16 ensemble members in each experiment. Missing values are masked in grey in Figures 4.2a–4.2c.

Figure 4.3 illustrates the AOD difference between REF and other experiments. The spatial pattern of AOD in each experiment is responsible for changes in meteorological fields and is to be discussed later.

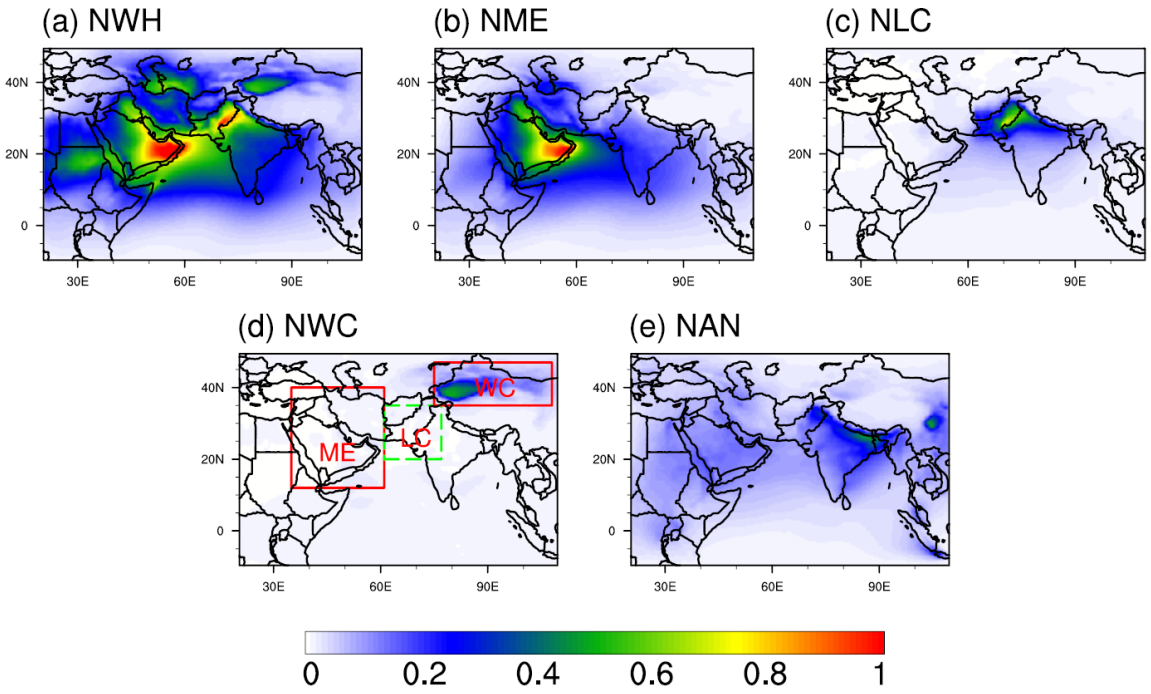

Figure 4.3. Spatial patterns of ensemble mean of WRF-Chem simulated dust AOD in (a) NWH (REF–NWH), (b) NME (REF–NME), (c) NLC (REF–NLC), and (d) NEA (REF–NEA) averaged for JJA 2008.

4.4.2. Rainfall Responses to Dust and Anthropogenic Aerosols

Figure 4.4 illustrates the ensemble means of total rainfall (i.e. the sum of convective and stratiform rainfall; units: mm day^{-1}) responses to dust and anthropogenic aerosols averaged for JJA 2008. Figure 4.4a shows that the ISM rainfall increases in north Pakistan, north and central India, Coastal South West India (CSWI), and Coastal South East India (CSEI) due to dust aerosols in the entire study domain (REF–NWH). The area-averaged rainfall response in WHI region (Figure 4.1b) is 0.44 mm day^{-1}, about 10% of total rainfall. Figure 4.4b demonstrates the rainfall response to Middle East dust aerosols (REF–NME).

The spatial patterns of rainfall response in Figure 4.4b are quite similar to those in Figure 4.4a in the Indian subcontinent, but with a smaller magnitude and fewer significant areas. The area-averaged rainfall response in WHI is 0.34 mm day^{-1} in NME, accounting for 77% of rainfall response in NWH. The rainfall response to dust aerosols in local areas (i.e. the Thar Desert; REF–NLC) is not significant, as shown in Figure 4.4c. Similarly, the rainfall response to West China dust aerosols (REF–NWC) in Figure 4.4d is significant but in rather limited areas in central India. Figure 4.4e indicates that the rainfall increases in north Pakistan, and central and north India, with quite weak decreases in south India due to anthropogenic aerosols (REF–NAN). The area-averaged rainfall increase is 0.31 mm day^{-1} in NAN. Note that the total rainfall responses to dust and anthropogenic aerosols generally follow the topography with rainfall increases in CSWI, central and north India, and mountain regions in Pakistan.

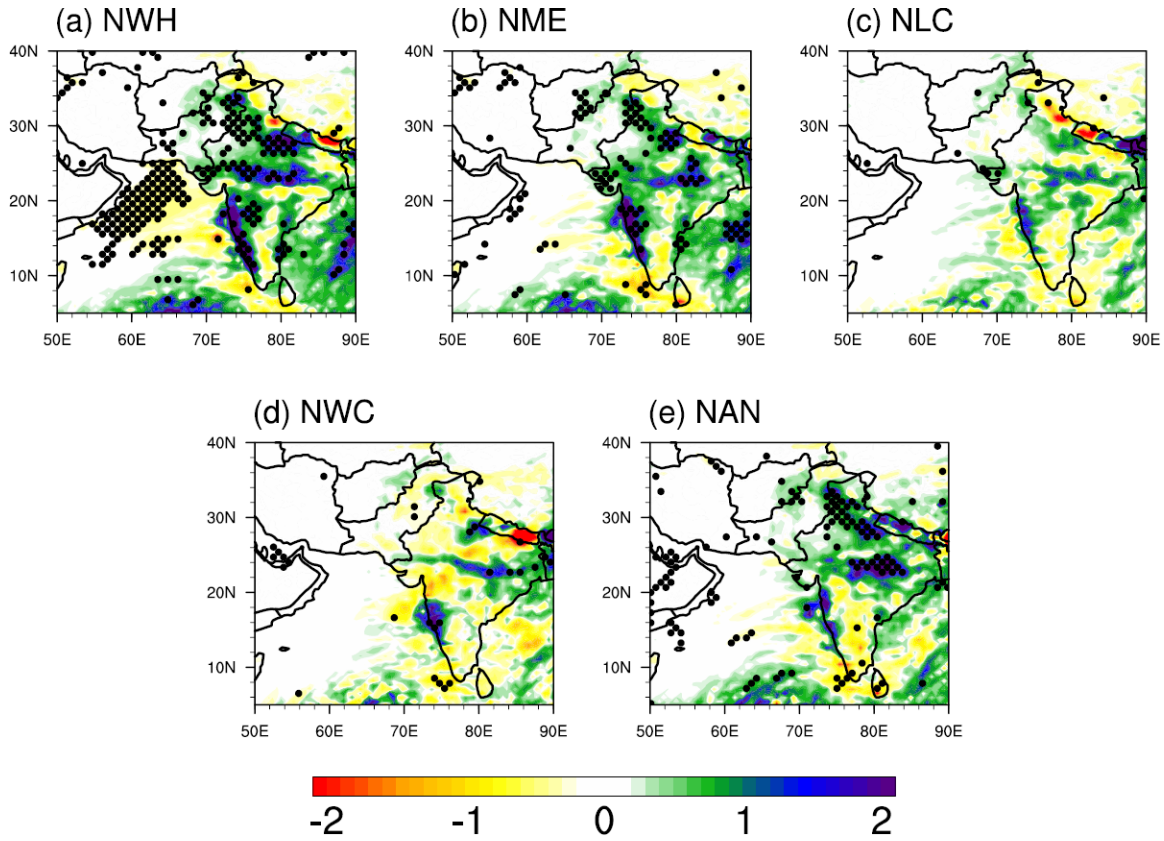

Figure 4.4. The ensemble mean of total rainfall response (mm day^{-1}) due to dust emission in (a) the whole model main, (b) the Middle East, (c) the local areas, and (d) the East Asia averaged for JJA 2008. The dotted areas are confident at 90% level based on a one-sided Student's *t*-test.

Figure 4.5 shows the convective rainfall responses calculated by model convection scheme. Figure 4.5a demonstrates that convective rainfall increases significantly in Pakistan and the entire India except south India due to dust aerosols in the entire domain, with an area-averaged value of 0.32 mm day^{-1}, which accounts for 73% of the total rainfall response. The rainfall responses to Middle East dust is quite similar to those in NWH, but with more significant areas in south India and less significant areas in north India compared to those in NWH. The Middle East dust aerosols-induced rainfall increase is about 0.24 mm day^{-1}, contributing about 75% to the convective rainfall increase in NWH. The dust

aerosols in local and remote West China do not show significant impacts on the ISM convective rainfall, as shown in Figures 4.5c and 5d. Due to anthropogenic aerosols, the rainfall increases in north Pakistan and north India with a magnitude of 0.20 mm day^{-1}. Note that the convective rainfall responses are much more spatially consistent than the total rainfall responses.

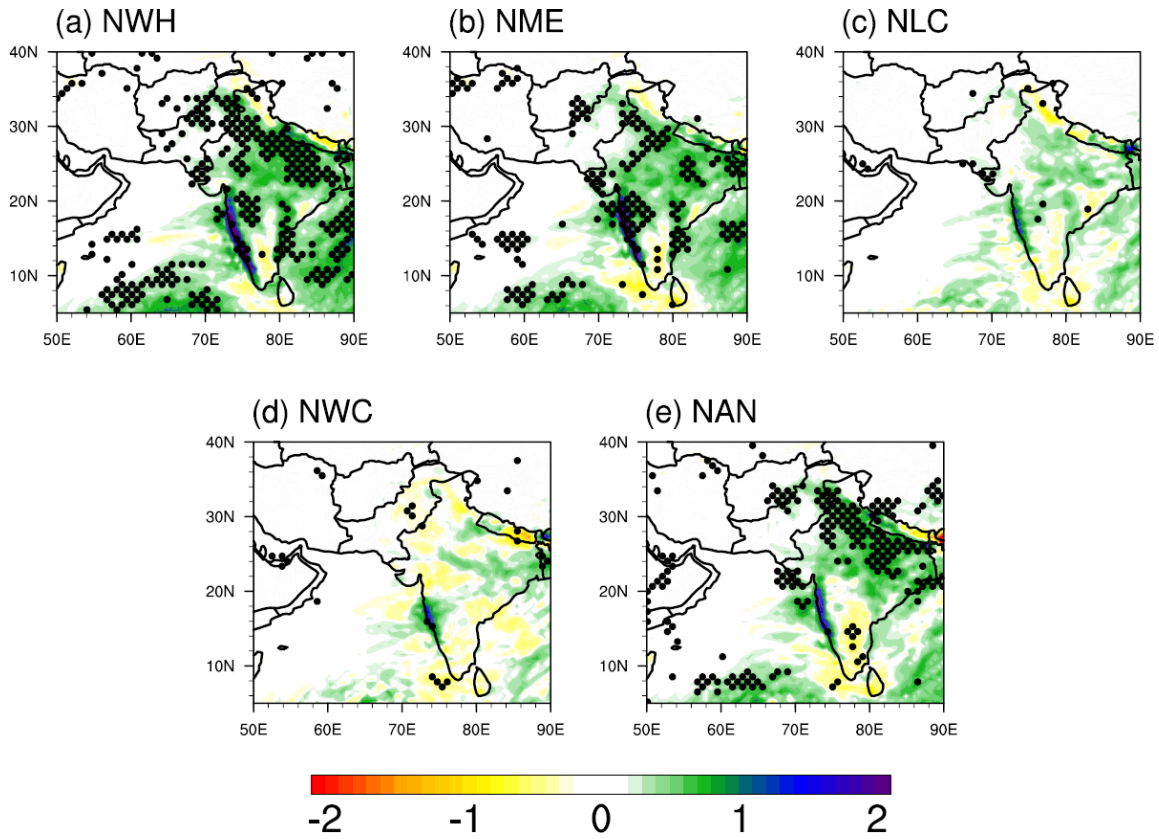

Figure 4.5. The same as Figure 4.4, but for the convective rainfall response (mm day^{-1}).

Figure 4.6 shows similar spatial patterns of the stratiform rainfall responses to the total rainfall responses, but with a smaller magnitude and much fewer significant areas in all experiments. The stratiform rainfall increases by 0.12 mm day^{-1}, contributing 27% of the total rainfall response in NWH experiments. Middle East dust aerosols-induced

stratiform rainfall has a magnitude of 0.10 mm day^{-1}, accounting for 83% of total stratiform rainfall responses. Local dust aerosols show little impacts on stratiform rainfall (Figure 4.6c), but remote dust aerosols in West China cause increased rainfall in some areas of central India in Figure 4.6d. The anthropogenic aerosols causes rainfall increases in central and north India, with a magnitude of 0.11 mm day^{-1}. One interesting phenomena are the significant stratiform rainfall decrease over the Arabian Sea in Figure 4.6a, which is also shown Figure 4.4a.

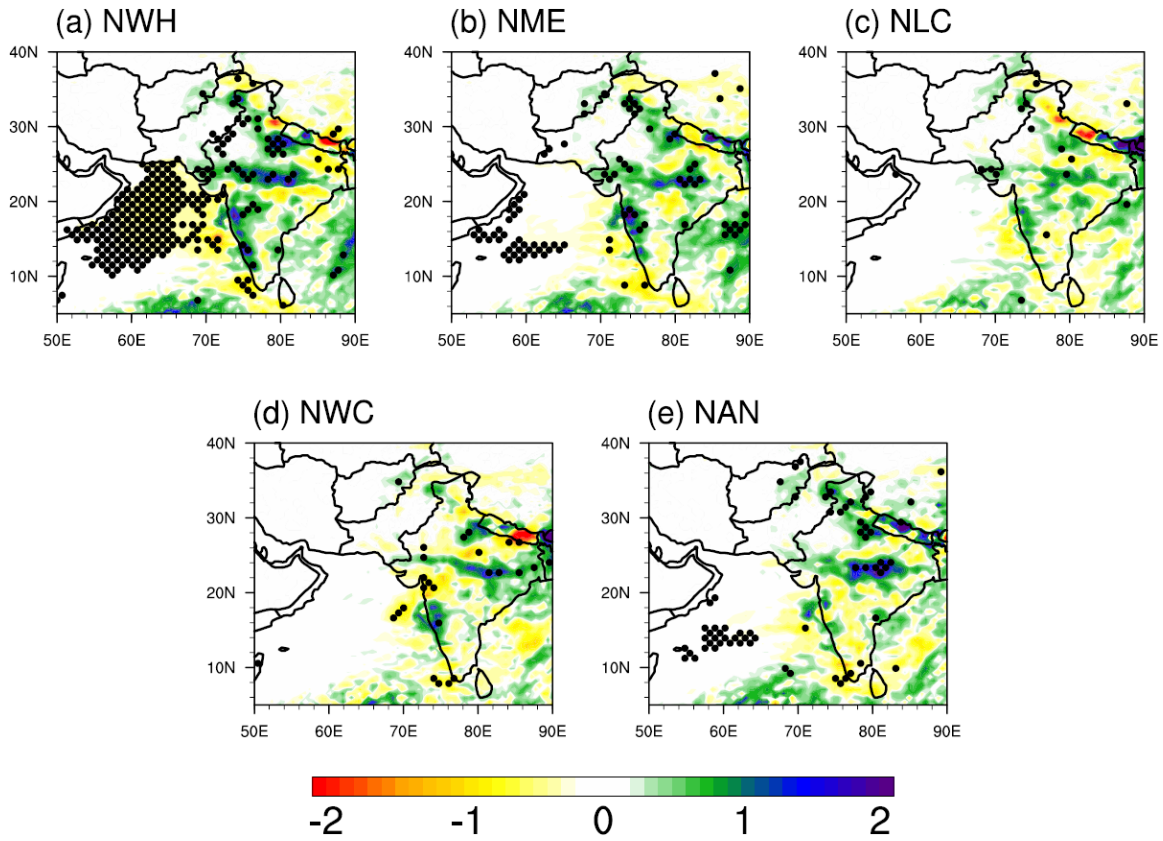

Figure 4.6. The same as Figure 4.4, but for the stratiform rainfall response (mm day^{-1}).

The area-averaged rainfall responses over WHI region in all experiments are summarized in Table 4.2. The convective rainfall responses contribute to about two thirds

of total rainfall responses in all experiments except for NLC and NWC, which is reasonable, because during monsoon season deep convections are quite strong and frequent. On the other hand, the stratiform rainfall responses determine the spatial distribution of total rainfall responses, which follows the topography. Furthermore, remote Middle East dust aerosols dominate the total rainfall responses to dust aerosols in the entire domain, while local dust aerosols show little impacts and remote dust aerosols in West China display limited impacts on the ISM rainfall. Although the anthropogenic aerosols have lower concentrations than dust aerosols, they play a role as important as Middle East dust aerosols in modulating the ISM rainfall due to their stronger absorbing ability of solar radiation.

Table 4.2. Area-averaged rainfall responses (mm day^{-1}) and their percentage in the rainfall responses due to dust aerosols in the entire domain (mm day^{-1}) for JJA 2008.

Experiments	Total		Convective		Stratiform	
	Rainfall	%	Rainfall	%	Rainfall	%
NWH	0.44		0.32	72.7	0.12	27.3
NME	0.34	77.3	0.24	74.9	0.10	83.3
NLC	0.04	9.7	0.05	17.1	–0.01	–8.9
NEA	–0.01	–1.3	–0.001	–0.3	–0.005	–3.8
NAN	0.31		0.20	64.5	0.11	35.5

4.4.2. The Physical Pathways

4.4.2.1. Aerosol Indirect Effects

Figure 4.4a shows that rainfall decreases over the central and western Arabian Sea, which are attributed to the stratiform rainfall response, as shown in Figure 4.6a. We talked about the topography-following patterns of the stratiform rainfall responses in Indian

subcontinent in section 4.1, which cannot be applied over the Arabian Sea. Therefore, the stratiform rainfall response decreases over the Arabian Sea have nothing to do with large-scale circulation changes. One potential contributor is the aerosol indirect effects. Figure 4.7 shows the ensemble means of responses of the flux of cloud droplet number to dust and anthropogenic aerosols averaged over JJA 2008. Significant increases in cloud droplet number due dust aerosols (REF–NWH) are seen over the Arabian Sea, India, and Bay of Bengal, as shown in Figure 4.7a. Dust-induced increases in cloud droplet number can result in smaller cloud droplets when cloud liquid water does not show a significant increase, which can prevent or postpone rainfall, thereby causing the rainfall decrease in the Arabian Sea. The aerosol indirect effects on rainfall generally depend on the concentrations of activated aerosol particles and the liquid water supply in clouds. When aerosol concentration is high or there is a limited liquid water supply in clouds, aerosol indirect effects tend to decrease the rainfall (Albrecht, 1989; Gong and Barrie, 2003). This is the reason that rainfall decreases are mainly located over the Arabian Sea rather than other regions where the activated aerosols particles are limited. Figures 4.7b and 4.7e show quite limited activated aerosol particles, therefore no significant rainfall decreases are seen in Figures 4.6b and 4.6e. Note that although dust AOD in NME is much higher than anthropogenic aerosol AOD (Figures 4.3b and 4.3e), the increases of cloud droplet numbers due to dust in NME are much weaker than anthropogenic aerosols, which is attributed to the different hygroscopic properties of dust (~0.1) and anthropogenic aerosols (~0.5).

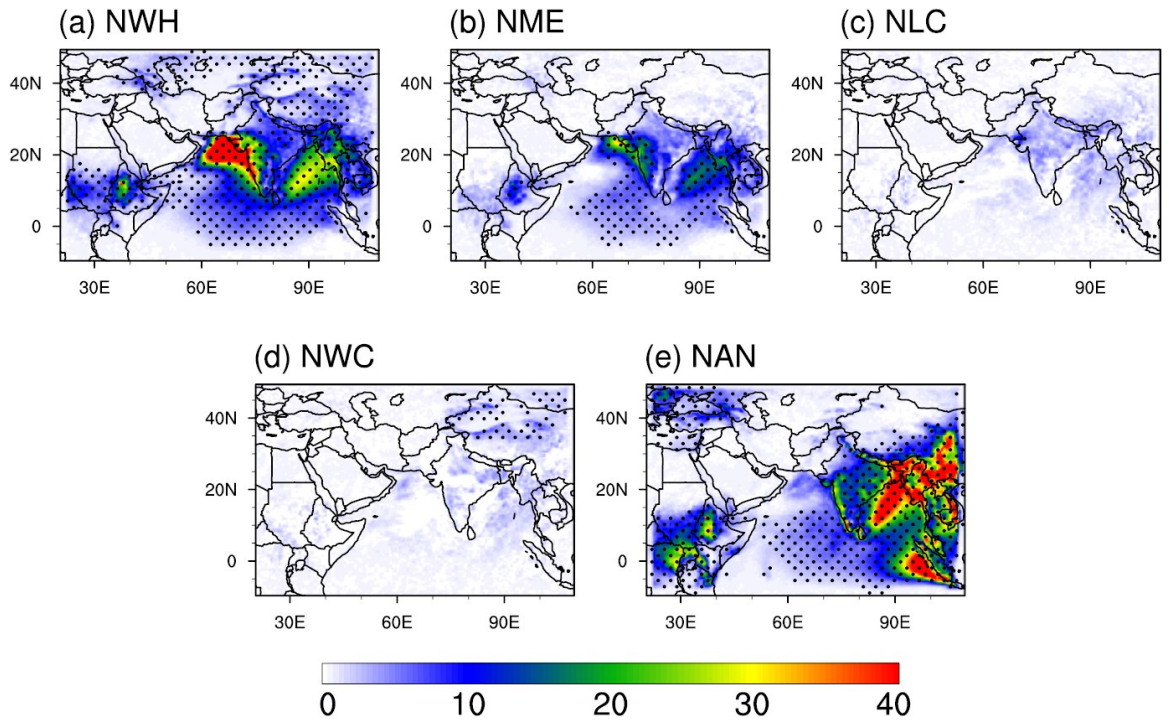

Figure 4.7. The ensemble mean of cloud droplet number flux (1.0×10^{9} m^{-2}) due to dust emission in (a) the whole model main, (b) the Middle East, (c) the local areas, (d) west China, and (e) anthropogenic aerosols averaged for JJA 2008. The dotted areas are confident at 95% level based on a one-sided Student's *t*-test.

4.4.2.2. Aerosol Radiative Effects

Figure 4.8 demonstrates the ensemble means of net radiative forcing (i.e. the sum of SW and LW radiation at the surface in all-sky conditions due to dust and anthropogenic aerosols averaged for JJA 2008. Downward is defined as positive, which means the surface gets energy and becomes warmer. Figure 4.8a shows a negative radiative forcing in the entire domain except for some sparse and small areas with positive radiative forcing without confidence. The strongest negative radiative forcing is located in the Arabian Sea, the Persian Gulf and the Caspian Sea, followed by the Red Sea, the Arabian Peninsula, and west India. The area-averaged radiative forcing is about –7.05 W m^{-2} as shown in Table 4.3. The radiative forcing induced by Middle East dust aerosols shows similar spatial

patterns to those in NWH but with a smaller magnitude and fewer significant areas as shown in Figure 4.8b. The area-averaged value is –3.48 W m^{-2}, accounting for about half of radiative forcing in NWH. Note that the surface negative radiative forcing is stronger over ocean than over land in Figures 4.8a and 4.8b, even though dust aerosols have higher concentrations over land than over ocean, which is due to much lower surface albedo of the ocean (~0.08) than the land (~0.4). Therefore, the spatial distributions of aerosol-induced surface cooling effect is largely influenced by the land–ocean distribution. Figures 4.8c and 4.8d show negative radiative forcing in Pakistan and West China due to the local dust aerosols, with area-averaged magnitudes of 0.76 and 0.41 W m^{-2}, respectively. The anthropogenic aerosols induced negative radiative forcing is strongest in the source regions, i.e. north India, with an area-averaged magnitude of 4.34 W m^{-2}, which is stronger than the radiative forcing due to dust aerosols in Middle East, local regions, and west China, but much smaller than that due to dust aerosols in the entire domain.

Table 4.3. Area-averaged radiative forcing (W m^{-2}) in all-sky conditions for JJA 2008.

Experiments	**BOT**		**ATM**		**TOA**	
NWH	–7.05		4.80		–2.25	
NME	–3.48	49.4	2.29	47.7	–1.19	52.9
NLC	–0.76	10.8	0.40	8.3	–0.36	16.0
NEA	–0.41	5.8	0.15	3.1	–0.26	11.6
NAN	–4.34		3.94		–0.41	

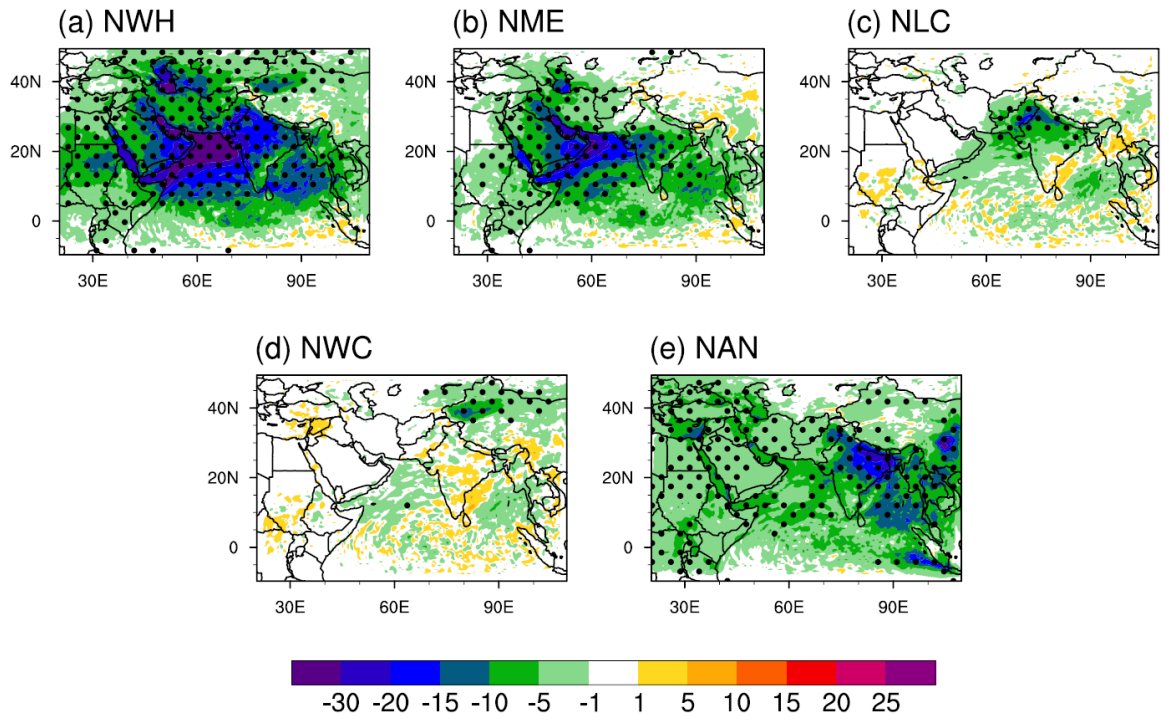

Figure 4.8. Spatial patterns of net radiative forcing (W m^{-2}) at the surface in all-sky conditions averaged during JJA 2008 in (a) NWH, (b) NME, (c) NLC, (d) NEA, (e) NAN, and (f) NHP. Calculated from the ensemble mean differences between REF and disturbed experiments of WRF-Chem. Downward radiation is defined as positive at the surface; therefore, positive (negative) value means absorb/warming (irradiate/cooling) effects. Net radiative forcing is the sum of SW and LW radiative forcing. The dotted areas mean that radiative forcing is 95% confident based on one-sided Student's *t*-test.

Figure 4.9 show the net radiative forcing in the atmosphere. Here positive means absorbing of solar radiation by the atmosphere. The spatial patterns in Figure 4.9 are quite similar to those in Figure 4.8. However, the spatial patterns of radiative forcing in the atmosphere do not show land–ocean contrast (Figures 4.9a and 4.9b) as for surface radiative forcing (Figures 4.8a and 4.8b). This is because that the aerosol concentrations dominate the radiative forcing in the atmosphere. The radiative forcing at the top of the atmosphere is shown in Figure 4.10, showing a quite strong land–ocean contrast due to

surface albedo. Note that the anthropogenic aerosols cause stronger and more areas of warming at the top of the atmosphere in Figure 4.10e than dust aerosols in Figures 4.10a and 4.10b due to their much stronger absorbing ability of solar radiation than dust aerosols.

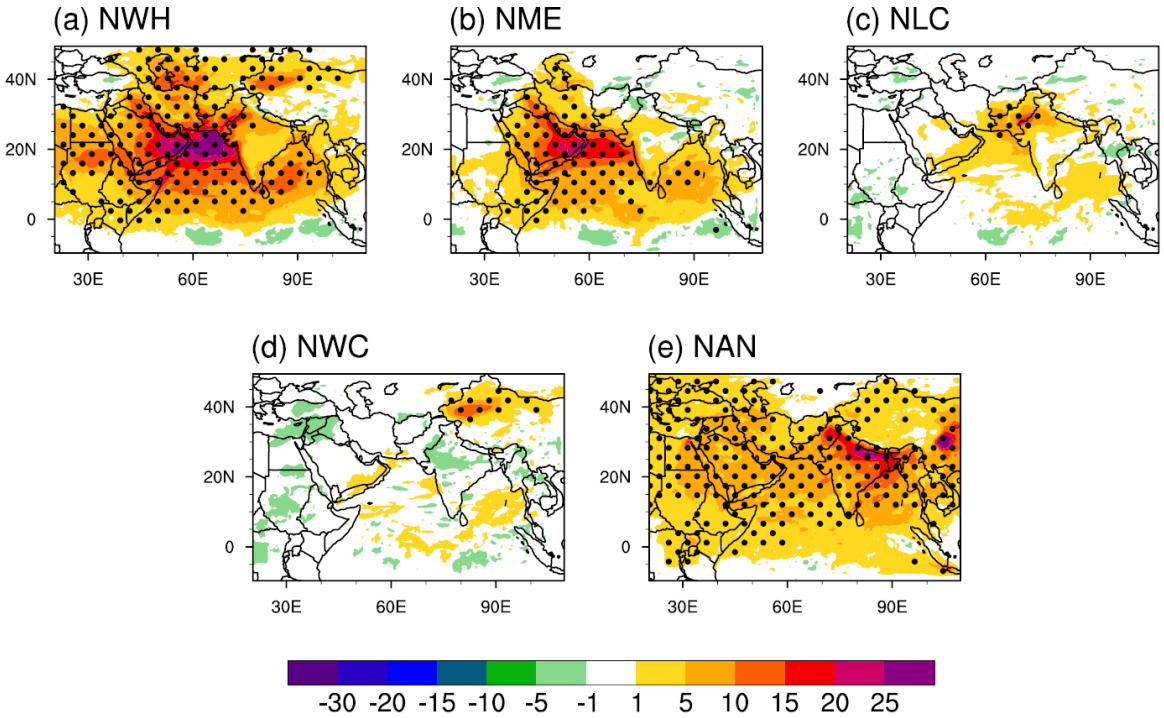

Figure 4.9. Same as Figure 4.8, but for net radiative forcing (W m^{-2}) in the atmosphere.

The area-averaged radiative forcing is summarized in Table 4.3. First, by comparing radiative forcing in the atmosphere and at the surface and top of atmosphere due to dust aerosols in various source regions, we can see that Middle East dust aerosols play a dominant role in altering the radiative forcing induced by dust aerosols in the entire domain, contributing half of the radiative forcing. If we add the radiative forcing induced by dust aerosols in the Middle East, local regions and west China, we find that their sums account for only 59% to 80% of radiative forcing due to total dust aerosols. One of the potential reasons is the positive feedbacks between dust emissions and the local "Shamal" winds proposed by Jin et al. (2014, 2015), which will also be discussed later. Also note that

anthropogenic aerosols-induced negative radiative forcing accounts for much a smaller percentage of that by the total dust aerosols at the surface (61.6%) and the top of the atmosphere (18.2%) than in the atmosphere (82.1%).

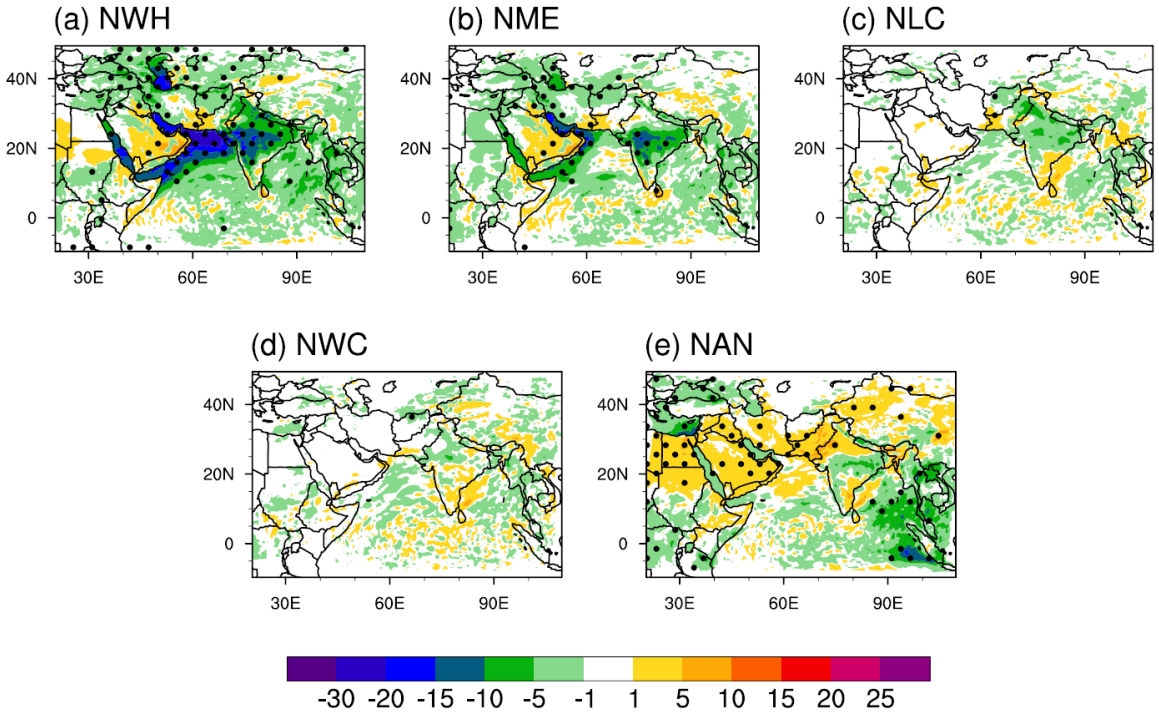

Figure 4.10. Same as Figure 4.8, but for net radiative forcing (W m^{-2}) at the top of the atmosphere.

4.2.2.3. Impact on Monsoon Dynamics

Figure 4.11 shows the ensemble means of responses of geopotential height (shading; unit: m) and wind (arrows; units: m s^{-1}) both at 850 hPa to dust and anthropogenic aerosols averaged for JJA 2008. Figure 4.11a shows a low pressure system centered over the Arabian Sea, the Persian Gulf, Iraq, Turkmenistan, and west India due to the total dust aerosols, which is associated with an anomalous convergence zone centered over the Arabian Sea and west India. The spatial patterns of responses of geopotential height and winds, as shown in Figure 4.11b, are akin to those due to total dust aerosols, but with a

smaller magnitude. The dust aerosols in local regions and west China show little impacts on monsoon dynamics, as shown in Figures 4.11c and 4.11d. The anthropogenic aerosols-induced circulation changes are weak in south India but strong in north India, as shown in Figure 4.11e.

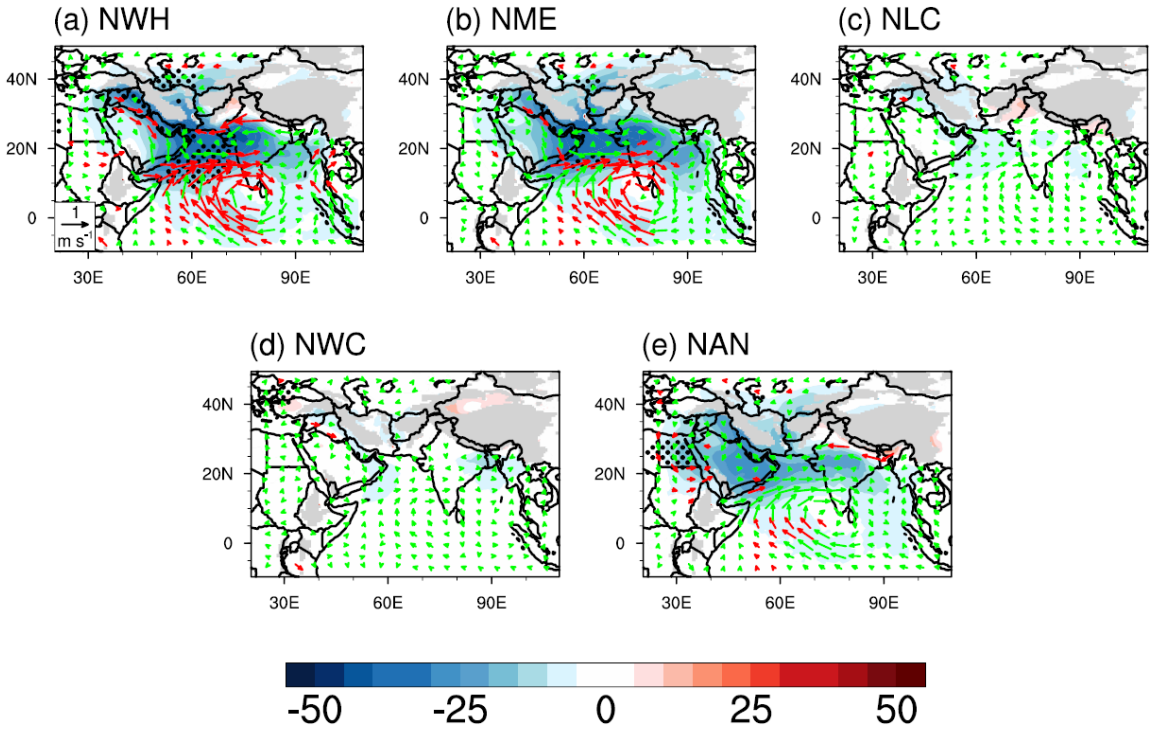

Figure 4.11. WRF-Chem ensemble mean differences in geopotential height (shading; unit: m) at and winds (arrows; units: m s^{-1}) both at 850 hPa between REF and disturbed experiments. The dotted areas are 95% confident based on one-sided Student's t-test. The red arrows show wind differences that are 95% confident based on one-sided Student's t-test, and green arrows are other wind differences (not confident). Grey color means missing data due to interpolation.

4.2.2.4. Impact on Water Vapor Budget

Figure 4.12 shows the ensemble means of responses of precipitable water (shading; unit: mm) and water vapor flux (arrows; units: kg m^{-1} s^{-1}) due to dust and anthropogenic aerosols averaged for JJA 2008. Figure 4.12a demonstrates that the precipitable water

increases in the entire India due to the total dust aerosols, with the strongest increases in the entire Pakistan and south and north India. The precipitable water increases are caused by more water vapor transported by the enhanced southwesterly and southeasterly monsoon flows over the Arabian Sea and north India, respectively. In Figure 4.12b, the precipitable water increases only in some regions of south India due to Middle East dust aerosols. The dust aerosols in local areas and west China show little impacts on water vapor budget (Figures 4.12c and 4.12d). The anthropogenic aerosols induced precipitable water increases are mainly located in Pakistan and north India due to the enhanced water vapor transport in these regions. Note that although the dust aerosols in local areas or remote dust aerosols in west China alone do not exhibit any significant impacts, they can play significant roles when taken into account with Middle East dust aerosols, which can be seen by comparing Figures 4.12a and 4.12b. This can be attributed to the aforementioned positive feedbacks between dust aerosols and the "Shamal" winds.

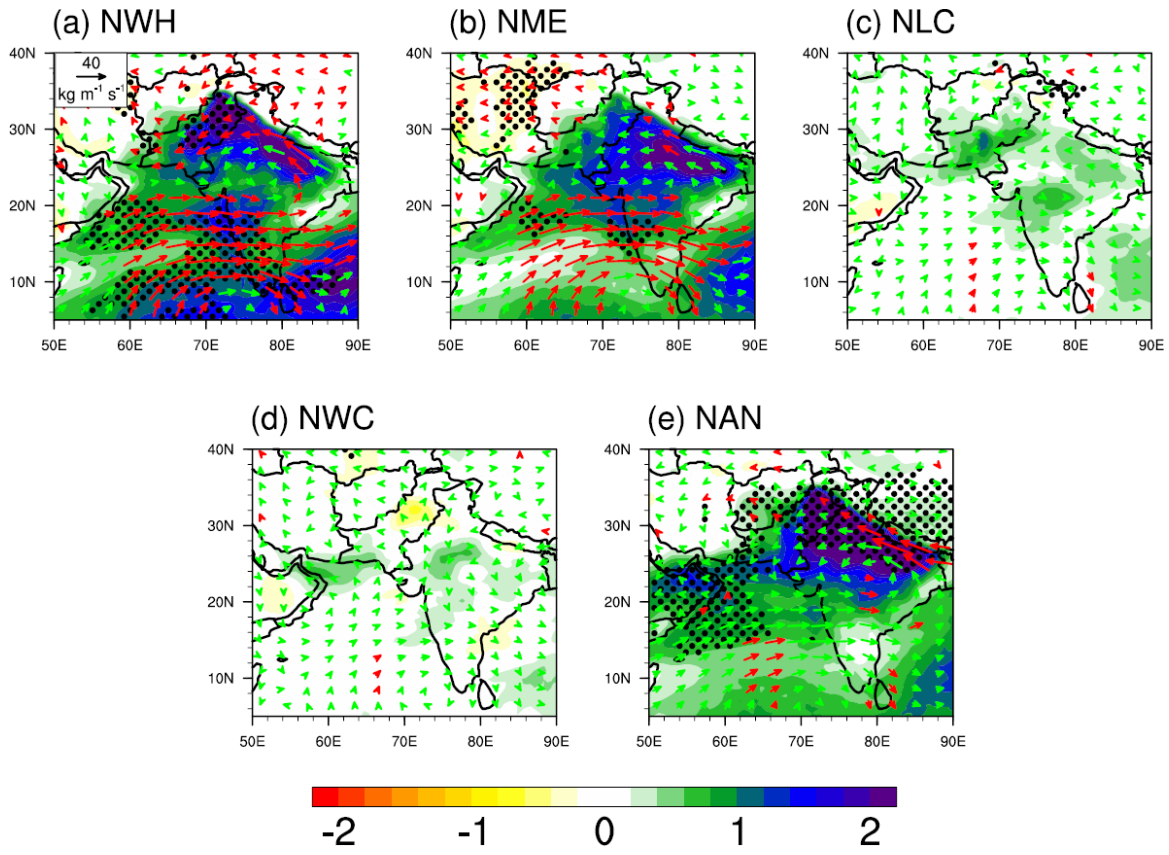

Figure 4.12. WRF-Chem ensemble mean differences in precipitable water (shading; unit: mm) and water vapor flux (arrows; units: kg m^{-1} s^{-1}) between REF and disturbed experiments. The dotted areas are 95% confident based on one-sided Student's t-test. The red arrows show water vapor flux differences that are 95% confident based on one-sided Student's t-test, and green arrows are other differences (not confident).

4.5. Discussion and Conclusions

The anthropogenic aerosols in India and dust aerosols in west China have been shown to have great impacts on the ISM rainfall. On the other hand, more frequent dust activities occur in the Middle East and India-Pakistan borders during the boreal summer. In this study, we examined the impacts of dust aerosols in various source regions on the ISM rainfall and compared the dust impacts with the anthropogenic aerosols impacts.

In our study domain, Middle East dust aerosols dominate the total aerosol concentrations, followed by anthropogenic aerosols and local dust aerosols in the Thar Desert, with the least contribution from dust aerosols in west China. The dust aerosols in the Arabian Peninsula and Iran can be transported southward by the northwesterly "Shamal" winds to the Arabian Sea and eastward by the southwesterly monsoon flow to India. The local and remote dust aerosols in west China are mainly suspended in the source regions with quite limited dust transported to the surrounding regions. The spatial patterns of anthropogenic aerosols are determined by their source locations since anthropogenic emissions do not depend on winds.

The dust induced rainfall increases are mainly located in north Pakistan, north and central India, and CSWI. The total dust induced rainfall increases are mainly (77%) attributed to Middle East dust aerosols. The anthropogenic aerosols can also cause rainfall increases, which are almost equal to the Middle East dust induced rainfall increases. Middle East dust aerosols tend to cause rainfall increases in both south and north India, while anthropogenic aerosols tend to cause rainfall increases in north India. Within the total rainfall increase due to dust aerosols, the convective rainfall response contributes 73% while the stratiform rainfall contributes the remaining 27%. Furthermore, both of the convective rainfall responses induced by dust and anthropogenic aerosols illustrate more spatially consistent patterns than the stratiform rainfall responses, whose spatial pattern follows the topography.

Both dust and anthropogenic aerosols induced monsoon rainfall responses can be largely attributed to their direct radiative effects. Middle East dust aerosols heat the atmosphere over the Arabian Sea, the Arabian Peninsula, and Iranian Plateau, which in turn results in a low-pressure system centered over the Arabian Sea. This low-pressure

system is associated with a convergence zone in the Arabian Sea, and the southwesterly flow transports more water vapor from the Arabian Sea to the Indian subcontinent, resulting in enhanced monsoon rainfall.

It should be pointed out that the lack of fully representing aerosol's indirect effects in our simulations may induce uncertainties to our conclusions. In the current WRF-Chem, aerosol's indirect effects are included only in the microphysics scheme at grid scales but not in the cumulus parameterization at sub-grid scales (Fast et al., 2006; Chapman et al., 2009). Therefore, the simulations at 54-km grid spacing cannot resolve convective clouds, nor can they fully consider aerosol's indirect effects. This problem becomes more important particularly for monsoon applications in which convective rainfall events are active and dominate the total rainfall. Increasing model resolution to resolve convective clouds can fully represent aerosol's indirect effects, but it will dramatically increase the simulation time and make simulations impossible on long timescales. We suggest including aerosol's indirect effects in cumulus parameterizations for simulations with horizontal resolutions larger than 10 km in the future model development.

Chapter 5: Summary and Future Work

5.1. SUMMARY

As one of the world's largest monsoon systems, the Indian Summer Monsoon (ISM) provides water resources to about one-third of the global population. While the impacts of anthropogenic aerosols on the ISM rainfall on decadal timescales have been extensively documented, very few studies have focused on the impacts of Middle East dust aerosols on the ISM rainfall. Focusing on the intraseasonal modulation of the ISM rainfall by Middle East dust aerosols, this dissertation has examined the underlying physical mechanism using multiple observational datasets and ensemble numerical simulations. The impacts of the local dust and anthropogenic aerosols in India and the remote dust aerosols in west China on the ISM rainfall are studied as well. The major conclusions are summarized as follows.

Chapter 2 addressed the first question: How does the ISM rainfall respond to the Middle East dust in observations on intraseasonal timescales? Based on MV-EOF of monthly anomalies of satellite AOD, atmospheric thickness between 700 and 500 hPa from reanalysis, winds at 850 hPa, and satellite rainfall for JJA during the period of 2000 and 2013. Spatial patterns of positive AOD anomalies over the Arabian Sea, the south Arabian Peninsula, and the Iranian Plateau are shown to be coupled with the positive ISM rainfall anomalies over Pakistan, central and north India, and CSWI. These coupled spatial patterns between AOD and rainfall are associated the enhanced water vapor transport from the Arabian Sea to the Indian subcontinent, which is caused by the strengthened southwesterly monsoon flow over the Arabian Sea, which itself is accompanied by the dust-induced atmospheric heating effect in the lower troposphere over the Arabian Sea and the surrounding regions. Furthermore, cross correlation analyses indicate the timescale between the coupled dust–monsoon is about 13 days. The results suggest that dust

concentrations over the Arabian Peninsula and the Arabian Sea form a positive feedback with the thermal low-pressure system centered over the Arabian Sea due to the dust-induced atmospheric heating.

Although the observations reveal a positive relationship between the Middle East dust and the ISM monsoon rainfall, no conclusions about the causal relationship can be drawn based on observations alone because multiple factors in observations contribute to the ISM rainfall variability. Numerical experiments were therefore designed in Chapter 3 to isolate the Middle East dust impacts from other factors on the ISM rainfall The objective was to answer the second question: Can the regional climate model reproduce the observed relationship between Middle East dust and the ISM rainfall, and what are the model uncertainties and how do they influence our results? Two groups of simulations with and without dust emissions were conducted using WRF-Chem for JJA 2008. Within each group, 16 ensemble simulations were created by using various physical and chemical scheme options to quantify the model uncertainties in parameterizing SW radiation, aerosol diffusion in the boundary layers, and aerosol chemical mixing rules. Model results show that the Middle East dust leads to an increased rainfall in Pakistan and India, which is consistent to observations. The modeled Middle East dust ant the IMS rainfall timescale is about 11 days, which is comparable to the observational timescale of 13 days. Analyses on ensemble members show that the biggest model uncertainty stems from the planetary boundary layer schemes and that SW radiation schemes are also a major source of uncertainty. Results show that the ensemble mean of the rainfall increases have a stronger spatial correlation with the regressed rainfall on AOD than any ensemble member in observations.

Chapter 4 further quantified the impacts of dust aerosols in various source regions on the ISM rainfall as well as compared dust impacts with local anthropogenic aerosol

impacts to answer the third question: How does the ISM system respond to different types of aerosols in different source regions on the intraseasonal timescales? Using the model ensemble method designed in Chapter 3, more simulations were conducted for various dust source regions, e.g. the Middle East and west China at regional scale, the Thar Desert at the local scale, and the anthropogenic aerosols in the entire domain. Model results show that the ISM rainfall responses to dust aerosols in the entire domain in JJA 2008 are largely (77%) attributed to Middle East dust aerosols, with little significant contributions from local and remote dust aerosols in the Thar Desert and west China, respectively. The remaining 23% of the ISM rainfall responses to dust aerosols in the entire domain comes from the non-linear response of the climate system, which is partly represented by the positive feedback between the enhanced northwesterly "Shamal" winds and the heat low pressure system centered over the Arabian Sea induced by positive dust radiative forcing in the lower troposphere. By decomposing total rainfall into stratiform and convective rainfall, model results show that the convective rainfall response contribute 73% of the total rainfall responses to dust. Moreover, aerosol indirect effects to some extent exhibit impacts on the rainfall over the western part of Arabian Sea, but no conclusions about aerosol indirect effects on the ISM rainfall can be drawn because aerosol indirect effects are not coupled into the cumulus scheme that dominates the monsoon total rainfall. Finally yet importantly, the anthropogenic aerosols, although with much lower concentration than natural dust in my study domain, can play a similar role in modulating the ISM rainfall in north India.

5.2. CAVEATS AND FUTURE WORK

As shown in previous chapters, this dissertation addresses the impacts of Middle East dust aerosols on the ISM rainfall on intraseasonal timescales and compares different

roles of natural dust with anthropogenic aerosols in modulating the ISM system. I hope my conclusions can be beneficial to the ISM rainfall prediction and reduce the casualties and property loss because of monsoon droughts and floods. However, some caveats in my studies are noted below and the future work is outlined as well.

5.2.1. Long-Term Trends of Middle East Dust and the ISM Rainfall

Previous studies have attributed the drying trend of the ISM rainfall to the increasing anthropogenic emissions during the second half of 20th century (Bollasina et al., 2011). However, this drying trend has been replaced by a wetting trend during the last decade, which is shown in Figure 5.1, while the local anthropogenic emissions continue to increase. The proposed intraseasonal positive response of the ISM rainfall to the Middle East dust in this work should be further examined on the decadal timescales, which may explain this observed drying–wetting transition.

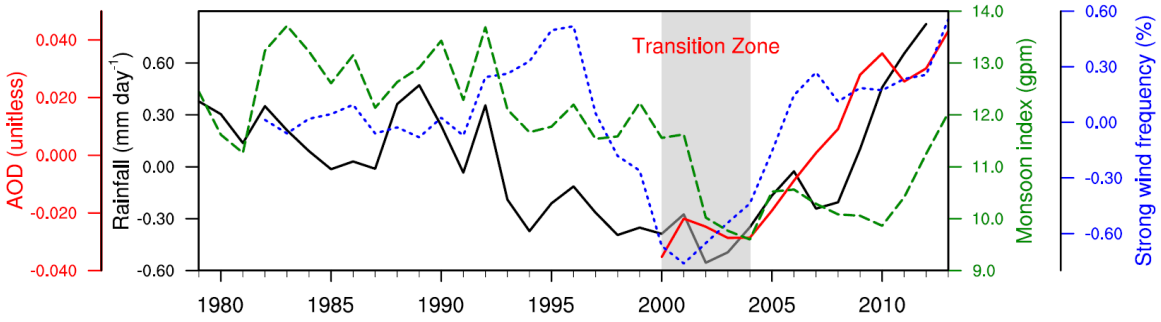

Figure 5.1. Time series of MISR AOD (unitless) at 550 nm over the Arabian Peninsula (8°–35° N, 40°–80° E), the ISM rainfall (mm day^{-1}) from TRMM in central and north India (20°–28° N, 76°–87° E), the ISM index, and strong wind frequency in dust source regions in the Arabian Peninsula (20°–40° N,40°–60° E). All values are averaged for JJA.

Figure 5.1 shows the time series of area-averaged AOD (8°–35° N, 40°–80° E), rainfall (20°–28° N, 76°–87° E), monsoon index, strong wind frequency from during JJA from 1979 to 2013. The monsoon index is defined based the south-north thermal contrast

represented by difference in geopotential height thickness in the lower troposphere following (Dai et al., 2013) as

$$ISMI \approx Z(200-500\ \text{hPa}, 60°-100°\ \text{E}, 20°-40°\ \text{N}) - Z(200-500\ \text{hPa}, 60°-100°\ \text{E}, 10°\ \text{S}-10°\ \text{N}) \quad (5.1)$$

The yearly strong wind frequency is defined by the area-averaged percentage of hourly wind speed greater than 8 m s over dust source regions in the Arabian Peninsula (20°–40° N, 40°–60° E) during JJA. The ISM rainfall shows a decreasing trend from 1980 to ~ 2000, after which it transitions to a sharp increase. This transition of the ISM rainfall is associated with the ISM index change, indicating that the rainfall transition is related to the change in the large-scale monsoon thermodynamics. It is very interesting to see a dramatically increasing trend of AOD over the Arabian Peninsula during 2000 and 2013. Due to the lack of consistent satellite AOD datasets before 2000, the hourly surface winds were used as AOD proxy. The MERRA hourly wind speed at 10 m above the surface is used to calculate the frequency of strong wind speed (> 8 m s^{-1}) in JJA, as shown in Figure 5.1. During 2000 to 2013, the wind frequency shows an increasing trend in a fashion similar to AOD, implying that the increasing AOD trend can be attributed to changes in wind speed and that wind speed is a good proxy for AOD. Before 2000, the wind speed frequency generally shows a decreasing trend, although it peaks around 1995. During the entire period of 1979 to 2013, both the ISM rainfall and the AOD proxy show a consistently decreasing trend before 2000 and an increasing trend after 2000, which to some extent suggests the positive relationship between the ISM rainfall and Middle East dust.

Figure 5.2 illustrates the spatial patterns of changes in rainfall from CRU and winds at 850 hPa from MERRA before and after the transition around 2000. The differences are calculated by simply subtracting the fields in the first half of period from the second half. Before the transition, the ISM rainfall decreases in south and east India, but increases in

west central India. However, after the transition, it shows a consistent increase across India. Notice that the increased rainfall spatial pattern follows the topography with a dramatic increase in Coastal Southwest India, central and east India, north India, and north Pakistan. Another obvious difference is a strong cyclone over the Arabian Sea before the transition and an anticyclone after the transition. The increased rainfall after the transition can be attributed to the stronger westerly monsoon flow over the Arabian Sea, the northerly flow over the Indian subcontinent, and the southeasterly flow over the Bay of Bengal. Figure 5.3 demonstrates the similar spatial patterns of changes in rainfall using NOAA datasets.

Figure 5.3 shows the spatial pattern of changes in frequency of strong wind speed. There are less strong winds in Iraq and weak changes in other areas in the Arabian Peninsula before the transition. However, more strong winds have been detected in Iraq and east of central Saudi Arabia after the transition. These prominent wind change spatial patters are located in the dust source regions (Figure 3.1b), thus resulting in changes in dust activities.

Figure 5.4 shows the global distributions of linear trends of yearly AOD from 2003 to 2012 using various satellite and aerosol reanalysis datasets. One of the most obvious trends is located in the Arabian Peninsula, the Arabian Sea, and south India, where AOD shows rather strong positive trends with a magnitude of 0.01 AOD year^{-1}. Figure 5.5 illustrates the linear trends of seasonal AOD using monthly anomalies during 2003 and 2012. The positive yearly AOD trends over Arabian and the surrounding regions shown in Figure 5.4 are attributed to increasing AOD during the boreal spring and summer with stronger trends in the boreal summer than spring, as shown in Figure 5.5. There are significant AOD trends in other regions, such as the western part of Amazon rainforest, but I will focus only on AOD trends in the Middle East.

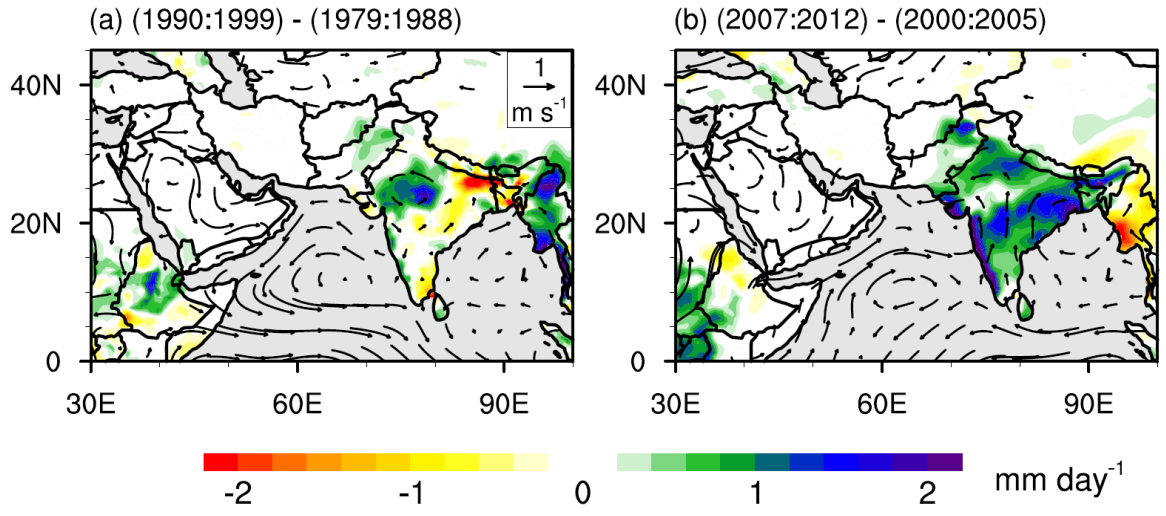

Figure 5.2. Changes in rainfall (shaded; units: mm day^{-1}) and winds (arrows; units: m s^{-1}) at 850 hPa in JJA for (a) 1982−1999, and (b) 2000−2012). Grey color means missing values of rainfall trend.

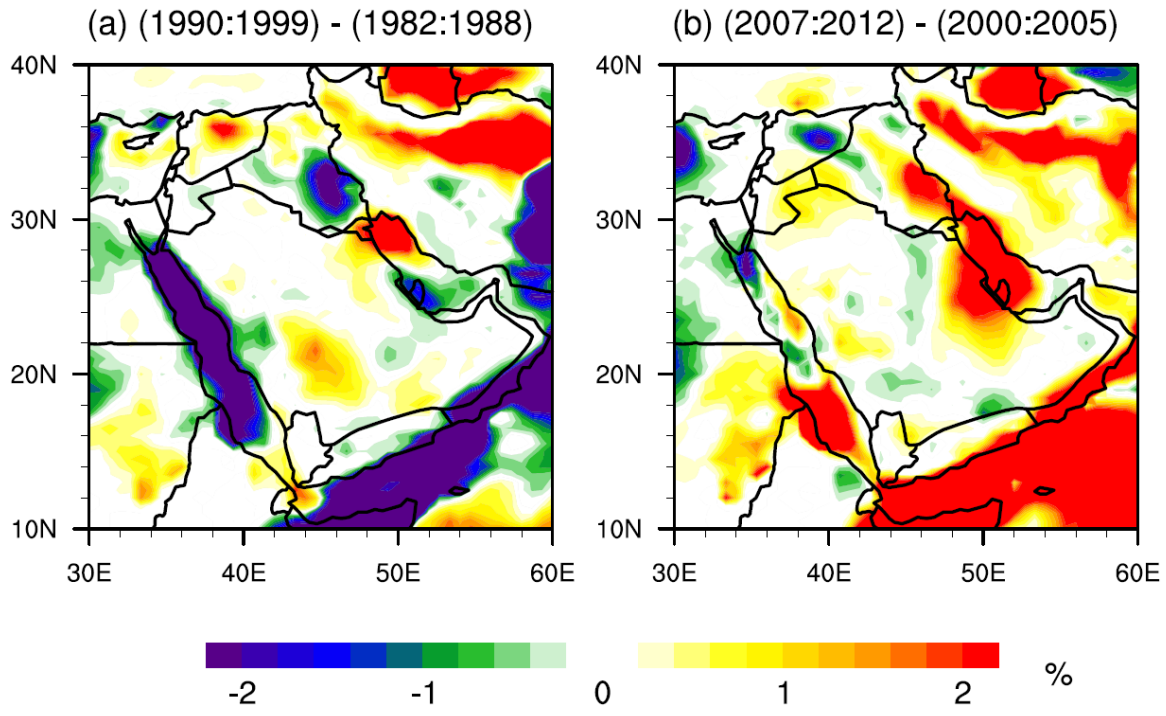

Figure 5.3. Changes in frequency (%) of strong wind (> 5 m s^{-1}) in JJA for (a) 1982−1999, and (b) 2000−2012). The frequency is calculated from MERRA hourly wind.

Corresponding to AOD trends in the Middle East and the Arabian Sea, Figure 5.6 shows the rainfall trends (mm day^{-1} $year^{-1}$) based on monthly anomalies during JJA from 2003 to 2012. All of the four datasets illustrate quite consistent positive trends of rainfall with a magnitude of about 0.08 mm day^{-1} $year^{-1}$ in Pakistan, north and central India, Coastal South and West India. It is worth pointing out that the patterns of positive rainfall trends are fairly similar to the observed and simulated positive rainfall responses to Middle East dust aerosols in Chapters 2, 3 and 4, which suggests that the increasing dust activities in Middle East dust may be responsible for the observed wetting trend in the ISM rainfall during the past decade. Simulations on longer timescales, e.g. inter-annual and decadal timescales, will be conducted trying to figure out the contributors to the observed drying trend in the ISM during the second half of twentieth century, the observed wetting trend in the ISM during the past 15 years, and the ISM rainfall transition between these two periods.

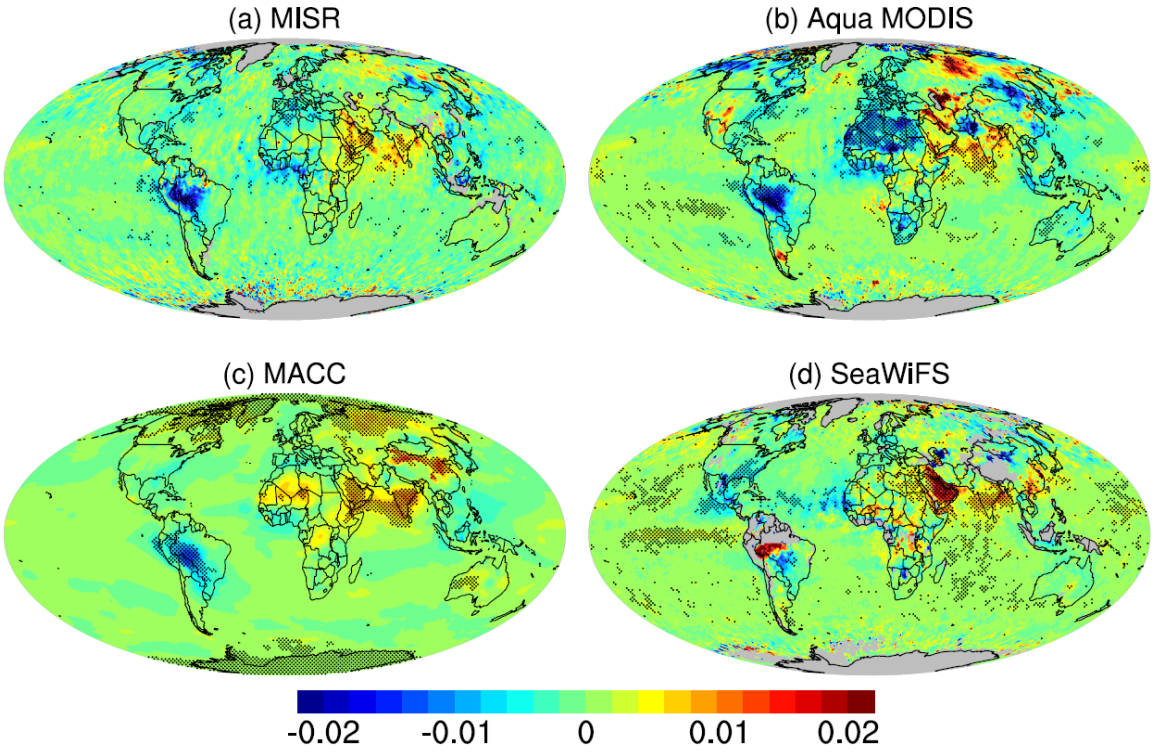

Figure 5.4. Spatial pattern of linear trend (AOD year^{-1}) of yearly AOD from 2003 to 2012 for row (a) MISR, (b) MODIS Aqua, (c) MACC, and (d) SeaWiFS. Areas that are significant at the 95% level are dotted. The grey color in Figures rows of (a), (b), and (d) are missing values.

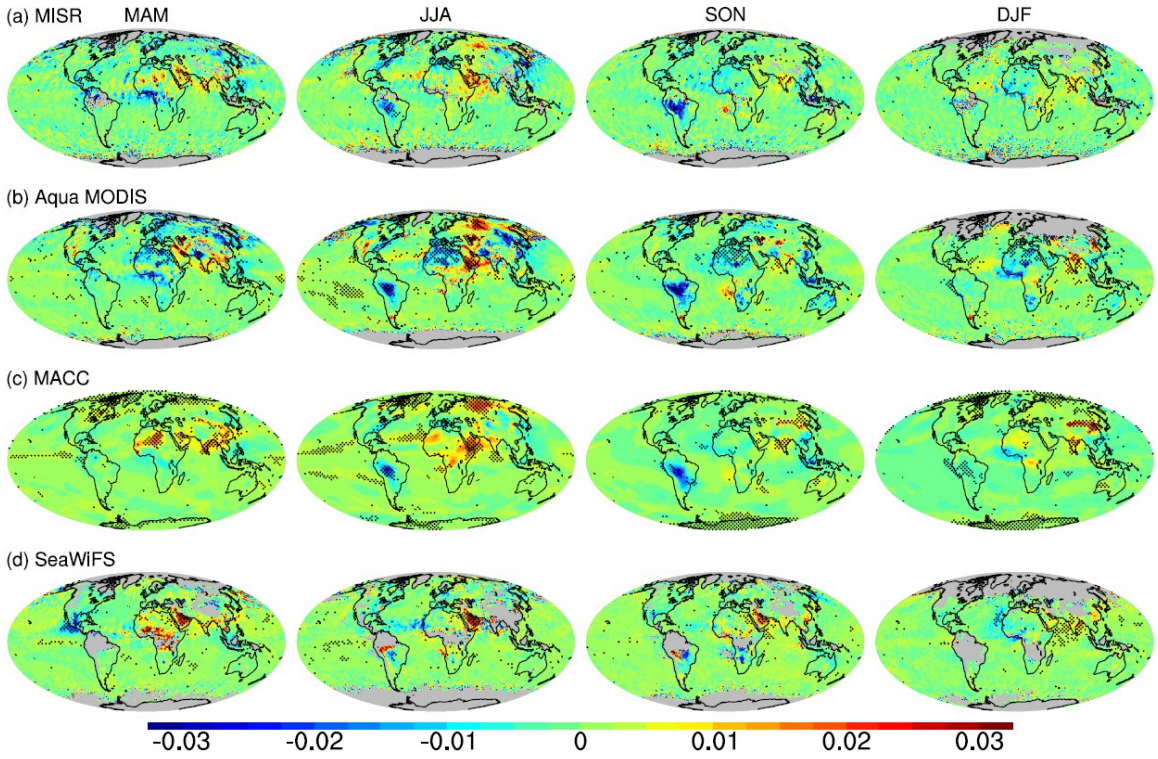

Figure 5.5. Spatial pattern of linear trend (AOD year^{-1}) of monthly AOD anomalies during MAM, JJA, SON and DJF from 2000 to 2013 for row (a) MISR, (b) MODIS Aqua, (c) MACC, and (d) SeaWiFS. Areas that are significant at the 95% level are dotted. The grey color in rows of (a), (b), and (d) are missing values.

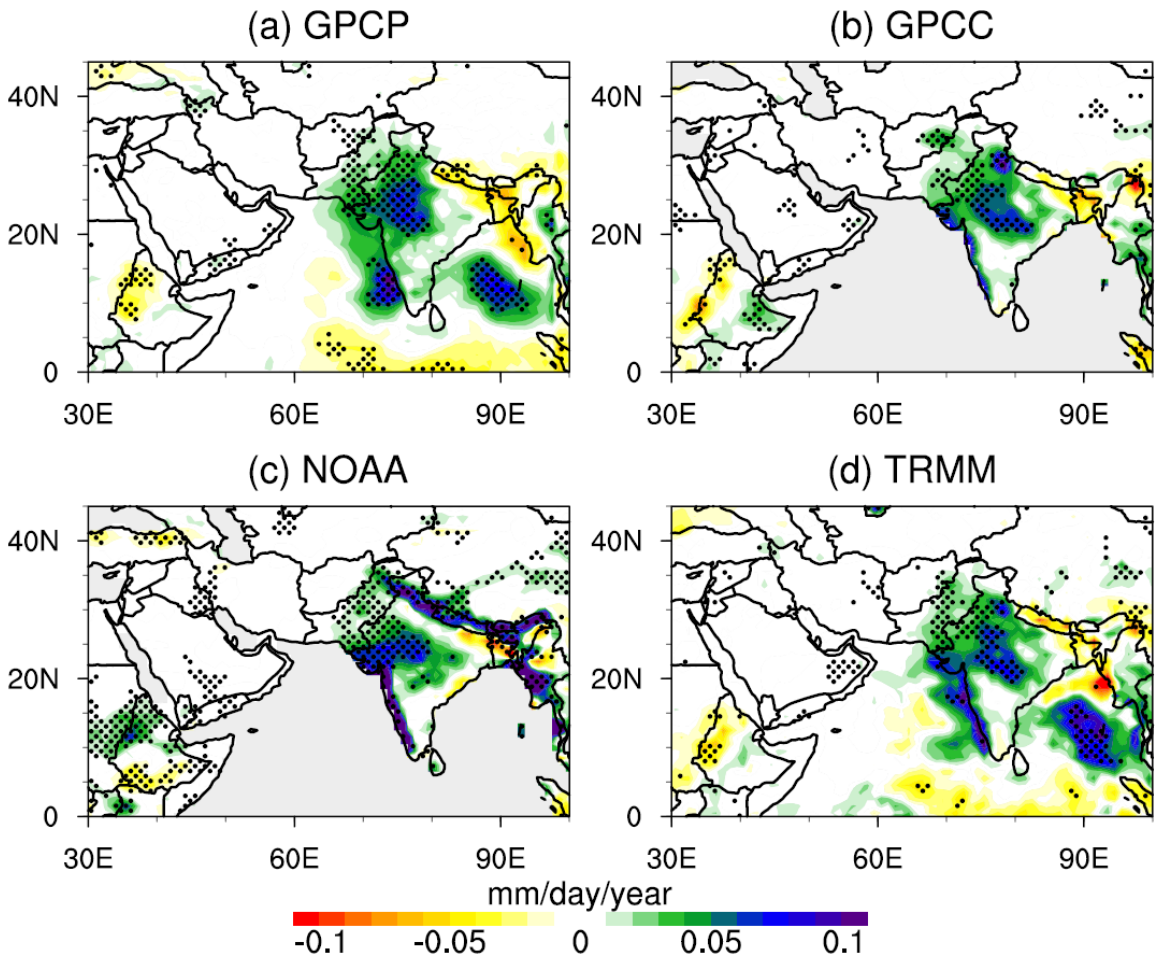

Figure 5.6. Spatial pattern of linear trend of monthly rainfall anomalis (mm day^{-1} year^{-1}) during JJAS from 2003 to 2012 for (a) GPCP, (b) GPCC, (c) NOAA, and (d) TRMM. The areas that are significant at the 95% level are dotted. Grey color in (b) and (c) presents missing values.

5.2.2. Aerosol Indirect Effects

As mentioned in Chapter 4, aerosol indirect effects are not fully considered in this work due to the lack of parameterizations of aerosol indirect effects in WRF-Chem cumulus schemes, which could result in significant uncertainties in the conclusions. Currently, some efforts have been made to couple the aerosol indirect effects with cumulus parameterizations for simulations with horizontal resolution greater than 10 km (e.g. PNNL

and NOAA). Before the release of the aerosol–cloud interactions in cumulus parameterizations in WRF-Chem, an alternative approach is the nesting technique, which allows high-resolution (i.e. cloud-resolving) simulations, in a region of interest and coarse resolutions in the other regions of the model domain. Different options for a specific physical scheme can be selected for different nested domains.

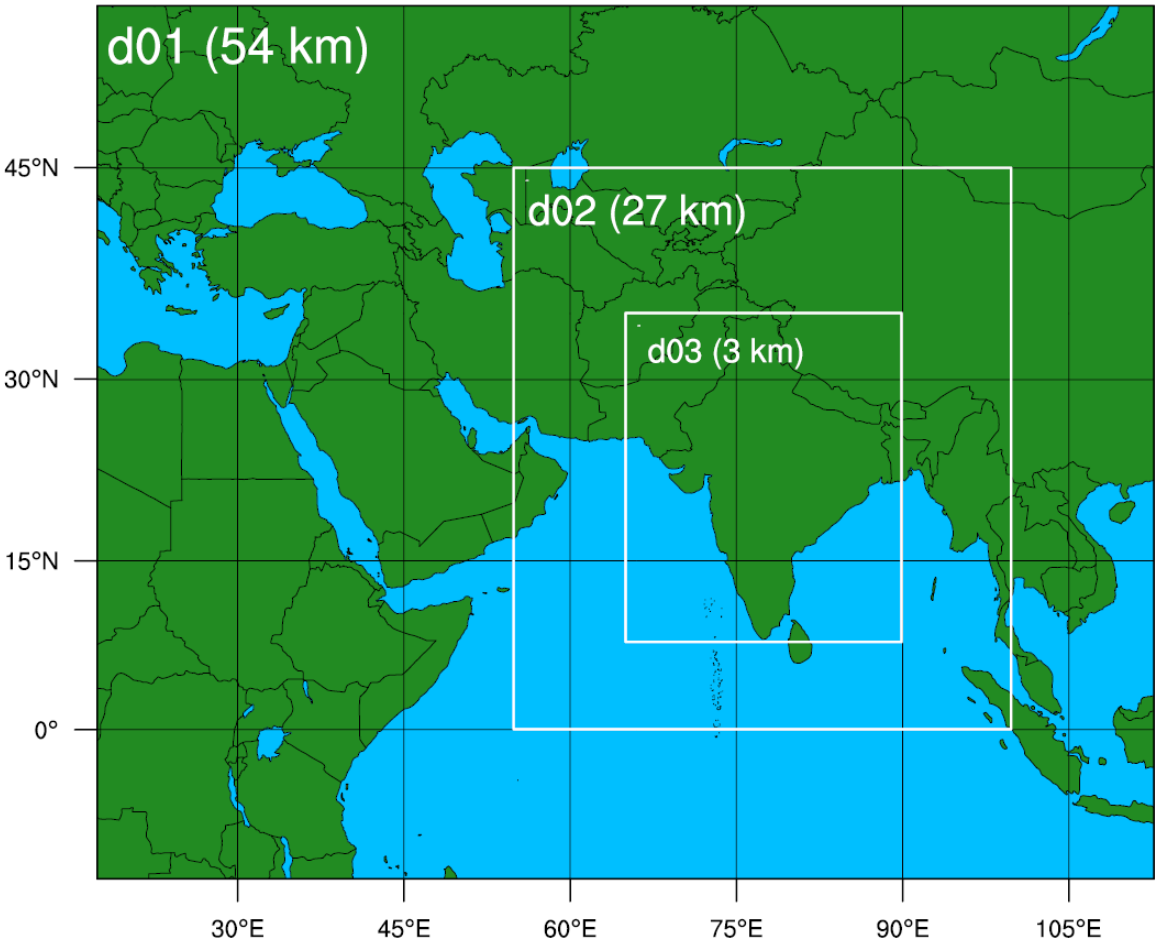

Figure 5.7. WRF-Chem nested domains for simulating aerosol indirect effects.

Figure 5.7 shows a map of the nested domains. The biggest domain includes the ISM region and its surrounding regions with the coarsest horizontal resolution of 54 km, followed by the first and second nested domains with 27-km and 3-km resolutions

respectively. For domain 1 and domain 2, the cumulus schemes should be turned on, while for domain 3, cumulus scheme should be turned off because with 3-km resolution, the microphysics scheme can simulate the convective clouds. Therefore, the aerosol indirect effects are fully considered in domain 3, where most of the dust induced rainfall increases occur, as shown in previous Chapters.

5.2.3. Model Deficiencies in Vegetation and Surface Parameters

The Noah land surface scheme in WRF-Chem calculates leaf area index (LAI) and land surface albedo based on land use categories and vegetation fraction (Chen et al., 2001; Xiu and Pleim, 2001). Each land use category corresponds to a pair of maximum and minimum of LAI and albedo in each month, which is derived from MODIS datasets and read in the model from a table. The LAI or albedo at a specific grid point equals to the sum of the minimum and maximum LAI or albedo weighted by the vegetation fraction, as shown in Figure 5.8a. The LAI and albedo from the table can capture the general temporal and spatial variability of LAI and albedo, but they cannot well capture LAI and albedo in a specific region during a specific month, as shown in Figure 5.8d.

Figure 5.8b shows the climatology (2000 to 2009) of MODIS LAI during JJA. Model overestimates LAI in the Indian subcontinent, the Middle East, but underestimates LAI in East Africa and Southeast Asia, as shown in Figure 5.8d. Since WRF-Chem version 3.6, users can use MODIS climatology LAI (Figure 5.8b), but differences still exist between the climatology and monthly LAI (Figure 5.8c). The similar situation occurs for the surface albedo, as shown in Figure 5.9.

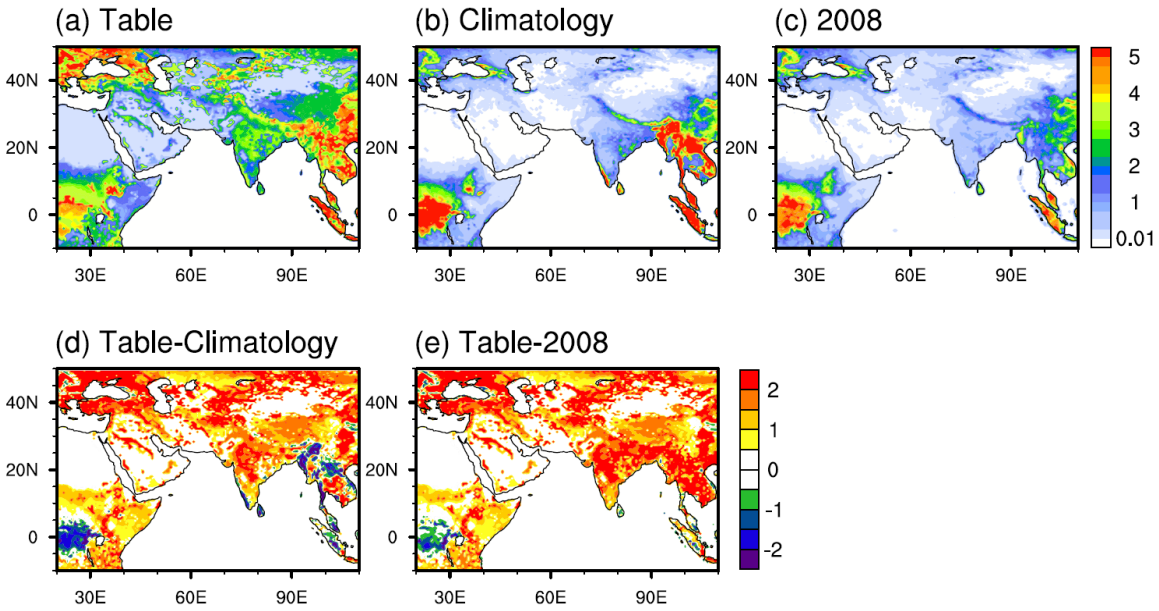

Figure 5.8. Spatial distribution of three types of LAI during JJA 2008 used in WRF-Chem for (a) default model LAI read from a table based on vegetation types, (b) climatology from MODIS, and (c) MODIS LAI for JJA 2008. The differences between default model LAI and the other two LAI data sets are shown in (d) table values minus climatology values and (e) table values minus values in JJA 2008.

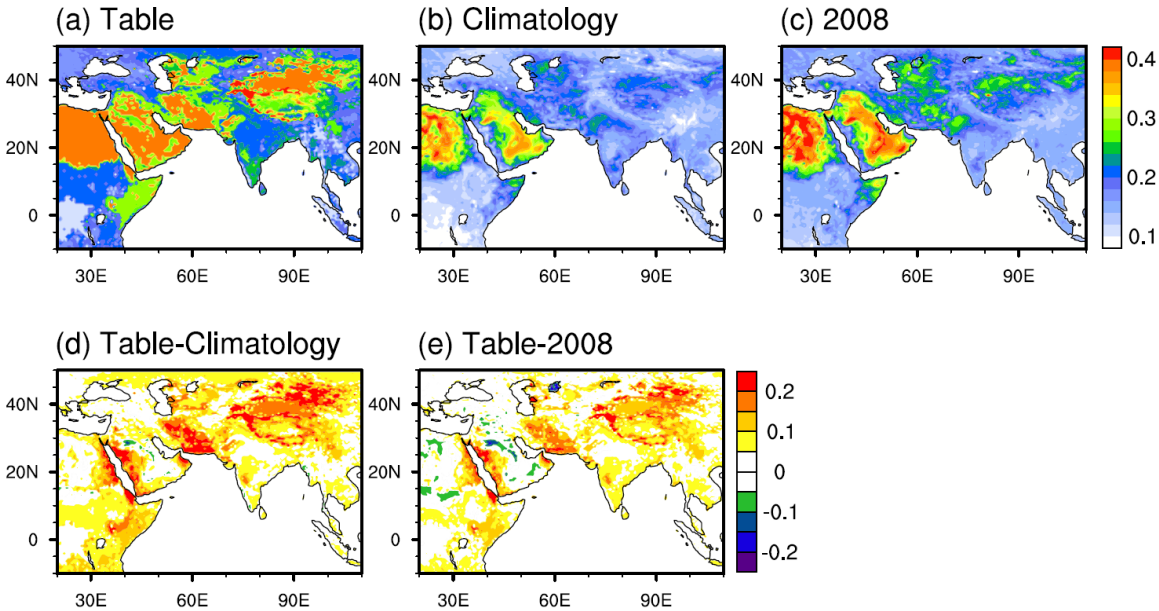

Figure 5.9. Same as Figure 5.8, but for the surface albedo.

The table values of LAI and surface albedo can significantly degrade model performance in precipitation, surface air temperature as well as latent and sensible heat fluxes in U.S. (Xu et al., 2014). Therefore, the incorporation of MODIS LAI and surface albedo in the future simulations is expected to reduce model uncertainties induced by vegetation parameterizations.

5.2.4. Other Potential Uncertainties

Besides the abovementioned uncertainties due to aerosol indirect effects and vegetation parameterizations, other uncertainties should also be considered. The responses of sea surface temperatures to dust radiative forcing at the surface could change west–east ocean–land thermal contrast between the Arabian Sea and the India subcontinent, which can modulate the monsoon water vapor budget and rainfall. Furthermore, the dust absorbing ability determines the magnitude of its atmospheric heating rates, therefore dominates the magnitude of the ISM rainfall responses. The absorbing abilities of aerosols are parameterized by the imaginary parts of aerosol complex refractive indices at different wavelengths in most GCMs and RCMs. Observations show that the imaginary parts of dust aerosols span a wide range from 0.001 to almost 0.006 at 550 nm (Sokolik et al., 1993; Muller et al., 2009; Petzold et al., 2009; Muller et al., 2011; Wagner et al., 2012), which may be another significant uncertainty.

In the future simulations, the slab ocean model in WRF-Chem needs to be used to consider the dust-induced radiative forcing in the SSTs in the Arabian Sea. Additionally, more observations and analyses of dust chemical compositions and absorbing abilities are needed in the Middle East to better constrain model uncertainties in simulating atmospheric heating by dust aerosols (Scanza et al., 2015).

5.3. OUTLOOK

As part of the Earth's climate system, aerosols can interact with the other parts of the climate system and have been drawing increasing attention since the 20th century. More and more researches have focused on various aerosol types and their impacts on both nature and human health (Poschl, 2005). A number of discoveries about aerosols are exciting. However, we have more unknowns than what we have known about aerosols and many debates are emerged about aerosols, mainly due to limited observations of aerosol physical and chemical properties on the global scale and complex chemical reactions occurring on aerosol particles.

Satellite can provide global observations of aerosol properties, such as AOD, and Ångström exponent that is associated with aerosol particle size. These observations are useful to study the spatial distribution of aerosols, but the associated large uncertainties may induce controversy between satellite and model results. Therefore, more surface observational datasets are needed to better parameterize aerosols' physical and chemical properties, such as their chemical compositions and absorbing ability of the solar radiation.

Numerical modeling is beneficial to a better understanding of the interactions between aerosols and the climate system, but their results are highly tunable. Numerical models have a large number of parameters, by tuning which one can get expected results to some extent. However, the tuned parameters are not arbitrary and should be at least in a reasonable range.

Finally yet importantly, some researchers exaggerate human influences on the climate system, trying to attribute changes in the climate system to human impacts, such as manmade pollutions. These assertions of human impacts on the climate system should be treated with extreme caution, because of the natural variability of the climate system on multiple timescales and the uncertainty in the historic anthropogenic emission inventory.

References

Ackermann, I. J., Hass, H., Memmesheimer, M., Ebel, A., Binkowski, F. S., and Shankar, U.: Modal aerosol dynamics model for Europe: Development and first applications, Atmos Environ, 32, 2981-2999, 1998.

Albani, S., Mahowald, N. M., Perry, A. T., Scanza, R. A., Zender, C. S., Heavens, N. G., Maggi, V., Kok, J. F., and Otto-Bliesner, B. L.: Improved dust representation in the Community Atmosphere Model, Journal of Advances in Modeling Earth Systems, 6, 541–570, 2014.

Albrecht, B. A.: Aerosols, Cloud Microphysics, and Fractional Cloudiness, Science, 245, 1227-1230, 1989.

Barnard, J. C., Fast, J. D., Paredes-Miranda, G., Arnott, W. P., and Laskin, A.: Technical Note: Evaluation of the WRF-Chem "Aerosol Chemical to Aerosol Optical Properties" Module using data from the MILAGRO campaign, Atmos Chem Phys, 10, 7325-7340, 2010.

Benedetti, A., Morcrette, J. J., Boucher, O., Dethof, A., Engelen, R. J., Fisher, M., Flentje, H., Huneeus, N., Jones, L., Kaiser, J. W., Kinne, S., Mangold, A., Razinger, M., Simmons, A. J., and Suttie, M.: Aerosol analysis and forecast in the European Centre for Medium-Range Weather Forecasts Integrated Forecast System: 2. Data assimilation, J Geophys Res-Atmos, 114, 2009.

Binkowski, F. S. and Shankar, U.: The Regional Particulate Matter Model .1. Model description and preliminary results, J Geophys Res-Atmos, 100, 26191-26209, 1995.

Bollasina, M. A., Ming, Y., and Ramaswamy, V.: Anthropogenic Aerosols and the Weakening of the South Asian Summer Monsoon, Science, 334, 502-505, 2011.

Bollasina, M. A., Ming, Y., and Ramaswamy, V.: Earlier onset of the Indian monsoon in the late twentieth century: The role of anthropogenic aerosols, Geophys Res Lett, 40, 3715-3720, 2013.

Bollasina, M. A., Ming, Y., Ramaswamy, V., Schwarzkopf, M. D., and Naik, V.: Contribution of local and remote anthropogenic aerosols to the twentieth century weakening of the South Asian Monsoon, Geophys Res Lett, 41, 680-687, 2014.

Boucher, O. and Quaas, J.: Water vapour affects both rain and aerosol optical depth, Nat Geosci, 6, 3-5, 2013.

Bretherton, C. S., Smith, C., and Wallace, J. M.: An Intercomparison of Methods for Finding Coupled Patterns in Climate Data, J Climate, 5, 541-560, 1992.

Chapman, E. G., Gustafson, W. I., Easter, R. C., Barnard, J. C., Ghan, S. J., Pekour, M. S., and Fast, J. D.: Coupling aerosol-cloud-radiative processes in the WRF-Chem model: Investigating the radiative impact of elevated point sources, Atmos Chem Phys, 9, 945-964, 2009.

Chen, F., Pielke, R. A., and Mitchell, K.: Development and application of land-surface models for mesoscale atmospheric models: Problems and promises, Land Surface

Hydrology, Meteorology, and Climate: Observations and Modeling, 3, 107-135, 2001.
Chen, M. Y., Xie, P. P., Janowiak, J. E., and Arkin, P. A.: Global land precipitation: A 50-yr monthly analysis based on gauge observations, J Hydrometeorol, 3, 249-266, 2002.
Cowan, T. and Cai, W.: The impact of Asian and non-Asian anthropogenic aerosols on 20th century Asian summer monsoon, Geophys Res Lett, 38, 2011.
Dai, A. G., Li, H. M., Sun, Y., Hong, L. C., Ho, L., Chou, C., and Zhou, T. J.: The relative roles of upper and lower tropospheric thermal contrasts and tropical influences in driving Asian summer monsoons, J Geophys Res-Atmos, 118, 7024-7045, 2013.
Damberg, L. and AghaKouchak, A.: Global trends and patterns of drought from space, Theor Appl Climatol, doi: 10.1007/s00704-013-1019-5, 2013. 2013.
Dee, D. P., Uppala, S. M., Simmons, A. J., Berrisford, P., Poli, P., Kobayashi, S., Andrae, U., Balmaseda, M. A., Balsamo, G., Bauer, P., Bechtold, P., Beljaars, A. C. M., van de Berg, L., Bidlot, J., Bormann, N., Delsol, C., Dragani, R., Fuentes, M., Geer, A. J., Haimberger, L., Healy, S. B., Hersbach, H., Holm, E. V., Isaksen, L., Kallberg, P., Kohler, M., Matricardi, M., McNally, A. P., Monge-Sanz, B. M., Morcrette, J. J., Park, B. K., Peubey, C., de Rosnay, P., Tavolato, C., Thepaut, J. N., and Vitart, F.: The ERA-Interim reanalysis: configuration and performance of the data assimilation system, Q J Roy Meteor Soc, 137, 553-597, 2011.
Diner, D. J., Beckert, J. C., Reilly, T. H., Bruegge, C. J., Conel, J. E., Kahn, R. A., Martonchik, J. V., Ackerman, T. P., Davies, R., Gerstl, S. A. W., Gordon, H. R., Muller, J. P., Myneni, R. B., Sellers, P. J., Pinty, B., and Verstraete, M. M.: Multi-angle Imaging SpectroRadiometer (MISR) - Instrument description and experiment overview, Ieee T Geosci Remote, 36, 1072-1087, 1998.
Douglas, E. M., Beltran-Przekurat, A., Niyogi, D., Pielke, R. A., and Vorosmarty, C. J.: The impact of agricultural intensification and irrigation on land-atmosphere interactions and Indian monsoon precipitation - A mesoscale modeling perspective, Global Planet Change, 67, 117-128, 2009.
Easter, R. C., Ghan, S. J., Zhang, Y., Saylor, R. D., Chapman, E. G., Laulainen, N. S., Abdul-Razzak, H., Leung, L. R., Bian, X. D., and Zaveri, R. A.: MIRAGE: Model description and evaluation of aerosols and trace gases, J Geophys Res-Atmos, 109, 2004.
Evan, A. T., Kossin, J. P., Chung, C., and Ramanathan, V.: Arabian Sea tropical cyclones intensified by emissions of black carbon and other aerosols, Nature, 479, 94-U119, 2011.
Fast, J. D., Gustafson, W. I., Easter, R. C., Zaveri, R. A., Barnard, J. C., Chapman, E. G., Grell, G. A., and Peckham, S. E.: Evolution of ozone, particulates, and aerosol direct radiative forcing in the vicinity of Houston using a fully coupled meteorology-chemistry-aerosol model, J Geophys Res-Atmos, 111, 2006.
Fasullo, J. and Webster, P. J.: A hydrological definition of Indian monsoon onset and withdrawal, J Climate, 16, 3200-3211, 2003.

Fecan, F., Marticorena, B., and Bergametti, G.: Parametrization of the increase of the aeolian erosion threshold wind friction velocity due to soil moisture for arid and semi-arid areas, Ann Geophys-Atm Hydr, 17, 149-157, 1999.

Flanner, M. G.: Arctic climate sensitivity to local black carbon, J Geophys Res-Atmos, 118, 1840-1851, 2013.

Ganguly, D., Rasch, P. J., Wang, H. L., and Yoon, J. H.: Climate response of the South Asian monsoon system to anthropogenic aerosols, J Geophys Res-Atmos, 117, 2012.

Ghan, S., Laulainen, N., Easter, R., Wagener, R., Nemesure, S., Chapman, E., Zhang, Y., and Leung, R.: Evaluation of aerosol direct radiative forcing in MIRAGE, J Geophys Res-Atmos, 106, 5295-5316, 2001.

Ginoux, P., Chin, M., Tegen, I., Prospero, J. M., Holben, B., Dubovik, O., and Lin, S. J.: Sources and distributions of dust aerosols simulated with the GOCART model, J Geophys Res-Atmos, 106, 20255-20273, 2001.

Gong, S. L. and Barrie, L. A.: Simulating the impact of sea salt on global nss sulphate aerosols, J Geophys Res-Atmos, 108, 2003.

Grell, G. A. and Devenyi, D.: A generalized approach to parameterizing convection combining ensemble and data assimilation techniques, Geophys Res Lett, 29, 2002.

Grell, G. A., Peckham, S. E., Schmitz, R., McKeen, S. A., Frost, G., Skamarock, W. C., and Eder, B.: Fully coupled "online" chemistry within the WRF model, Atmos Environ, 39, 6957-6975, 2005.

Guenther, A. B., Jiang, X., Heald, C. L., Sakulyanontvittaya, T., Duhl, T., Emmons, L. K., and Wang, X.: The Model of Emissions of Gases and Aerosols from Nature version 2.1 (MEGAN2.1): an extended and updated framework for modeling biogenic emissions, Geosci Model Dev, 5, 1471-1492, 2012.

Hansen, J., Sato, M., and Ruedy, R.: Radiative forcing and climate response, J Geophys Res-Atmos, 102, 6831-6864, 1997.

Hong, S. Y., Noh, Y., and Dudhia, J.: A new vertical diffusion package with an explicit treatment of entrainment processes, Mon Weather Rev, 134, 2318-2341, 2006.

Hsu, N. C., Gautam, R., Sayer, A. M., Bettenhausen, C., Li, C., Jeong, M. J., Tsay, S. C., and Holben, B. N.: Global and regional trends of aerosol optical depth over land and ocean using SeaWiFS measurements from 1997 to 2010, Atmos Chem Phys, 12, 8037-8053, 2012.

Hsu, N. C., Tsay, S. C., King, M. D., and Herman, J. R.: Aerosol properties over bright-reflecting source regions, Ieee T Geosci Remote, 42, 557-569, 2004.

Huang, J., Fu, Q., Su, J., Tang, Q., Minnis, P., Hu, Y., Yi, Y., and Zhao, Q.: Taklimakan dust aerosol radiative heating derived from CALIPSO observations using the Fu-Liou radiation model with CERES constraints, Atmos Chem Phys, 9, 4011-4021, 2009.

Huffman, G. J., Adler, R. F., Bolvin, D. T., Gu, G. J., Nelkin, E. J., Bowman, K. P., Hong, Y., Stocker, E. F., and Wolff, D. B.: The TRMM multisatellite precipitation analysis (TMPA): Quasi-global, multiyear, combined-sensor precipitation estimates at fine scales, J Hydrometeorol, 8, 38-55, 2007.

Iacono, M. J., Delamere, J. S., Mlawer, E. J., Shephard, M. W., Clough, S. A., and Collins, W. D.: Radiative forcing by long-lived greenhouse gases: Calculations with the AER radiative transfer models, J Geophys Res-Atmos, 113, 2008.

IPCC: Climate Change 2000: The scientific basis, 2001. 2001.

Iqbal, M. J., Baig, M. J., and Naz, S.: Dominant impact of South Asian low heat on summer monsoon rainfall over Central India, Arab J Geosci, 6, 2001-2008, 2013.

Jeong, M. J., Li, Z. Q., Andrews, E., and Tsay, S. C.: Effect of aerosol humidification on the column aerosol optical thickness over the Atmospheric Radiation Measurement Southern Great Plains site, J Geophys Res-Atmos, 112, 2007.

Jin, Q. J., Wei, J. F., and Yang, Z. L.: Positive response of Indian summer rainfall to Middle East dust, Geophys Res Lett, 41, 4068-4074, 2014.

Kuhlmann, J. and Quaas, J.: How can aerosols affect the Asian summer monsoon? Assessment during three consecutive pre-monsoon seasons from CALIPSO satellite data, Atmos Chem Phys, 10, 4673-4688, 2010.

Kulmala, M., Toivonen, A., Makela, J. M., and Laaksonen, A.: Analysis of the growth of nucleation mode particles observed in Boreal forest, Tellus B, 50, 449-462, 1998.

Lau, K. M. and Kim, K. M.: Comment on "'Elevated heat pump' hypothesis for the aerosol-monsoon hydroclimate link: 'Grounded' in observations?" by S. Nigam and M. Bollasina, J Geophys Res-Atmos, 116, 2011.

Lau, K. M. and Kim, K. M.: Observational relationships between aerosol and Asian monsoon rainfall, and circulation, Geophys Res Lett, 33, 2006.

Lau, K. M., Kim, M. K., and Kim, K. M.: Asian summer monsoon anomalies induced by aerosol direct forcing: the role of the Tibetan Plateau, Clim Dynam, 26, 855-864, 2006.

Levine, R. C. and Turner, A. G.: Dependence of Indian monsoon rainfall on moisture fluxes across the Arabian Sea and the impact of coupled model sea surface temperature biases, Clim Dynam, 38, 2167-2190, 2012.

Liu, X., Easter, R. C., Ghan, S. J., Zaveri, R., Rasch, P., Shi, X., Lamarque, J. F., Gettelman, A., Morrison, H., Vitt, F., Conley, A., Park, S., Neale, R., Hannay, C., Ekman, A. M. L., Hess, P., Mahowald, N., Collins, W., Iacono, M. J., Bretherton, C. S., Flanner, M. G., and Mitchell, D.: Toward a minimal representation of aerosols in climate models: description and evaluation in the Community Atmosphere Model CAM5, Geosci Model Dev, 5, 709-739, 2012.

Lohmann, U. and Feichter, J.: Global indirect aerosol effects: a review, Atmos Chem Phys, 5, 715-737, 2005.

Mahowald, N.: Aerosol Indirect Effect on Biogeochemical Cycles and Climate, Science, 334, 794-796, 2011.

Mahowald, N., Albani, S., Kok, J. F., Engelstaeder, S., Scanza, R., Ward, D. S., and Flanner, M. G.: The size distribution of desert dust aerosols and its impact on the Earth system, Aeolian Res, 15, 53-71, 2014.

McFiggans, G., Artaxo, P., Baltensperger, U., Coe, H., Facchini, M. C., Feingold, G., Fuzzi, S., Gysel, M., Laaksonen, A., Lohmann, U., Mentel, T. F., Murphy, D. M., O'Dowd, C. D., Snider, J. R., and Weingartner, E.: The effect of physical and

chemical aerosol properties on warm cloud droplet activation, Atmos Chem Phys, 6, 2593-2649, 2006.
Meehl, G. A., Arblaster, J. M., and Collins, W. D.: Effects of black carbon aerosols on the Indian monsoon, J Climate, 21, 2869-2882, 2008.
Middleton, P., Stockwell, W. R., and Carter, W. P. L.: Aggregation and Analysis of Volatile Organic-Compound Emissions for Regional Modeling, Atmos Environ a-Gen, 24, 1107-1133, 1990.
Mishra, V., Smoliak, B. V., Lettenmaier, D. P., and Wallace, J. M.: A prominent pattern of year-to-year variability in Indian Summer Monsoon Rainfall, P Natl Acad Sci USA, 109, 7213-7217, 2012.
Morcrette, J. J., Boucher, O., Jones, L., Salmond, D., Bechtold, P., Beljaars, A., Benedetti, A., Bonet, A., Kaiser, J. W., Razinger, M., Schulz, M., Serrar, S., Simmons, A. J., Sofiev, M., Suttie, M., Tompkins, A. M., and Untch, A.: Aerosol analysis and forecast in the European Centre for Medium-Range Weather Forecasts Integrated Forecast System: Forward modeling, J Geophys Res-Atmos, 114, 2009.
Moron, V. and Robertson, A. W.: Interannual variability of Indian summer monsoon rainfall onset date at local scale, Int J Climatol, 34, 1050-1061, 2014.
Muller, T., Schladitz, A., Kandler, K., and Wiedensohler, A.: Spectral particle absorption coefficients, single scattering albedos and imaginary parts of refractive indices from ground based in situ measurements at Cape Verde Island during SAMUM-2, Tellus B, 63, 573-588, 2011.
Muller, T., Schladitz, A., Massling, A., Kaaden, N., Kandler, K., and Wiedensohler, A.: Spectral absorption coefficients and imaginary parts of refractive indices of Saharan dust during SAMUM-1, Tellus B, 61, 79-95, 2009.
Myhre, G., Stordal, F., Johnsrud, M., Kaufman, Y. J., Rosenfeld, D., Storelvmo, T., Kristjansson, J. E., Berntsen, T. K., Myhre, A., and Isaksen, I. S. A.: Aerosol-cloud interaction inferred from MODIS satellite data and global aerosol models, Atmos Chem Phys, 7, 3081-3101, 2007.
Nigam, S. and Bollasina, M.: "Elevated heat pump" hypothesis for the aerosol-monsoon hydroclimate link: "Grounded" in observations?, J Geophys Res-Atmos, 115, 2010.
Nigam, S. and Bollasina, M.: Reply to comment by K. M. Lau and K. M. Kim on '"Elevated heat pump' hypothesis for the aerosol-monsoon hydroclimate link: 'Grounded' in observations?", J Geophys Res-Atmos, 116, 2011.
Peters, K. and Eiden, R.: Modeling the Dry Deposition Velocity of Aerosol-Particles to a Spruce Forest, Atmos Environ a-Gen, 26, 2555-2564, 1992.
Petzold, A., Rasp, K., Weinzierl, B., Esselborn, M., Hamburger, T., Dornbrack, A., Kandler, K., Schutz, L., Knippertz, P., Fiebig, M., and Virkkula, A.: Saharan dust absorption and refractive index from aircraft-based observations during SAMUM 2006, Tellus B, 61, 118-130, 2009.
Poschl, U.: Atmospheric aerosols: Composition, transformation, climate and health effects, Angew Chem Int Edit, 44, 7520-7540, 2005.
Prospero, J. M., Ginoux, P., Torres, O., Nicholson, S. E., and Gill, T. E.: Environmental characterization of global sources of atmospheric soil dust identified with the

Nimbus 7 Total Ozone Mapping Spectrometer (TOMS) absorbing aerosol product, Rev Geophys, 40, 2002.
Qian, Y., Flanner, M. G., Leung, L. R., and Wang, W.: Sensitivity studies on the impacts of Tibetan Plateau snowpack pollution on the Asian hydrological cycle and monsoon climate, Atmos Chem Phys, 11, 1929-1948, 2011.
Rahul, P. R. C., Salvekar, P. S., and Devara, P. C. S.: Aerosol optical depth variability over Arabian Sea during drought and normal years of Indian monsoon, Geophys Res Lett, 35, 2008.
Ramanathan, V., Chung, C., Kim, D., Bettge, T., Buja, L., Kiehl, J. T., Washington, W. M., Fu, Q., Sikka, D. R., and Wild, M.: Atmospheric brown clouds: Impacts on South Asian climate and hydrological cycle, P Natl Acad Sci USA, 102, 5326-5333, 2005.
Rienecker, M. M., Suarez, M. J., Gelaro, R., Todling, R., Bacmeister, J., Liu, E., Bosilovich, M. G., Schubert, S. D., Takacs, L., Kim, G. K., Bloom, S., Chen, J. Y., Collins, D., Conaty, A., Da Silva, A., Gu, W., Joiner, J., Koster, R. D., Lucchesi, R., Molod, A., Owens, T., Pawson, S., Pegion, P., Redder, C. R., Reichle, R., Robertson, F. R., Ruddick, A. G., Sienkiewicz, M., and Woollen, J.: MERRA: NASA's Modern-Era Retrospective Analysis for Research and Applications, J Climate, 24, 3624-3648, 2011.
Ruijgrok, W., Davidson, C. I., and Nicholson, K. W.: Dry Deposition of Particles - Implications and Recommendations for Mapping of Deposition over Europe, Tellus B, 47, 587-601, 1995.
Saha, S. K., Pokhrel, S., and Chaudhari, H. S.: Influence of Eurasian snow on Indian summer monsoon in NCEP CFSv2 freerun, Clim Dynam, 41, 1801-1815, 2013.
Satheesh, S. K. and Moorthy, K. K.: Radiative effects of natural aerosols: A review, Atmos Environ, 39, 2089-2110, 2005.
Scanza, R. A., Mahowald, N., Ghan, S., Zender, C. S., Kok, J. F., Liu, X., Zhang, Y., and Albani, S.: Modeling dust as component minerals in the Community Atmosphere Model: development of framework and impact on radiative forcing, Atmos Chem Phys, 15, 537-561, 2015.
Schell, B., Ackermann, I. J., Hass, H., Binkowski, F. S., and Ebel, A.: Modeling the formation of secondary organic aerosol within a comprehensive air quality model system, J Geophys Res-Atmos, 106, 28275-28293, 2001.
Shin, H. H. and Hong, S. Y.: Intercomparison of Planetary Boundary-Layer Parametrizations in the WRF Model for a Single Day from CASES-99, Bound-Lay Meteorol, 139, 261-281, 2011.
Skamarock, W. C., Klemp, J. B., Dudhia, J., Gill, D. O., Barker, D. M., Wang, W., and Powers, J. G.: A Description of the Advanced Research WRF Version 2, NCAR TECHNICAL NOTE, 2005. 2005.
Sokolik, I., Andronova, A., and Johnson, T. C.: Complex Refractive-Index of Atmospheric Dust Aerosols, Atmos Environ a-Gen, 27, 2495-2502, 1993.

Solmon, F., Nair, V. S., and Mallet, M.: Increasing Arabian dust activity and the Indian Summer Monsoon, Atmospheric Chemistry and Physics Discussions, 15, 4879-4907, 2015.

Stockwell, W. R., Kirchner, F., Kuhn, M., and Seefeld, S.: A new mechanism for regional atmospheric chemistry modeling, J Geophys Res-Atmos, 102, 25847-25879, 1997.

Trenberth, K. E.: Atmospheric moisture recycling: Role of advection and local evaporation, J Climate, 12, 1368-1381, 1999.

Turner, A. G. and Annamalai, H.: Climate change and the South Asian summer monsoon, Nat Clim Change, 2, 587-595, 2012.

Utry, N., Ajtai, T., Pinter, M., Tombacz, E., Illes, E., Bozoki, Z., and Szabo, G.: Mass-specific optical absorption coefficients and imaginary part of the complex refractive indices of mineral dust components measured by a multi-wavelength photoacoustic spectrometer, Atmos Meas Tech, 8, 401-410, 2015.

Vinoj, V., Rasch, P. J., Wang, H., Yoon, J.-H., Ma, P.-L., Landu, K., and Singh, B.: Short-term modulation of Indian summer monsoon rainfall by West Asian dust, Nature Geoscience, doi: 10.1038/ngeo2107, 2014. 2014.

Wagner, R., Ajtai, T., Kandler, K., Lieke, K., Linke, C., Muller, T., Schnaiter, M., and Vragel, M.: Complex refractive indices of Saharan dust samples at visible and near UV wavelengths: a laboratory study, Atmos Chem Phys, 12, 2491-2512, 2012.

Wang, C., Jeong, G. R., and Mahowald, N.: Particulate absorption of solar radiation: anthropogenic aerosols vs. dust, Atmos Chem Phys, 9, 3935-3945, 2009a.

Wang, C., Kim, D., Ekman, A. M. L., Barth, M. C., and Rasch, P. J.: Impact of anthropogenic aerosols on Indian summer monsoon, Geophys Res Lett, 36, 2009b.

Webster, P. J. and Fasullo, J.: Monsoon: Dynamical Theory (Encyclopedia of Atmospheric Sciences (Second Edition)), 3, 1370-1386, 2014.

Wehner, M. F., Reed, K. A., Li, F. Y., Prabhat, Bacmeister, J., Chen, C. T., Paciorek, C., Gleckler, P. J., Sperber, K. R., Collins, W. D., Gettelman, A., and Jablonowski, C.: The effect of horizontal resolution on simulation quality in the Community Atmospheric Model, CAM5.1, J Adv Model Earth Sy, 6, 980-997, 2014.

Wesely, M. L.: Parameterization of Surface Resistances to Gaseous Dry Deposition in Regional-Scale Numerical-Models, Atmos Environ, 23, 1293-1304, 1989.

Whitby, E. R. and McMurry, P. H.: Modal aerosol dynamics modeling, Aerosol Sci Tech, 27, 673-688, 1997.

Wu, G. X., Liu, Y. M., He, B., Bao, Q., Duan, A. M., and Jin, F. F.: Thermal Controls on the Asian Summer Monsoon, Sci Rep-Uk, 2, 2012.

Xie, P. P. and Arkin, P. A.: Global precipitation: A 17-year monthly analysis based on gauge observations, satellite estimates, and numerical model outputs, B Am Meteorol Soc, 78, 2539-2558, 1997.

Xiu, A. J. and Pleim, J. E.: Development of a land surface model. Part I: Application in a mesoscale meteorological model, J Appl Meteorol, 40, 192-209, 2001.

Xu, M., Liang, X. Z., Samel, A., and Gao, W.: MODIS Consistent Vegetation Parameter Specifications and Their Impacts on Regional Climate Simulations, J Climate, 27, 8578-8596, 2014.

Zaveri, R. A., Easter, R. C., Fast, J. D., and Peters, L. K.: Model for Simulating Aerosol Interactions and Chemistry (MOSAIC), J Geophys Res-Atmos, 113, 2008.

Zaveri, R. A. and Peters, L. K.: A new lumped structure photochemical mechanism for large-scale applications, J Geophys Res-Atmos, 104, 30387-30415, 1999.

Zender, C. S., Bian, H. S., and Newman, D.: Mineral Dust Entrainment and Deposition (DEAD) model: Description and 1990s dust climatology, J Geophys Res-Atmos, 108, 2003a.

Zender, C. S., Newman, D., and Torres, O.: Spatial heterogeneity in aeolian erodibility: Uniform, topographic, geomorphic, and hydrologic hypotheses, J Geophys Res-Atmos, 108, 2003b.

Zhang, L. M., Gong, S. L., Padro, J., and Barrie, L.: A size-segregated particle dry deposition scheme for an atmospheric aerosol module, Atmos Environ, 35, 549-560, 2001.

VITA

Qinjian Jin was born in Baoji Shaanxi, China in December 1985. After graduating from Chencang Guozheng No. 1 Junior High School, he entered Lanzhou University in 2005, majoring in electronics and computer science. In 2009, he earned his Bachelor degree. With a great enthusiasm and interest in the nature, he decided to pursue a doctoral degree. In 2010, he was admitted for The University of Texas at Austin with the major of atmospheric, oceanic and climate dynamics.

Permanent email: jinqj05@gmail.com

This dissertation was typed by the author.